KU LEUVEN

ARENBERG DOCTORAL SCHOOL
Faculty of Science

Characterization of semiconductor interfaces by nonlinear optical techniques

Vanbel Maarten

Dissertation presented in partial fulfillment of the requirements for the degree of Doctor in Science

May 2014

Characterization of semiconductor interfaces by nonlinear optical techniques

Vanbel Maarten

Supervisory Committee:
Prof. dr. M. Van der Auweraer, chair
Prof. dr. T. Verbiest, supervisor
Prof. dr. V.K. Valev, co-supervisor
Prof. dr. J.-P. Locquet, co-supervisor
Prof. dr. M. Caymax, co-supervisor
Prof. dr. K. Clays
Prof. dr. M. Nguyen
Prof. dr. S. De Gendt
Prof. dr. A.V. Silhanek
(Université de Liège)

Dissertation presented in partial fulfillment of the requirements for the degree of Doctor in Science

May 2014

Acknowledgments
The research presented in this PhD thesis has been funded by the KU Leuven (GOA), with the financial support of Dr. Sven Van Elshocht of imec.

Cover image
Adaptation of an image of Edelweiss, purchased from fotolia with royalty-free license. The cover represents an SHG measurement on a fully processed microprocessor. This knowledge obtained from the research presented in this thesis is intended as footsteps towards this ultimate goal of characterization of transistor-based devices with nonlinear optical techniques.

Uitgegeven in eigen beheer, Vanbel Maarten, Celestijnenlaan 200D box 2425, B-3001 Heverlee (Belgium)

ISBN 978-90-8649-710-2
D/2014/10.705/19

Merci!

"... dann bin ich auch, wie sie wissen, gleich stuff,
wenn ich immer für ein Instrument,
das ich nicht leiden kann, schreiben soll...

"You know that I become quite powerless
whenever I am obliged to write for an instrument
which I cannot bear."

Wolfgang Amadeus Mozart

Wie had ooit gedacht dat iemand van wie men zei dat hij een goede lasser moest worden, een doctoraat in de chemie zou kunnen behalen? Wie durft het advies van de "experten" van het PMS[1] naast je neerleggen en studeren waar je zin in hebt? Wie kiest er bij het afstuderen van de humaniora een studierichting door in verschillende vakjes van een darts-bord opleidingen te schrijven om vervolgens met een pijltje naar dat bord te gooien en dan de opleiding te volgen waar het pijltje valt? Onder het motto: als ik geen opleiding dwarsfluit mag volgen, dan maakt het mij niet zoveel uit wat ik wel ga studeren. Meer nog, laat ik beide opleidingen starten, dan kan ik die moeilijke keuze wat uitstellen. Maar dat keuze moment moest toch komen: na 3 jaar conservatorium muziek laten varen voor chemie ging met heel veel pijn in het hart. Maar wat als ik chemie had laten vallen voor dwarsfluit? Ik ben nog steeds verbaasd over mezelf dat ik tot deze beslissing gekomen ben... Spijt heb ik van die beslissingen niet, maar de vraag blijft: wat als? Die vraag is onmogelijk om te beantwoorden. Je weet niet, 'wat als', maar vaak wel 'wat als ik niet'. Ik mag niet klagen, want ik geniet van mijn leven en van de vele ervaringen die ik beleef.

[1] Het gaat hier over de vroegere versie van het centrum van leerlingenbegeleiding CLB en niet over enkele vrouw-specifieke klachten

Het is met deze ervaringen in het achterhoofd dat de quote van W. A. Mozart meer betekenis krijgt. Mozart schreef briljante fluitmuziek. Letterlijk briljant, want in tijden van crisis schreef Mozart vrolijke en luchtige muziek, ongeacht persoonlijke en financiële problemen. Daarenboven vond hij dwarsfluit maar een onnozel instrument. En toch vond hij de kracht om voor dit instrument prachtwerken neer te pennen. Ik kan niet zeggen dat deze quote me geïnspireerd heeft om ook zo te handelen, maar de gelijkenissen zijn wel frappant. Ik heb een opleiding tot een goed einde kunnen brengen, hoewel een andere opleiding me misschien ('wat als?') beter lag en heb me daar 100% voor ingezet. Laat de originele quote dan nog over dwarsfluit gaan, dat maakt het des te persoonlijker.

Met het schrijven van mijn doctoraatsthesis, komt er een einde aan een mooie periode in mijn leven: mijn studententijd. Ik kan stellen dat ik er heel hard van genoten heb, met alle muzikale, sportieve en studentikoze activiteiten incluis. Het staat vast dat ik nog vaak met heimwee zal terugdenken aan deze tijd. Ik moet bekennen dat tijdens mijn doctoraat ik soms nog iets teveel als student door het leven ging, maar je kan er maar wel bij varen, dacht ik. Ach, dat is gewoon een teken dat het echt goed is geweest!

Naast het mijmeren over vervlogen studententijd, is het einde van een belangrijke periode ook een moment om merci te zeggen. Hoewel het grootste gedeelte van een doctoraatswerk en de voorafgaande studie en opleidingen een individuele taak is geweest, gebaseerd op zelfstandigheid, is het onmogelijk om alleen door deze jaren te ploeteren. Zelfs zonder existentiële perikelen, is de hulp van velen onontbeerlijk!

Als eerste richt ik graag enkele woorden aan Thierry. Het moet moeilijk zijn om promotor te zijn van iemand die initieel niet zomaar aanneemt van wat je zegt en er vaak zijn eigen mening op nahoudt. Ik moet toegeven dat ik mijn mening wel eens moest herzien en terug bij jou kwam om je gelijk te geven. Je gunde me een grote vrijheid in mijn onderzoek, waardoor ik met vele verschillende aspecten van wetenschappelijk onderzoek in contact kwam. Hierdoor mocht ik vaak naar congressen, waardoor ik steeds met een nieuwe kijk op ons eigen onderzoek terugkwam. Bedankt voor je zeeën van geduld en steun!

Vervolgens wil ik graag mijn co-promotoren in de bloemetjes zetten. Ventsi, je maakte me wegwijs in de wereld van niet-lineaire optica en bij uitbreiding de wetenschappelijke gemeenschap. Je enthousiasme voor wetenschap werkte aanstekelijk. Dankzij mijn andere co-promotoren Jean-Pierre en Matty kreeg ik de kans om samenwerkingen aan te gaan, waardoor ik een waardevolle bredere kijk heb gekregen op 'interdisciplinair werken': Bedankt.

Zonder onderzoeksproject, geen onderzoek; zonder centen, geen onderzoeker. Daarom wil ik in het bijzonder Sven Van Elshocht van harte bedanken die mijn geldschieter was tijdens mijn eerste jaar als doctorandus. Gelukkig werd deze

taak van geldschieter in de laatste 3 jaar van mijn onderzoek overgenomen door Thierry.

Furthermore, I would like to thank all my jury members for their evaluation of my research and their constructive feedback and comments on my PhD thesis. I hope you enjoyed reading my thesis.

In een volgende paragraaf wil ik merci zeggen aan de personen die meegewerkt hebben aan dit onderzoek. Ik kan me niet herinneren hoe vaak ik met Rik Paesen van UHasselt achter zijn SHG-microscoop heb gezeten om het een of ander staal te bekijken, waarna we vaak in een discussie verzeild geraakte, in een poging om te begrijpen wat we op het beeld zagen. Het was zeer aangenaam om met je samen te werken. Hopelijk komen we mekaar nog tegen, maar dan liefst niet in een donkere kelder, zoals nu.
Ik ben en blijf een chemist die met het taalgebruik van een chemist over fysische problemen of vraagstukken nedankt. Daardoor is het van cruciaal belang om hulp te krijgen vanuit fysisch georiënteerde personen. Speciale dank gaat uit naar Prof. Valeri Afanas'ev van het departement fysica aan de KU Leuven. Uw fysisch inzicht is onnavolgbaar. Ik kan zeggen dat ik door uw bijdrage sneller tot inzichten kon komen. Ik leerde dat de taal die een chemist gebruikt duidelijk verschillend is dan de taal van een fysicus. Mede hierdoor werd onze samenwerking waardevol.
Door medewerking van Christoph, Annelies en Sonja van imec was er nooit een tekort aan structuren en projecten om aan te werken. Omdat verschillende metingen op oxidatie-gevoelige structuren in het weekend moesten ingepland worden, verdienen deze metingen een speciale plaats in mijn geheugen.

Als we het nu toch over speciale plaatsen hebben, dan is het nu op z'n plaats om de mannen van de bureau te bedanken. Ik denk dat we de meest sfeervolle bureau in den D hebben. Vaak stond er een niet-al-te-hoogstaand liedje op, waarvan we allemaal de tekst kennen en als het dat niet was, dan waren we wel aan het afgeven op elkaar muzikale smaak. Toch vond ik het een heel aangename sfeer om in onze bureau aan wetenschap te doen. Ik wil Stefaan bedanken voor onze ontspanningsmomenten in de vorm van een potje schaak en later de laservariant laser game. Hierdoor keerde de frisheid in m'n hoofd terug, om daarna verder te werken. Ward, m'n congresmaat bij uitstek. Door het goed inplannen en uitbreiden van onze congres-plannen hebben we samen al enkele interessante plaatsen in de wereld bezocht. Roadtrippen is echt de max met je. Bovendien is onze traditie van eens om de zoveel tijd speciale bieren te gaan drinken er eentje om te bewaren. Eerst al zittend, dan al staand, maar de zware bieren zullen het geweten hebben! Bloemen, mijn naamgenoot en inwoner van (ondertussen) dezelfde stad. Het was zeer aangenaam om met je samen te studeren en nu samen te doctoreren. Sinds het begin van onze studie reageren we steeds minder en minder op Maarten en onze achternaam werd

onze roepnaam, maar dat is een prijs die ik daarvoor graag betaal. Ontspannen deden we door samen een gameke te spelen en dat leverde ons vele leuke avonden op. Hopelijk blijven we jong genoeg van geest om dat nog vaak te doen! Misschien nog eens een Testosterona-activiteit fixen? Ook de andere leden van onze onderzoeksgroep zou ik graag willen bedanken voor de sfeer in het labo en tijdens de taart-momenten. Ik zou Pieter-Jan en Griet willen bedanken, voor de babbels bij een tas thee of koffie en Rik en Frans in vroegere tijden, voor hun hulp bij electronica-problemen en mijn toeverlaat in het vinden van de juiste schroevendraaiers. In dit opzicht draag ik ook de mannen van de mechanische werkenplaats, Tony, Kevin en Peter een warm hart toe. Zij knutselden vele oplossingen voor optische opstellingen voor me in elkaar. Ze zijn van goudwaarde!

Buiten de werkomgeving zijn er ook enkele mensen die zeer belangrijk voor me zijn en die ervoor gezorgd hebben dat ik ben wie ik nu ben en sta waar ik nu sta. Als eerste zou ik graag Meester Van den Hende bedanken. Niet enkel mijn muzikale, maar ook sociale talenten heb ik bij jou in de dwarsfluitles kunnen ontwikkelen. Ik moet toegeven dat ik op elk fluitexamen nog steeds een stuk uitkies dat ik voor jou speel. Lindy heeft je werk goed overgenomen en door jullie blijft mijn droom van fluitist toch wat langer hangen: bedankt! De persoon die ervoor gezorgd heeft dat ik vrede kon nemen met mijn 'gekozen' studierichting is Rosa, beter bekend als Madam Vynckier. Het is duidelijk dat ook zij een speciale dank u wel verdient. Zij begreep al snel dat je als bij mij iets duidelijk wou maken, men dat best deed wanneer mijn maag gevuld was. Bedankt voor je lekkere pannenkoeken wanneer we met de mannen van Geel op bezoek kwamen, voor je steun en luisterend oor. PS: nogmaals sorry voor de misgelopen proef met HCl in het laatste jaar van de humaniora!

Van de mannen van Geel zijn er uiteindelijk 3 die hun chemie studies afgemaakt hebben. Bogaert en Bloemen, jullie zijn meer dan studie-maten. Tijdens onze studie werd het groepje van 3 aangevuld door den Bram, die nu, ondanks zijn Leuvense roots, toch al aardig een mondje Kempisch dialect kan meepraten. Zonder onze ontspannende game-avonden en kaartmiddagen zou mijn studententijd niet hetzelfde geweest zijn! Bovendien zou deze thesis nooit zijn afgeraakt. Hele dikke merci mannen! En dat er nog vaak ge-whololoo-t mag worden!

Vriendschappen van in Geel en ver daarbuiten: Leerlingenraders, vrienden uit de muziekschool en fanfare, kotgenootjes en groenvelders, Chemika, Top Vakantie maatjes en makkers van de scouts uit lang vervlogen tijden, teveel mensen op persoonlijk op te noemen. Jullie bijdrage aan mijn doctoraat was misschien eerder gering, maar men moet ook ontspannen he! Daar hebben jullie ruimschoots voorgezorgd: Merci! Eén daarvan moet ik echt wel persoonlijk bedanken: Kotgenoot, zot om mee te gaan mountainbiken, te gamen, pinten

te pakken, te karren met onze Ford Focussen, kortom: ne maat voor het leven. Pieter, uw bijdrage aan mijn doctoraat valt niet te onderschatten! Het is fijn om te weten dat na het laat werken iemand op kot zit die altijd wel zin en tijd heeft om een gameke te knallen zodat ik nadien weer volledig ontspannen was. De weinige frustraties moest je erbij pakken, maar dan speelden we geen AOE en dan kon je dat wel verdragen zeker. Onder het motto: Everyone is getting married or pregnant, we are just getting more awesome! Check!

Na zo'n uitspraak is de moment aangebroken om mijn vriendin Sanne te bedanken. Het moet niet makkelijk zijn om met een wetenschapper als lief door het leven te gaan, maar ze zijn op z'n minst rationeel, of dat zou toch moeten. Of dat altijd positief is, dat zal ik in het midden laten! Geek of niet, dat speciaal T-shirt dat ik van je kreeg is echt mooi. Alle gekheid op een stokje, bedankt om er altijd voor me te zijn, lieve schat! Zonder jou was ik toch niet de ik die ik nu ben en dat vind ik best ok!

Tenslotte en in het bijzonder wil ik mijn zus en ouders bedanken. Mijn grote zus Ann is er altijd al voor mij geweest. Bedankt voor je steun zus, altijd en overal. Je zorg voor mij, de kleine broer, heb ik nog bij niemand anders zo ervaren. Gelukkig kan ik jou ondertussen ook al wat helpen en is de vroegere eenrichtings-hulp voorbij! Bedankt zusje!
Moeder en vader, ik ben jullie niet vergeten. Maar de belangrijkste dingen zeg ik meestal maar één keer en na de details eindig ik met het essentie! Tijdens mijn hele leven heb ik grotendeels mogen doen waar ik zin in had. Steeds stonden jullie klaar met raad en daad. Vaak volgde ik die raad dan ook op en als ik dat dan al eens niet deed, dan hebben we daar mettertijd uit geleerd. Maar die koppigheid: het zal altijd een stukje van mij zijn. Niet enkel als sponsors, maar ook als supporters waren jullie steeds van de partij bij de alledaagse en belangrijke momenten. Jullie hebben meermaals een bidon aangegeven, zowel op als naast de fiets. De grootste merci van allemaal is daarom ook bestemd voor jullie, alsook een dikke knuffel en een flinke hand. Jullie maken veel van me en ik weet dat jullie heel trots op me zijn voor wat ik tot nu toe heb bereikt. Daar ben ik dan weer trots op.

Bij deze wil ik deze thesis dan ook opdragen aan alle mensen, hetzijn anoniem of met naam vernoemd.

Ut vivat, crescat, floreatque amicitia

Maarten

Abstract

Nonlinear optics is a wide research field based on the nonlinear relationship of the electric field component of light and the induced polarization in matter under intense laser illumination. The second order effect second-harmonic generation (SHG) is often used as a surface characterization tool for materials with a center of symmetry. Due to the advantage of probing surfaces and even buried interfaces, specific material properties can be attributed to the material surface instead of the bulk. Moreover, SHG is very sensitive to changes in the surface structure or alignment of molecules thereon. An additional advantage is the non-invasiveness of SHG, which makes the technique applicable to fragile materials. Exploiting these advantages, SHG can be a useful technique in semiconductor industry, since semiconductor devices consist of a sequence of thin layers. Metal-oxide-semiconductor field-effect transistors (MOSFETs) consist of an oxide layer on top of a semiconductor with different contact areas and are the fundamental parts of e.g. computer chips. The interface between these layers determines the power consumption, reliability, operating voltage, leakage current of the resulting device, etc. Optimizing the interfaces between these layers, will result in an optimized transistor performance. SHG can provide valuable insight in interface-specific processes in semiconductor research.

In this work, we investigate the surface and interfaces in MOSFETs. We determine the optimal growth conditions with respect to the carrier gas and temperature during atomic layer deposition (ALD) of the oxide layer. During the ALD process, the composition of the bonds at the surface changes, which results in a change in the isotropic contribution of SHG. For thicker oxide layers, it is shown that the SHG response is thickness independent.
Moreover, passivation of the interface is important for optimal device properties. Therefore, the influence of the oxidizing agent and number of oxidation steps on a Si capped Ge layer is probed.
Since the operation of MOSFET is voltage dependent, electric field-induced second-harmonic generation (EFISH) is performed on Al_2O_3 and MgO covered

Si substrates. The charges contribute to the EFISH signal, hence a change in charge distribution will result in a changing EFISH intensity. We observe the tunneling of holes from the semiconductor layer to the Al_2O_3 and migration of oxygen vacancies in MgO.
Graphene is an upcoming semiconducting material, which is to be incorporated in a new type of transistor. The capability of using SHG as symmetry-sensitive probe and visualization method is tested on graphene and a novel analyzing method based on fast Fourier-transformation is proposed.
These findings illustrate the usefulness of SHG and EFISH to probe buried interfaces in semiconducting material and charge separation therein. In this manner, these second-order nonlinear techniques can push the boundaries in semiconductor manufacturing.

Beknopte samenvatting

Niet-lineaire optica is een breed onderzoeksveld gebaseerd op de niet-lineaire correlatie van de electrische veld component van licht en de geïnduceerde polarizatie van materie, wanneer het materiaal beschenen wordt met hoog energetisch laser licht. Het tweede-orde effect second-harmonic generation (SHG) of frequentieverdubbeling wordt vaak gebruikt als karakterisatie methode voor oppervlakken van materialen met een inversiecentrum. Het voordeel van het karakteriseren van oppervlakken en zelfs bedekte interfasen maakt het mogelijk om bepaalde specifieke eigenschappen van een materiaal toe te kennen aan het oppervlak in plaats van aan de bulk. Bovendien is SHG zeer gevoelig aan veranderingen aan de structuur van het oppervlak of van uitlijning van moleculen aan het oppervlak. Een bijkomend voordeel is dat SHG niet-invasief is, waardoor fragiele structuren kunnen bestudeerd worden met deze techniek. Dankzij deze voordelen kan SHG een interessante en bruikbare techniek zijn in halfgeleider industrie, aangezien transistoren opgebouwd zijn uit verschillende lagen. Metal-oxide-semiconductor field-effect transistors (MOSFETs) bestaan uit een oxide laag die bovenop een halfgeleidend materiaal is afgezet waarin verschillend gedopeerde contact gebieden in zijn aangebracht. Een MOSFET vormt een van de basisonderdelen van o.a. computer chips. Het grensvlak tussen deze lagen bepaalt het verbruik, betrouwbaarheid, spanningsval, stroomverbruik door een lekstroom, enz. Optimalizering van dit grensvlak zal leiden tot verbeterde prestaties van de transistor. Hierbij kan SHG bijkomend inzicht bieden in de interfase-specifieke processen in halfgeleider onderzoek.

In dit werk onderzoeken we oppervlakken en grensvlakken van metal-oxide-semiconductor field-effect transistors (MOSFETs). We bepaalden de optimale afzettingscondities in het atomic layer deposition (ALD) proces, door het beste draaggas en verwerkingstemperatuur te bepalen. Tijdens de eerste cycli van het ALD process kan de bindingstoestand van de atomen aan het oppervlak variëren, waardoor er een verandering in isotrope bijdrage in het SHG signaal bemerkt wordt. Deze bijdrage verandert niet meer bij dikkere oxide lagen. Bovendien kan

de invloed van de oxidantia en het aantal oxidatie stappen bestudeerd worden van een dunne laag Si op een Ge substraat. Aangezien de werking van een MOSFET spanningsafhankelijk is, voerden we electrisch veld geïnduceerd SHG (EFISH) metingen uit op Al_2O_3 en MgO gepassiveerde Si substraten. Door het aanleggen van een extern electrisch veld werd tunneling van gaten vanuit Si tot in het Al_2O_3 geobserveerd en migratie van zuurstof deficiënte sites in de MgO laag. Grafeen is recent een interessant semi-metaal dat kan ingebouwd worden in een nieuw type van transistor. We testten dat SHG kan gebruikt worden als symmetriegevoelige meettechniek en visualisatiemethode voor grafeen en beschrijven een nieuwe analyzemethode voor SHG gebaseerd op snelle Fourier-transformaties. Onze bevindingen bevestigen dat SHG en EFISH uiterst nuttig is voor het bestuderen van bedekte interfasen in halfgeleidende materialen en hun ladingsverdeling. Op deze manier kan tweede-orde niet-lineaire optica de productie limiet verleggen in halfgeleider productie.

Abbreviations

2PF	Two-photon fluorescence
AFM	Atomic force microscopy
ALD	Atomic layer deposition
CV	Capacitance-voltage
EFISH	Electric field-induced second-harmonic generation
FFT	Fast Fourier transform
FFT-SHG	Fast Fourier-transform second-harmonic generation
FLIM	Fluorescence-lifetime imaging microscopy
IRS	International technology roadmap for semiconductors
IC	Integrated circuit
ML	Monolayer
MOF	Metal-organic-framework
MBE	Molecular beam epitaxy
MOS	Metal-oxide-semiconductor
MOSFET	Metal-oxide-semiconductor field-effect transistor
NLO	Nonlinear optical
SCR	Space-charge region
SE	Spectroscopic ellipsometry
SH	Second-harmonic
SHG	Second-harmonic generation
SOI	Silicon-on-insulator
SNR	Signal to noise
TD-SHG	Time-dependent second-harmonic generation

list of symbols

$\nabla\cdot$	Divergence operator
$\nabla\times$	Curl operator
β	Field dependency
ϵ	Dielectric constant
θ	Phase
λ	Wavelength
μ_n	Charge mobility
ρ	Charge density
σ	Capture cross section
τ	Temporal periodicity
ϕ	Azimuthal rotation angle
Φ	Band bending
χ	Electron affinity
$\chi^{(1)}$	First-order susceptibility
$\chi^{(2)}$	Second-order susceptibility
$\chi^{(3)}$	Third-order susceptibility
χ^{D}	Dipole nonlinear susceptibility
χ_{eff}	Effective nonlinear susceptibility
χ^{Q}	Quadrupole nonlinear susceptibility
ω	Angular temporal frequency

$\mathbf{B}$	Total magnetic field strength
c	Speed of light
C	Capacitance
$\mathbf{D}$	Displacement field
D_{it}	Interface trap density
$\mathbf{E}$	Electric field
$\overrightarrow{E}_{dc}$	Internal dc electric field
E_g	Band gap
$\mathbf{H}$	Applied magnetic field
i	Imaginairy number
I_e	Current of charges in the SCR of the semiconductor
$\mathbf{J}$	Current density
k	Propagation number
$\mathbf{k}$	Propagation direction in the beam coordinate system
k_B	Boltzmann constant
n	Refractive index
N	Number of charges
$\mathbf{P}$	Polarization
P^D_{iso}	Isotropic dipole polarization
P^Q_{anis}	Anisotropic quadrupole polarization
P^Q_{iso}	Isotropic quadrupole polarization
$\mathbf{P}^{\text{NL}}$	Nonlinear polarization
q	Charge per electron
Q_f	Amount of fixed charges
Q_{it}	Amount of trapped charges
Q_m	Amount of mobile ionic charges
t	Time
v	Charge velocity
V_{FB}	Flatband voltage
V_g	Gate-drain voltage
V_{ox}	Voltage over the oxide layer
W_m	Work function of the gate metal
W_s	Work function of the semiconductor

Contents

Chapter 1

Introduction

Shortly after the invention of the laser by Maiman in 1960,[1] the field of nonlinear optics was started by the discovery of second-harmonic generation by Franken *et al.* in 1961.[2] Nonlinear optics was already known much earlier by the discoveries of Kerr and Pockels, who used external electrical fields to modify the refractive index of a material. However, Franken was the first to show a nonlinear optical effect using the applied optical electric field instead of an external electric field. The nonlinear optical effect of second-harmonic generation, where the polarization depends quadratically on the applied optical field, doubles the frequency and hence changes the color of the light beam. Bloembergen *et al.*[3] provided the first theoretical framework on harmonic generation and optical wave mixing in 1962. Since then, the field has grown at such a fast rate that today, nonlinear optics has a contribution in a lot of scientific research fields ever since.[4]

While research in nonlinear optics was ongoing, advances in semiconductor research were boosted by the manufacturing and improvement of the first Si based transistor, invented by Morris Tanenbaum at Bell labs in 1954 and manufactured by Texas instruments in the same year.[5] The world had to wait until 1960 for the first metal-oxide-semiconductor (MOS) transistor and even to 1971 for the first integrated circuit (IC).[6] These ICs are the basic semiconductor devices for computers: from 4004 transistors on the first IC, to 1.16 billion transistors on the intel i7 microprocessor. Today, semiconductor research is a billion dollar, multi-cooperation franchise employing millions of people and providing new material for the digital age in which we live.

In this thesis, we use the advantages of nonlinear optics to characterize semiconductor devices. The coincidence of their almost simultaneous discovery

is not the major reason for combining the field of nonlinear optics with semiconductor research. Due to specific characteristics of second-harmonic generation, interface-properties of semiconductor devices can be explored and characterized. In the following sections, a short introduction to both subjects is presented here, as well as the research goal of this thesis.

1.1 Towards nonlinear optics

Optics in general is the study of light-matter interactions. Light consists of an electric and magnetic field component, which are perpendicularly oriented with respect to each other and the propagation direction of light. Moreover, the electric and magnetic field component are in phase with each other. Overall, the most dominant interaction of matter with light is through its electric field. We focus on this interaction and describe the electric field component of light as a propagating wave.

1.1.1 Light in vacuum

Light can be described in vacuum by a general differential wave function, which relates the space, x and time, t dependencies of the function $\phi(x,t)$. The one-dimensional differential wave equation can be written as

$$\frac{\delta^2\phi}{\delta x^2} = \frac{1}{c^2}\cdot\frac{\delta^2\phi}{\delta t^2} \tag{1.1}$$

which is a homogeneous differential equation for undamped systems. No driving force or attenuation of the propagating wave is considered, which is allowed if one considers the propagation of light in vacuum. In vacuum, the speed of light is a constant, equal to $c = 299\ 792\ 458$m/s.

Solving the wave equation (eq. (1.1)) in vacuum conditions, yields

$$\phi = A\ sin\ (kx \pm \omega t) \tag{1.2}$$

where A is the amplitude of the wave, k the propagation number and ω the angular temporal frequency with the unit rad/s. The propagation number k can be converted to the spatial periodicity or wavelength of light by $k = 2\pi/\lambda$. For visible wavelengths, λ covers the wavelength range from 380nm to 800nm. Also the angular temporal frequency can be written as, $\omega = 2\pi\nu$, where ν is the frequency.

Since the dominant interaction of light with matter is through its electric field component, eq. (1.2) can be interpreted as a propagating electric field, where $\phi = E(r,t)$ and $A = E_0$.

This way of representing a light wave is very intuitive. Nevertheless, it is sometimes hard to calculate wave propagation with this type of wave representation. Often trigonometric manipulations are needed, which are time consuming to validate. Therefore, we will write the solution of the wave equation as a complex wave representation. In the complex presentation, polar coordinates r, the magnitude and θ, the phase angle in rad are used to describe the coordinate system. These coordinates are connected to Cartesian coordinate system as

$$x = r\,cos\,\theta \qquad\qquad y = r\,sin\,\theta \tag{1.3}$$

Using Eulers formula,

$$e^{i\theta} = cos\,\theta + isin\,\theta \tag{1.4}$$

the solution of the wave equation (eq. (1.2)) can be written in a complex wave function.

In order to obtain a general formulation of an electro-magnetic wave which can account for nonlinear optical phenomena, a complex conjugate is added to obtain one harmonic wave, of which the resulting wave has a real character instead of an imaginary. For a monochromatic wave, the electric field $E(r,t)$ can be written as

$$E(r,t) = E_0(e^{ik.r-i\omega t} + e^{-ik.r+i\omega t}) \tag{1.5}$$

where E_0 is the amplitude of the electro-magnetic wave and the latter term is denoted as the complex conjugate. It can be noticed again, that this wave is both time and space-dependent at a specific angular frequency ω. Up until now, the electric field was described as a scalar quantity. However, the electric field is in general described as a vector, since E_0 has a magnitude, direction and sense. Moreover, both r and k are also vectors, which yields $\vec{r} = \mathbf{r}$ and $\vec{k} = \mathbf{k}$

Introducing this vector behavior in eq. (1.5) results in

$$\mathbf{E}(r,t) = \mathbf{E_0}(e^{i\mathbf{k}.\mathbf{r}-i\omega t} + e^{-i\mathbf{k}.\mathbf{r}+i\omega t}) \tag{1.6}$$

where $\mathbf{k}$, $\mathbf{r}$ and $\mathbf{E_0}$ are correlated since their vector behavior determines the propagation direction of the electro-magnetic wave. Now, one of the solutions

to the wave equation is fully described. However, all the parameters in the equations above are defined in vacuum conditions only.

1.1.2 Linear optics in a medium

The undamped solution to the wave equation in vacuum is not sufficient to describe the propagation of light in a medium. To describe optical phenomena in a material, Maxwell's equations are required. Note that these equations can also be used to calculate the wave propagation in vacuum. For simplicity, Maxwell's equations are written in Gaussian units.

$$\nabla \cdot \mathbf{D}(\omega) = 4\pi\rho \tag{1.7}$$

$$\nabla \cdot \mathbf{B}(\omega) = 0 \tag{1.8}$$

$$\nabla \times \mathbf{E}(\omega) = -\frac{1}{c}\frac{\delta \mathbf{B}(\omega)}{\delta t} \tag{1.9}$$

$$\nabla \times \mathbf{H}(\omega) = \frac{1}{c}\frac{\delta \mathbf{D}(\omega)}{\delta t} + \frac{4\pi}{c}\mathbf{J}(\omega) \tag{1.10}$$

where $\mathbf{D}(\omega)$ denotes the displacement field, ρ the charge density, $\mathbf{B}(\omega)$ the magnetic field, $\mathbf{E}(\omega)$ the electric field, $\mathbf{H}(\omega)$ the applied magnetic field, $\mathbf{J}(\omega)$ the current density and the nabla ∇ denotes a three-dimensional gradient operator; which leads to $\nabla\cdot$ the divergence operator and $\nabla\times$ the curl operator, respectively.

Provided that there are no free charges and no free currents, Maxwell's equations can be simplified since, $\rho = 0 \quad$ and $\quad \mathbf{J}(\omega) = 0$ respectively. Moreover, when considering the case for nonmagnetic material, $\mathbf{B}(\omega) = \mathbf{H}(\omega)$, the displacement field is dependent on the electric field and the induced polarization

$$\mathbf{D}(\omega) = \mathbf{E}(\omega) + 4\pi\mathbf{P}(\omega) \tag{1.11}$$

This induced polarization $\mathbf{P}(\omega)$ is the dipole moment per unit of volume, and describes the interaction of light with a material. Hence, the polarization is the sum over all dipole moments. In Gaussian units,

$$\mathbf{P}(\omega) = \sum_i \mu_i(\omega) = \chi^{(1)}(\omega)\mathbf{E}(\omega) \tag{1.12}$$

where $\mu_i(\omega)$ is the induced dipole moment and $\chi^{(1)}(\omega)$ the first-order susceptibility. This susceptibility parameter contains all information of linear

optical phenomena. When considering a macroscopic medium, such as reflection, refraction, absorption, etc. the term "linear" refers to the direct proportionality of the strength of the electric field $E(t)(\omega)$ to the induced polarization in a medium $P(t)(\omega)$ in eq. (1.12). For nonlinear optics, this relationship is no longer linear. $\chi^{(1)}(\omega)$ is a complex number and is related to the refractive index n_ω and the dielectric constant ϵ_ω by

$$n_\omega^2 = \epsilon_\omega = 1 + 4\pi\chi^{(1)}(\omega) \tag{1.13}$$

Now, using this correlation in eq. (1.11), the electric displacement field becomes

$$\mathbf{D}(\omega) = n_\omega^2 \mathbf{E}(\omega) \tag{1.14}$$

Hence, the refractive index of a medium determines its optical properties. As opposed to the wave equation in vacuum, the index of refraction of the medium has to be inserted in the wave equation by the electric displacement field. Deriving the optical wave equation starts from taking the curl operator of eq. (1.9) and using $\mathbf{B}(\omega) = \mathbf{H}(\omega)$ to rewrite the right-hand side of eq. (1.9) with eq. (1.10) to obtain the equation

$$\nabla \times \nabla \times \mathbf{E}(\omega) + \frac{1}{c^2}\frac{\delta^2}{\delta t^2}\mathbf{D}(\omega) = 0 \tag{1.15}$$

Eliminating the displacement field by eq. (1.11), results in

$$\nabla \times \nabla \times \mathbf{E}(\omega) + \frac{1}{c^2}\frac{\delta^2}{\delta t^2}\mathbf{E}(\omega) = \frac{-4\pi}{c^2}\frac{\delta^2 \mathbf{P}(\omega)}{\delta t^2} \tag{1.16}$$

This is a general case of the wave equation in optics, both for linear and nonlinear optics, where the relationship between the electric field E and the polarization P is clear. Since the polarization and the electric field are vectors, the susceptibility is a tensor, which for $\chi^{(1)}$ is a second-rank tensor. Equation (1.12) is valid when the strength of the applied optical field is small, i.e. when P is related linearly to E.

1.1.3 Nonlinear optics in a medium

When using high electric field strength, e.g laser irradiation, eq. (1.12) needs to be generalized for higher-order contributions by means of a Taylor expansion, which yields

$$\mathbf{P} = \mathbf{P}^{(1)} + \mathbf{P}^{(2)} + \mathbf{P}^{(3)} + \cdots$$

$$= \chi^{(1)}\mathbf{E}(\omega) + \chi^{(2)} : \mathbf{E}(\omega)\mathbf{E}(\omega) + \chi^{(3)} \vdots \mathbf{E}(\omega)\mathbf{E}(\omega)\mathbf{E}(\omega) + \cdots \tag{1.17}$$

where $\chi^{(2)}$ and $\chi^{(3)}$ are the second and third-order nonlinear optical susceptibility, respectively and $\chi^{(2)}$ is a third-rank tensor and $\chi^{(3)}$ a fourth-rank tensor. Note that the for factors are neglected. Hence, the linear relation between $\mathbf{P}(\omega)$ and $\mathbf{E}(\omega)$ no longer holds for high electric field strengths.

In nonlinear optics, it is convenient to rewrite the wave equation 1.16 in such a way that the nonlinear source term is explicitly described. The total polarization can be written as summation of the linear and nonlinear polarization ($\mathbf{P} = \mathbf{P}^{(1)}(\omega) + \mathbf{P}^{\mathrm{NL}}$). Substituting $\mathbf{P}(\omega)$ from eq. (1.16) by this equation, where the frequency symbol is omitted, since we allow for nonlinear processes which result in different frequency components, yields

$$\nabla \times \nabla \times \mathbf{E}(\omega) + \frac{1}{c^2}\frac{\delta^2}{\delta t^2}\mathbf{D}(\omega) = \frac{-4\pi}{c^2}\frac{\delta^2 \mathbf{P}^{\mathrm{NL}}}{\delta t^2} \tag{1.18}$$

where $\mathbf{D}(\omega)$ is the linear displacement field.

Since eq. (1.14) is still valid for the linear displacement field, eq. (1.18) yields

$$\nabla \times \nabla \times \mathbf{E}(\omega) + \frac{n^2}{c^2}\frac{\delta^2}{\delta t^2}\mathbf{E}(\omega) = \frac{-4\pi}{c^2}\frac{\delta^2 \mathbf{P}^{\mathrm{NL}}}{\delta t^2} \tag{1.19}$$

This equation has the form of a driven (i.e. inhomogeneous) wave equation. The nonlinear response of the medium acts as a source term which appears on the right-hand side of this equation. In the absence of this source term, eq. (1.19) simplifies to a homogeneous wave equation, which describes the light propagation in vacuum.[7]

1.1.4 Second-harmonic generation within the electric dipole approximation

Knowing now that nonlinear optical phenomena can take place in a medium, we want to describe which information this can give us about the material. The charges within a material are displaced under the influence of an electromagnetic field. The displacement of these charges can be represented as a series of electric moments (dipole, quadrupole, etc.) For electrons in a bond, the largest contribution to the electric moment is the electric dipole contribution.

In this case, the electron will be displaced along the direction of the bond itself. As a first simplification in describing the nonlinear response of a material, this approximation will be used. This approximation is referred to the electric dipole approximation. The other higher-order terms are neglected at this stage.

Focusing on the second-order term of eq. (1.17), the polarization is quadratic in the electric field.

$$P_i^{(2)} = \sum_{j,k} \chi_{ijk}^{(2)} \cdot E_j E_k \tag{1.20}$$

Since both the polarization and the electric field are vectors, the sum of the different tensor components is explicitly written. Often eq. (1.20) is simplified using the summation convention, which implies that when an index variable appears twice in a single term it implies summation of that term over all the values of the index.

$$P_i^{(2)} = \chi_{ijk}^{(2)} \cdot E_j E_k \tag{1.21}$$

Furthermore, simplifications can be made by using permutation of indices, when considering second-harmonic generation. For this nonlinear optical phenomenon, both electric field strengths originate from the same fundamental beam, which means that $j = k$ in eq. (1.20), while for sum frequency generation, $j \neq k$. Since one cannot distinguish between the two identical incident electric fields in a SHG experiment, the last 2 indices of the susceptibility tensor can be exchanged or permutated.

$$P_i^{(2)} = \chi_{ijk}^{(2)} \cdot E_j E_k = \chi_{ikj}^{(2)} \cdot E_k E_j \tag{1.22}$$

As a consequence,

$$\chi_{ijk}^{(2)} = \chi_{ikj}^{(2)} \tag{1.23}$$

where the index i represents the direction of the induced polarization and j and k are direction of the incident electric fields.

Therefore, evaluating eq. (1.21) yields

$$\begin{bmatrix} P_x^{(2)} \\ P_y^{(2)} \\ P_z^{(2)} \end{bmatrix} = \begin{bmatrix} \chi_{xxx}^{(2)} & \chi_{xyy}^{(2)} & \chi_{xzz}^{(2)} & \chi_{xyz}^{(2)} & \chi_{xxz}^{(2)} & \chi_{xyx}^{(2)} \\ \chi_{yxx}^{(2)} & \chi_{yyy}^{(2)} & \chi_{yzz}^{(2)} & \chi_{yyz}^{(2)} & \chi_{yxz}^{(2)} & \chi_{yyx}^{(2)} \\ \chi_{zxx}^{(2)} & \chi_{zyy}^{(2)} & \chi_{zzz}^{(2)} & \chi_{zyz}^{(2)} & \chi_{zxz}^{(2)} & \chi_{zyx}^{(2)} \end{bmatrix} \cdot \begin{bmatrix} E_x^2 \\ E_y^2 \\ E_z^2 \\ 2E_yE_z \\ 2E_xE_z \\ 2E_yE_x \end{bmatrix} \tag{1.24}$$

where $\chi^{(2)}$ is the second-order susceptibility tensor consisting of 18 tensor components.

In literature, eq. (1.24) is often written in the condensed form

$$\mathbf{P^{(2)}} = \chi^{(2)} : \mathbf{EE} \tag{1.25}$$

Since the polarization is quadratically dependent to the electric field strength, this type of process is referred to as a second-order process. When optical electric fields are used, which arise from the same fundamental beam, the second-order process is referred to as second-harmonic generation (SHG). Justification of this name is found in combining eq. (1.25) with eq. (1.5), which yields

$$P^{(2)} = \chi^{(2)} : EE = \chi^{(2)} E_0(e^{ik.r-i\omega t} + cc) E_0(e^{ik.r-i\omega t} + cc) \tag{1.26}$$

$$= 2\chi^{(2)} E_0^2 + \chi^{(2)} E_0^2(e^{2ik.r-i2\omega t} + cc) \tag{1.27}$$

where cc denotes the complex conjugate and is given by $e^{-ik.r+i\omega t}$. The first term is the process called optical rectification, which is frequency independent. Moreover, this term cannot produce electro-magnetic radiation, since the second time derivative becomes zero, as is described by eq. (1.16). This optical rectification leads to a static electric field within a material with nonlinear optical properties. The second term represents the frequency doubling or second-harmonic generation.

The optical phenomenon of second-harmonic generation is illustrated in fig. 1.1. Although the second-harmonic process occurs, the linear processes still take place as well. Specifically for SHG measurements, the linear and higher-order contributions have to be filtered out, prior to detection. The frequency doubling can be observed as the conversion of red light into blue light.

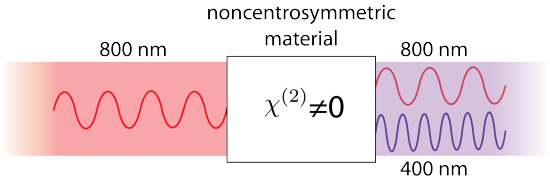

Figure 1.1: Visualization of the second-harmonic generation process in a nonlinear medium

Besides the necessity of high optical electric field strengths, also symmetry considerations are of great importance in nonlinear optics. The symmetry of a structure determines the magnitude of tensor components and determines the number of tensor components which reduce to 0. Due to this symmetry consideration, SHG is a valuable tool for point group characterization and more specific the surface and interface of centrosymmetric material. In order to understand this property, the principle of Neumann can be used to investigate these symmetry considerations. This principle states that the sign and magnitude of physical properties have to remain identical under symmetry considerations. For a structure with an inversion center, the polarization and electric field in eq. (1.21) change sign upon applying the symmetry conditions. In the specific case of the $\chi^{(2)}_{zzz}$ tensor element, eq. (1.21) yields $P^{(2)}_z = \chi^{(2)}_{zzz} E_z E_z$. When considering the inversion center, $-P^{(2)}_z = \chi^{(2)}_{zzz}(-E_z)(-E_z)$, which results in the expression that $-P^{(2)}_z = P^{(2)}_z$ for the $\chi^{(2)}_{zzz}$ tensor element. This expression is only valid when $\chi^{(2)}_{zzz} = 0$ since the physical properties of a material cannot change under symmetry conditions. The same principle can be applied to all tensor elements. Therefore $\chi^{(2)}$ is nonexistent in centrosymmetric materials. Only where this centrosymmetry is broken, SHG can originate. Due to this feature, SHG is widely used to characterize surfaces,[8, 9] and interfaces,[10, 11] since centrosymmetry is always broken.

Using these simplifications, the second-order susceptibility tensor for Si (001), which has a C_{4v} point group symmetry for its surface, becomes

$$\begin{bmatrix} 0 & 0 & 0 & 0 & \chi^{(2)}_{xxz} & 0 \\ 0 & 0 & 0 & \chi^{(2)}_{xxz} & 0 & 0 \\ \chi^{(2)}_{zxx} & \chi^{(2)}_{zxx} & \chi^{(2)}_{zzz} & 0 & 0 & 0 \end{bmatrix} \tag{1.28}$$

while for Si (111), which has a C_{3v} point group symmetry for its surface, this susceptibility tensor yields,[12]

$$\begin{bmatrix} \chi^{(2)}_{xxx} & -\chi^{(2)}_{xxx} & 0 & 0 & \chi^{(2)}_{xxz} & 0 \\ 0 & 0 & 0 & \chi^{(2)}_{xxz} & 0 & -\chi^{(2)}_{xxx} \\ \chi^{(2)}_{zxx} & \chi^{(2)}_{zxx} & \chi^{(2)}_{zzz} & 0 & 0 & 0 \end{bmatrix} \tag{1.29}$$

For these specific point group symmetries, the second-order susceptibilities are evaluated in appendix A.

Some tensor components can be addressed individually when using a polarizer and analyzer during the SHG measurements to define the incident and detected polarization respectively. A commonly used convention for the polarization state of the light is p and s polarization. These polarizations are defined relative to the plane of incidence, perpendicular to the surface and along the propagation direction of the light, as shown in fig. 1.2.

The component of the electric field parallel to the plane of incidence is referred to as p and the component perpendicular to this plane is s. Depending on the polarization before and after the sample, different polarizer-analyzer combinations can be obtained, which in turn address different tensor components. An incident p-polarized wave, can address x and z components, while an s-polarized wave can only address a y component. When the polarizer-analyzer combination is set to S_{in}-P_{out} and correlating it to the indices of $\chi^{(2)}$ in eq. (1.28), only $\chi^{(2)}_{zyy}$ and $\chi^{(2)}_{xyy}$ are probed. Since for a C_{4v} $\chi^{(2)}_{zyy} = \chi^{(2)}_{zxx}$, which is elaborated on in appendix A, both tensor components can be separated with this specific polarizer-analyzer combination. In this manner, different changes to orientation, alignment of molecules,[13] changes in surface reconstruction,[14, 15] or passivation,[16] and diffusion of molecules in porous material can be detected.[17, 18] Also the chirality of structures can be investigated using SHG.

1.1.5 Second-harmonic generation beyond the electric dipole approximation

Due to the electric dipole approximation, the bulk of a centrosymmetric material cannot contribute to the second-harmonic (SH) signal. However, this approximation has to be treated with great care! It was observed that centrosymmetrical structures can still give rise to SHG. So the theoretical model has to be extended to take into account deviations of the bulk properties near the surface. Hence, higher-order contributions (in principle both electric

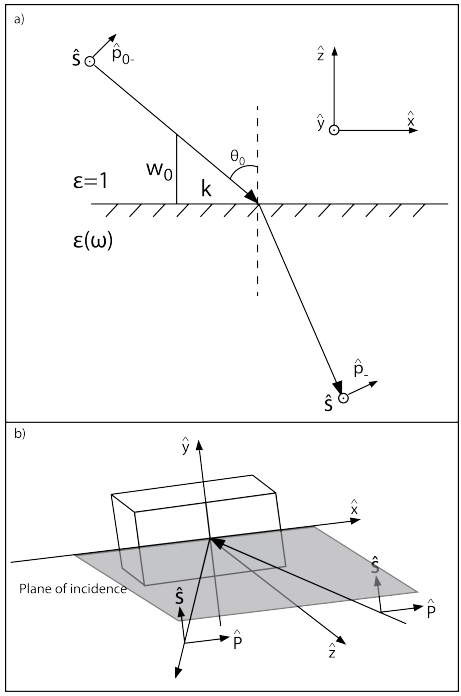

Figure 1.2: Visualization of the beam coordinate system. In a), the beam coordinate system at the surface is shown. Due to trigonometric considerations, a phenomenological theory for electric quadrupole contributions can be proposed. It can be noticed that the p-polarization is defined by field components in $\hat{k}$ and $\hat{z}$. In b), the definition of p and s-polarization is visualized, relative to the plane of incidence.

and magnetic contributions) to the SH signal have to be introduced. So, using second-harmonic generation solely as interface or surface probe can be misleading. The surface contribution to the total SHG signal arises only from the top monolayer of a material. This monolayer is only a few Ångström thick. On the contrary, bulk contribution can arise from the whole escape-depth of the SH signal. Therefore, the bulk and surface contributions can be comparable in magnitude. Second-harmonic generation is an excellent surface probe when the surface contribution is large compared to the bulk. Regrettably, these so-called surface and bulk contributions cannot be separated in cubic centrosymmetric material. When considering a centrosymmetric material, the lowest allowed nonlinear bulk response arises from electric quadrupole or magnetic dipole symmetry.[19, 20, 21] Although the magnitude of these contributions has to be

calculated from microscopic theory, the form that these contributions follow, alike the electric dipole contribution, are determined by the crystal structure. Hence, the bulk contribution can also be described by a phenomenological theory. Initial attempts to present a macroscopic study still relied on microscopic physical origin, which made the theory susceptible for fluctuations in the electric fields normal to the surface and near the surface.[20, 22]

An intuitive description is useful in understanding the electric quadrupole contribution to second-harmonic generation. Imagine two centrosymmetric materials side to side next to each other and a propagating wave through both materials, as is represented in fig. 1.3.

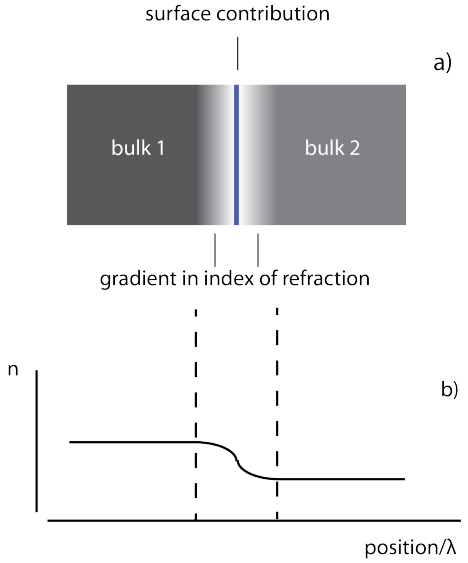

Figure 1.3: Visualization of an electric gradient near an interface. In a), the electric gradient near the interface is indicated as a gradient color. The interface, which can give rise to SHG within the electric dipole approximation is separately indicated. The gradient itself can give rise to SHG, when accounting for higher-order contributions, such as electric quadrupole and magnetic dipole to the total SHG signal. In b), the change in index of refraction n, is illustrated near the interface. Since the index of refraction changes, the incident electromagnetic wave is subjected to a gradient in the structure.

The interface between both materials is indicated in fig. 1.3. As presented in section 1.1.4, this interface breaks the centrosymmetry and thereby can give rise to SHG within the electric dipole approximation. However, when considering the

index of refraction, this image becomes more complex. The index of refraction has to change from the bulk value of one material in a continuous manner to the bulk index of refraction value of the other. This change in index of refraction is illustrated in fig. 1.3. For nonlinear optical phenomena, a gradient in the index of refraction n has to be inserted to obtain a good description of these phenomenon. As a consequence, the applied optical electric field is subjected to a changing index of refraction near the interface. Therefore, the electric field in the medium is also determined by this gradient.

In general, any spatial dependent optical response or so-called nonlocal in electric quadrupolar response can be written in terms of an effective polarization as

$$P_i^{(2\omega)}(r) = \Gamma_{ijkl} E_j^{(\omega)} \nabla_k E_l^{(\omega)} \tag{1.30}$$

where P is the polarization, ∇ the gradient and E represents the electric fields vectors. The gradient is determined in the beam coordinate system, as presented in fig. 1.2. Γ_{ijkl} is a fourth rank tensor, which can be reduced to a 9×9 tensor consisting 81 tensor elements. For a bulk cubic symmetry, such as Si or Ge, the tensor can be simplified by grouping the tensor elements by

$$\Gamma_{ijkl} = a_1 \delta_{ijkl} + a_2 \delta_{ij}\delta_{kl} + a_3 \delta_{ik}\delta_{jl} + a_4 \delta_{il}\delta_{jk} \tag{1.31}$$

where a_i are constants and $\delta_{il}\delta_{jk}$ implies that $i, l \neq k, l$. Using this simplification of the tensor, and using the summation convention, and omitting the frequency symbol for clarity, eq. (1.30) results in

$$P_i^{(2\omega)}(r) = (\delta - \beta - 2\gamma)(\mathbf{E}\cdot\nabla)E_i + \beta E_i(\nabla\cdot\mathbf{E}) + \gamma\nabla_i(\mathbf{E}\cdot\mathbf{E}) + \zeta E_i \nabla_i E_i \tag{1.32}$$

where δ, β, γ and and ζ are phenomenological constants and are parts of the nonlinear susceptibility tensor Γ_{ijkl}. The first three terms are all isotropic with respect to the crystal orientation, while the last one is anisotropic. Moreover, when considering a plane wave excitation, the first term is zero, while the second term cancels due to Maxwell's equations, since $\nabla \cdot E = 0$. Hence, the total electric quadrupolar contribution can be devided in one isotropic term and one anisotropic term. Upon rotating a structure, which changes the orientation of the crystal structure relative to the fundamental beam, any change in bulk SHG is represented by the anisotropic term, while the isotropic term will yield a constant signal over all rotation angles.

This description is used for describing the bulk electric quadrupole contribution in cubic centrosymmetric crystals by the phenomenological theory of Sipe *et al.*[23] They examine the form of the tensor and then transform to the

appropriate coordinate system. Then, the induced nonlinear polarization of the medium is described. Finally, a Green function formalism is used to calculate the generated frequency doubled electric field.[24] Since Sipe *et al.*,[23] other crystal structures considerations in SHG have been reported using the same approach.[25, 26]

This theoretical model was used to validate the physical properties of different structures, mostly semiconductors capped with an oxide layer, to extract surface or interface specific information.

1.1.6 Electric field-induced second-harmonic generation

It has now been demonstrated how second-harmonic generation can be used to characterize surfaces, interfaces and the crystal structure of materials. Moreover, it was observed by Lee *et al.*[27] that at Si- and Ag-electrolyte interfaces in an electrochemical cells, the SH intensity changed with applied dc electric field. Since then, this phenomenon is referred to as electric field-induced second-harmonic generation (EFISH). Si(111)-electrolyte interfaces has been systematically studied by EFISH.[28] Although the first experiments where performed in an electrochemical cell, a metal contact was preferred as electrode, because the strength of the dc electric field which could be applied electrochemically was limited by interface electrochemical reactions. Aktsipetrov *et al.*[29, 30, 31] provided a phenomenological model to describe EFISH in metal-oxide-semiconductor (MOS) structures.

By applying an electric field over a centrosymmetric material, a bulk dipole is created. Then a bulk dipole contribution to the SH signal can occur as well. This bulk dipole contribution can be written as

$$\overrightarrow{P}^{\text{dc-induced}}(2\omega) = \chi^{(3)} \vdots \overrightarrow{E}(\omega)\overrightarrow{E}(\omega)\overrightarrow{E}_{dc} \tag{1.33}$$

where $\overrightarrow{E}_{dc}$ is the electric field, and $\chi^{(3)}$ is a fourth rank tensor. It can be noticed immediately that, when the applied electric field is altered, the SH signal can change as well. A quadratic dependence of EFISH intensity on bias voltage was observed, when an electric field was applied normal to the surface.[28] In this case, eq. (1.33) can be rewritten as

$$\overrightarrow{P}_{\text{eff}}^{\text{dc-induced}}(2\omega) = \chi_{\text{eff}}^{(2)} \vdots \overrightarrow{E}(\omega)\overrightarrow{E}(\omega)\overrightarrow{E}_{z,dc} \tag{1.34}$$

where $\overrightarrow{E}_{z,dc}$ is only oriented in the z-direction, perpendicular to the surface. The subscript eff describes the instantaneous application of the electric field to the structure.[32] Although the third-order nonlinear susceptibility is a fourth

rank tensor, it can be seen as an effective second-order nonlinear susceptibility tensor, which explains the quadratic relationship with incident intensity of the SH signal.

For MOS stacks, the applied electric field induces charge separation in the space-charge region (SCR) of the semiconductor, which results in an internal electric field. This internal electric field is correlated but not the same as the externally applied electric field. It is this internal field which has to be inserted in eq. (5.3) to calculate the exact SH response. However, changes in the internal charge separation can be observed by measuring the nonlinear SH response as function of time. Not all charges migrate equally fast through the structure, so depending on the process, the time response of the SH signal can be fitted to charge migration associated with migration time of the corresponding charges.[16, 33]

To summarize the second-harmonic generation processes in a MOS structure, the total SH response can be written as

$$\overrightarrow{P}_{\text{total}} = \chi^{D} : \overrightarrow{E}(\omega)\overrightarrow{E}(\omega) + \chi^{Q} \vdots \overrightarrow{E}(\omega)\nabla\overrightarrow{E}(\omega) + \chi^{(3)} \vdots \overrightarrow{E}(\omega)\overrightarrow{E}(\omega)\overrightarrow{E}_{z,dc} \tag{1.35}$$

where χ^{D} is the electric dipole or surface term, which reflects the centrosymmetry of the structure and the symmetry of surface or interface (or $\chi^{(2)}$ from eq. (1.25)), χ^{Q} is the electric quadrupole or bulk term, which reflects the crystal lattice and the gradient of the light within the penetration depth (so $\chi^{Q} = \Gamma$ from eq. (1.30)) and $\chi^{(3)}$ corresponds to EFISH. Thus, the second-order response of MOS structures can be explained using these theoretical models.

1.2 Advances in semiconductor processing

Semiconductors and their device applications are abundantly present in our society, more than common intuition would dictate. Not only computers or portable phones utilize semiconductors, satellites, cars, washing machines, etc., use semiconductors to operate as well. Most of these semiconductor devices are integrated circuits or 'microchips' which are a collection of a large number of interconnected electronic components. For the majority of applications, such as memories, microprocessors and logics, which cover up to 80% of the total semiconductor market, these electronic components consist of a metal-oxide-semiconductor field-effect transistor (MOSFET).[34] This MOSFET is a transistor (or initially called the 'transfer resistor') based on the sequence of a metal layer on top of an oxide layer on a semiconductor, which is illustrated in

fig. 1.4. On either sides of this gate stack, a source and drain area is implanted due to a difference in doping.

This type of device is used for its amplifying capability and the property of switching between off and on current through the device. Nowadays, the number of interconnected transistors on one substrate exceeds 5 billion. Also the layout of the transistor itself is changed in order to increase reliability of the device and increase the number of transistors on a single IC.

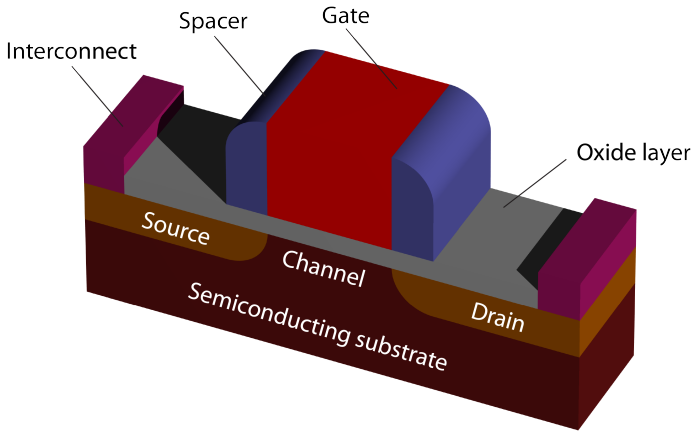

Figure 1.4: The cross section of a simple metal-oxide-semiconductor field-effect transistor (MOSFET) shows the different areas in one MOSFET device. The source and drain are connected by the channel, when the device is turned on. The gate is separated from the channel region by a thin insulating layer. The interconnects are, in a practical point of view, wires which connect different transistors on the same IC. The spacer prevents leakage currents from the gate to the source and drain.

As the name MOSFET suggest, the working principle of a transistor is based on the electric field-effect. The application of a horizontal electric field to the channel, causes electrons to acquire an average velocity $v = -\mu_n \cdot E$ where μ_n is the charge mobility, which is positive for electrons and negative for holes. The

resulting current density can be calculated as

$$j = \rho \cdot v = -N \cdot q \cdot \mu_n \cdot E \tag{1.36}$$

where ρ is the mobile charge density, q the charge per electron and N the number of electrons. The difference in horizontal electric field is obtained by a different doping concentration in the source area compared to the drain area and by applying a potential between those areas. The source and drain are doped with the same type of charge (n for negative doping and p for positive doping). Hence, depending on the doping, electrons (n-doped) or holes (p-doped) will be able to travel from the source to drain. This current can be controlled over time by applying a potential on the gate. The bulk of the semiconductor (and also the channel region when no current is flowing) is doped with a charge of different sign compared to the source and drain doping. So effectively, no negative charge can flow from source to drain through a positively doped medium. Therefore, the amount and sign of the charges in the channel region can be adjusted by an external electric field. This electric field is generated by a potential, which is referred to as the gate voltage, between the gate top electrode, placed on top of the channel but separated from it by an insulating oxide layer, and the source. When a positive field is applied on the gate, electrons are attracted towards the semiconductor/oxide interface. Image now that the source and drain are n-doped, an electron current can flow from source to drain. When the positive electric field on the gate is switched to a negative one, holes will be attracted to the Si/oxide interface. In this case, migration of electrons between source and drain is not possible. So, a change in gate voltage V_g influences the charge density ρ in the channel. Hence, the current density j is determined by V_g. This mechanism is further elaborated on in chapter 4.

Besides this intuitive description of the working principle of a transistor, one can also describe it as a contraction of two junctions or diodes, which are placed back-to-back. Depending on the doping of the Si substrate as well as the source and drain areas, they form pn-np or np-pn junctions. The doping levels are not equal in the different sections of the transistor, which enables conduction through the transistor when the appropriate voltages are applied. For a transistor to conduct, the first junction (when going from source to drain) has to be forward biased, while the latter junction has to be reversed biased. Hereby, two depletion layers are formed at these interfaces. Let us now consider a pnp transistor. In this scenario, the source and drain are positively doped, while the semiconductor substrate is negatively doped. When the first pn junction is forward biased, a large number of holes will flow from the source to the semiconductor substrate. There, these holes will recombine with the doping charges, i.e. electrons from the base. Since the base is only lightly doped, only a small number of holes will recombine with the electrons in the base. Moreover,

the channel region is thin, so most of the holes will be able to diffuse through this region into the drain region. Due to the reverse biased np diode while a negative potential is applied over the base region, the holes are attracted to its terminal. The migrating charges result in a drain current. If one of the junctions in the transistor are not properly biased, charges cannot flow from source to drain, so the transistor is not conducting. Again, the importance of the interfaces, in this case between source and channel as well as channel and drain, are visible. If defects are present at or near these interfaces, charges will recombine there, resulting in no net current from a single transistor. Hence, optimizing these interfaces is of great importance for device performance.

Intuitively speaking, not all the applied gate voltage reaches the semiconductor/oxide interface. However, this is never the case. When a gate voltage V_g is applied between the gate metal and Si, only a part remains across the oxide V_{ox}, while other parts are related to the band bending Φ (eV) and the difference in the work functions between the gate metal W_m (eV) and the semiconductor W_S.[35] Band bending refers to the local changes in the energy offset of a semiconductor's band structure near an interface. Since all interfaces in semiconductors are electrically not in balance or neutral near this interface, the energy of a charge is different near the interface compared to inside the bulk. A change in applied gate voltage will change the amount of charges near this interface, thereby influencing the band bending. The work function of the metal and semiconductor layer is the energy needed to remove an electron from this layer to a point in vacuum. Also this process is influenced by the applied gate voltage. W_S is a function of the electron affinity χ, the band gap E_g, and the dopant versus intrinsic concentration (N_d/N_i) which defines the position of the Fermi level,

$$V_g = \frac{W_m}{q} - \left(\frac{\chi + E_g/2 + k_B T log(N_d/N_i)}{q} \right) + V_{ox} + \frac{\Phi}{q} \tag{1.37}$$

where k_B is the Boltzmann constant and the first three terms determine the flatband voltage V_{FB}, which refers to a voltage at which there is no electrical charge in the semiconductor and, therefore, no voltage drop across it. It should be noted here that the electron affinity is defined for use in solid state physics instead of chemistry. The electron affinity is defined as the energy obtained by moving an electron from vacuum just outside a semiconducting material to the bottom of the conduction band just inside the semiconductor.

The properties of a MOSFET are ideal when V_g is primarily used to influence the charge density in the channel. However, due to the build-up of layers in the system and incomplete oxidation or layer deposition, electrical defects can be introduced in the system. In the latter case, the applied gate voltage not

only influences the charge density, but also the electrical defects are affected by it, which influences the net voltage on the channel. There are a number of charge defects that can occur. First of all, the density of interface traps (D_{it}) and trapped charges (Q_{it}) are located at the semiconductor-oxide interface. The energy states of these defects are located within the bandgap of the semiconductor, and can therefore exchange charges with the semiconductor in a short time period. They exist due to the interruption of the periodic lattice structure at in the interface of a crystal. Moreover, Q_{it} is determined by the Fermi level, so its amount is dependent on the applied gate voltage. This class of defects represent broken hydrogen bonds or dangling bonds at the semiconductor interface, excess oxygen atoms near the interface and impurities. Secondly, fixed oxide charges (Q_f) are located at or near the interface and cannot be influenced by the applied electric field, whereas mobile ionic charges Q_m are mobile under applied gate voltage and even temperature change. Finally, the oxide trapped charges (Q_{ot}) are distributed in the insulating oxide layer and are created e.g. by X-ray radiation.[6]

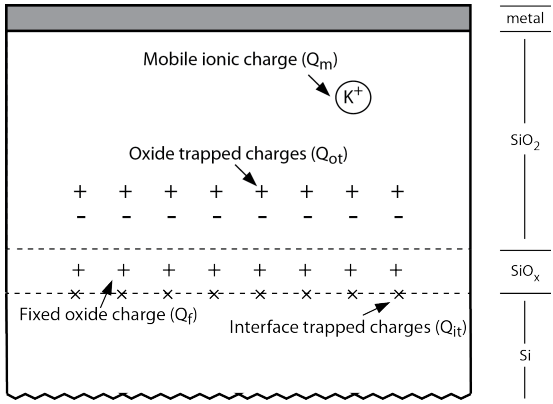

Figure 1.5: Terminology for charges within thermally oxidized silicon. The type of charges, i.e. mobile ionic charges (Q_m), fixed oxide charges (Q_f), oxide trapped charges (Q_{ot}) and interface trapped charges (Q_{it}) are depicted as function of their depth position in the oxide layer. (Figure after Sze.[6])

Considering all these defects, the magnitude of the applied voltage on the channel region is thus reduced. Depending on the doping, migrating electrons or holes from source to drain can generate a current between source and drain, which is determined by the applied voltage between the gate and drain. The current is determined by the doping of the source, drain and the channel area. Hence, optimizing these areas in the MOSFET is of great important. Therefore, a lot of attention is directed towards the optimization of these areas and the

formed channel under device operation. Moreover, a lot of attention in transistor fabrication and design is devoted to the semiconductor/oxide interface, since the defects are present near this interface. Hence, overcoming these defects is key in optimizing the transistor performance. For higher device performance, scaling of transistors devices is possible. Then, more transistors can be integrated on the same size of substrate, which increases the total performance of an integrated circuit.

In order to optimize the semiconductor/oxide interface, different oxide-depositions techniques are commonly used in semiconductor processing. One of these techniques is atomic layer deposition (ALD). As the name suggests, the process is conducted in cycles, depositing in principle one layer per cycle. Each cycle is typically a sequential use of two gas phase chemicals called precursors. When the first precursor, often a organometallic compound reaches the semiconductor surface, it reacts with it in a self-limiting manner. Depending on the preferred high-k dielectric layer, the organometallic compound can be chosen: e.g. trimetyl-aluminum for the deposition of Al_2O_3 or $HfCl_4$ for an HfO_2 resulting oxide layer. The second precursor is an oxidizing agent or acid to react with the organometal to form the oxide layer. Between every cycle, excess material is purged out of the system. The advantage of this oxide-deposition method is the fine control of the oxide thickness, since it is only dependent on the number of cycles during the ALD process. The processing temperature has an influence on the reaction rate at the surface although degradation of the first precursor has to be taken into account. Other parameters than the type of substrate, precursor and temperature, have little influence on the end result of an ALD-deposited oxide layer.

Another technique of depositing oxide layers is molecular beam epitaxy (MBE), although this technique can be used to deposit any single crystal or III-V semiconductors. Under high vacuum conditions, extremely pure metals are heated until they slowly sublime. The metal in the gas phase is directed to the wafer surface, where it can condense and react. In order to oxidize the metal, oxygen or ozone is introduced in the system. The deposition rate can be adjusted in order to deposit material in an epitaxial manner, which corresponds to the conservation of crystal structure of the semiconductor substrate. The molecular beam epitaxy (MBE) system is determined by more parameters compared to the ALD system. The quality of the vacuum, temperature, impurities in the metal, etc can all have a significant influence on the resulting oxide layer.

The final deposition technique, capable of depositing thin layers of material, is chemical vapor deposition (CVD). Although this technique is also able to deposit oxide layers, it is primarily used to deposit epitaxial layers of Si on top of other types of substrates. The chemical vapor deposition (CVD) process has a similar working principle as the ALD process. A semiconductor substrate is

exposed to different gas phase precursors, which can react or decompose on the substrate's surface. Depending on the deposited material, the temperature, carrier gas, pressure in the system and type of CVD system has to be chosen accordingly, in order to obtain epitaxial growth of the deposited layer compared to the substrate. Diverse types of CVD vary from each other in their differences in the initialization of the precursor molecules and reducing side-reactions. Due to the decomposition at the surface, by-products are formed. Those by-products have to be removed form the reaction chamber by a gas flow. In the research presented in this thesis, low-pressure CVD was used for the deposition of a Si capping layer on Ge. In this variant, the low pressure in the system ensures a reduction of the unwanted gas-phase reactions before the precursors encounter the substrate. Moreover, the low pressure improves the film uniformity.

The explanation of all different variants of CVD is beyond the scope of this thesis. However, from this small section, it is clear that a lot of effort is put into optimizing the deposition conditions for oxide layers and other thin layers in general. Optimization of transistor performance by improving the semiconductor/oxide layer is one of the key aspects.

In order to further optimize the transistor performance, different types of materials are considered as channel material. Although the very first transistor was made of germanium as semiconducting material (since Ge was available as a more purified material than Si and Ge is intrinsically better semiconducting material), nowadays, the majority of transistors is fabricated on silicon.[36] The path of Ge-based transistors was abandoned, due to specific interface problems such as passivation problems of the interface, the formation of a brittle and chemically active oxide layer, which results in a larger leakage current. Hence, initially all semiconductor research was directed towards the use of Si in device applications, which in turn boosted the research for a higher purification ratio in Si. The oxide layer was formed by oxidizing the top layer of the silicon, which forms the thermal oxide. This facilitated the production process significantly. An aluminum metal gate was used as gate material until the 1970's. However, to increase the performance of a MOSFET, more and more transistors are fitted onto the substrate. Since speed is determined by the length of the interconnects between different transistors, the size of the substrate is kept constant, while the transistors themselves are minimized. Scaling-down permits improvements at the transistor level by enhancing the on-current. At the circuit level, circuits delay is reduced, which is the time the system needs to go from on-state to their off-state. Furthermore, the density of transistors on an integrated circuit is enhanced, which reduces the economical cost per transistor. Due to the continuous scaling-down of the transistor dimensions, Si, SiO_2 and the poly Si metal gate encounters its fundamental limits, due to their physical properties. New technologies with respect to material research are emerging to overcome

the scaling issues and continue the improvements at the transistor and circuit level. These improvements are based on constant field scaling: channel mobility increase, reduction of potentials, reducing the gate delay, increasing the doping concentration and reducing the physical dimensions of the IC.

By increasing the channel mobility, the on-current is increased while simultaneously the delay of the circuit is reduced. This can be done by introducing Ge in the channel, since the electron and hole mobility is larger and the bandgap is smaller compared to Si. Often a combination of Si and Ge is used to obtain good growth conditions on the Si substrate, due to the 4% crystal volume mismatch between Ge and Si. Due to the mismatch between the crystal structure of Si and Ge, strain is introduced in the system. This straining of the Ge channel will increase the mobility of the carriers, which also can be obtained by mixing Si and Ge.[37] The strain of the material is dependent on the thickness of the Si/Ge layer. After a certain thickness, the strain will be reduced. The critical thickness for plastic relaxation for tensely strained Si layers grown on Ge has been discussed by several authors.[38, 39, 40]

Since Ge is hard to passivate with its native oxide, high-k dielectrics have to be used in the MOS structure. However, these high-k dielectrics often exhibit a high defect density near the semiconductor-oxide interface. Because of the high dielectric constant, tunneling of electrons and holes is reduced, which reduces the leakage current and minimizes the power consumption.[6] By optimizing the interface between the oxide and the semiconductor layer, the MOS device will yield better electronic properties. For Ge channels, passivation can be done by means of sulphur.[41, 42]

Changing the channel material from Si to Ge is not the only possible way of continued scaling down of the transistor dimensions according to the ITRS roadmap.[43] Compound semiconductors, which consist of at least two elements of different groups in the periodic table, have great potential to replace Si as channel material in certain applications where a higher saturated electron velocity and higher electron mobility are required. Hence, the power of these types of devices are larger compared to Si as semiconductor. The most common compound semiconductor is GaAs. This III-V semiconductor has the additional advantage that it has a high resistance to radiation damage, which makes it the ideal material to be used in space electronics.

Besides optimizing the semiconductor/oxide interface in front-end-of-line processing, also the doping of source, drain and the channel areas play an important role. This can be learned from eq. (1.37), since the division of the gate voltage over the different layers in the MOSFET is influenced by the doping concentration.

1.3 Why semiconductor research needs nonlinear optics

In MOSFET research, one strives to process better devices. This is mostly obtained by scaling down device dimensions. When shrinking these dimensions, different problems arise and one is challenged to overcome these obstacles. A number of challenges are listed below:[44]

- Sub-threshold leakage current
- Threshold voltage variation
- Carrier mobility degradation
- Hot carrier effects
- Direct source to drain tunneling
- Direct tunneling gate leakage current
- Gate depletion
- Suppress on-current
- Reverse-biased junction leakage current
- Surface BTBT current

To overcome some of these challenges in MOSFET research and to continue the down-scaling of the transistor dimensions, surface and interface specific characterization techniques are employed to optimize transistors. A technique such as SHG is highly suited for this type of investigations.[45, 46] As explained in section 1.1.4, SHG is forbidden in centrosymmetric media within the dipole approximation. Centrosymmetry is broken at surfaces and interfaces in elemental semiconductors, resulting in a high interest for implementation of SHG in semiconductor research. In literature, it has been reported that SHG is a valid tool for studying interfaces in semiconductors.[47, 48] Most of the research has been performed on Si. Rotational anisotropy SHG on Si provides insight in surface and interface properties, such as strain,[49, 50] roughness,[51, 52] and surface reconstruction.[14] For the latter observation, a 7×7 surface reconstruction was observed on top of the Si bulk symmetry. Also high-k dielectric layers, such as Al_2O_3,[53, 54] HfO_2 [55], and ZrO_2 have been examined by SHG.[56] Depending on the composition of the oxide layer, differences in interface properties were addressed. Spectroscopic SHG revealed that when charges are present in the oxide layer, the resonance peak of the SH response shifts. Compound semiconductors form a difficult structure to examine with SHG, since they are not centrosymmetric, which results in a large

bulk contribution compared to the surface contribution. By using theoretical calculations such as *ab initio* DFT calculations, it is possible to unambiguously identify spectral features in both linear reflectance differential spectra and nonlinear SHG optical spectra of the Si/SiO_2 interface with local atomic oxygen-related configurations. The combination of calculating the linear and nonlinear spectra provides a detailed picture of the Si/SiO_2 interface at the atomic level.[57]

Besides the optimization of interface properties, it is also important to characterize the properties of a MOS structure, i.e. when applying a potential to the structure. The measurement setup represents the working principles of a MOSFET.Applying a potential will influence the amount of charges in the channel region. When applying an external electric field over the whole MOS structure, the electric field-induced equivalent of second-harmonic generation, electric field-induced second-harmonic generation (EFISH) can be measured.

When including EFISH, the electric field near the interface from externally applied voltage,[58, 59] or doping can be characterized.[60, 61] A thorough characterization of the Si-SiO_2 interface in a MOS configuration has been performed, accompanied with a phenomenological theoretical model by Aktsipetrov *et al.*[29] Also, the charge carrier trapping near the interface can be investigated by means of EFISH.[62, 63] It was demonstrated by Chang *et at.* that the flat-band voltage can be determined by SHG.[64] Combining EFISH and second-harmonic spectroscopy can investigate the influence of doping on the resonance in the second-harmonic generation spectra when the wavelength of the fundamental beam is tuned.[60, 65] Also amorphous silicon films were electrically characterized by nonlinear optical techniques.[66] By using high energy lasers, the energy of a photon can be converted in the creation of an electron-hole pair in the semiconductor. As a result, a potential is created over the MOS structure, which in turn results in an EFISH contribution to the total SH signal. This effect can be used to investigate buried oxide interfaces, by providing information on surface roughness, strain, defects, and metallic contamination.[67] Unlike investigating the interface properties of compound semiconductors by means of SHG, the electrical properties can be probed by EFISH.[68]

1.3.1 Research objectives

We based our work on similar structures and techniques as presented in the research listed above. The global research goal of this thesis is to characterize interfaces and electrical properties of semiconductor devices by means of nonlinear optical techniques and to evaluate SHG and EFISH as possible in-line characterization tools in semiconductor industry. The surface sensitivity

of SHG can be exploited in different areas in semiconductor processing. By using the knowledge of the Si/SiO_2 interface in a traditional MOS gate stack, other types of gate stack assemblies were investigated. One of the promising new solutions in passivating Ge, is growing a thin Si capping layer on top of Ge, which in turn can be partially oxidized. Therefore, one can use the advantage of the good native oxide of Si, compared to Ge. We investigated in chapter 2 if SHG is able to probe different interface properties when the oxide is grown using different oxidant agents in analogy of the research on other high-k dielectric layers,[53, 54, 55, 56] and if so, that a difference in resulting Si cap was detectable. Furthermore, we investigate to which extent and how the carrier gas and the operating temperature influences the interface quality in chapter 3. If different thicknesses of oxide layers are grown on top of a semiconductor, is there a large influence of these layers on the total SHG response of a gate stack? This is investigated in chapter 4.

Applying an external electric field to the MOS gate stack enables us to investigate the charge migration inside the structure during MOS operation, as was demonstrated in EFISH experiments reported in the previous section. In chapter 5, we utilize EFISH to observe tunneling of holes through the oxide layer of a MOS structure, while an external electric field was applied by corona poling. In chapter 6, we investigate if charge migration also can occur from the oxide layer towards the Si/SiO_x interface instead from substrate to oxide layer.

The ITRS roadmap makes prognoses even beyond the Ge and compound semiconductor devices. Since the discovery of graphene in 2004,[69] a lot of effort has been put in the incorporation of graphene in semiconductor devices.[70] Graphene can be exploited as plasmonic material,[71, 72], electronic material,[73] optical material,[74] and fluorescent material.[75, 76] Also nonlinear optical effects are reported in graphene such as second-harmonic generation,[77, 78] third-harmonic generation,[79, 80] nonlinear broadband luminescence,[81] and linear optical properties.[82] In the presence of a strong magnetic field, the nonlinearity increases dramatically.[83] Recently, graphene itself has proven to have good imaging properties for biological samples.[84] Since the production of large high-quality graphene areas remains challenging, imaging of graphene is often done by microscopy techniques.[44]

Following from these findings, our attention turned to graphene as well. Due to the 2D nature of graphene, we investigated if SHG can be used to characterize this type of material, which is elaborated on in chapter 7. Since nonlinear imaging of graphene proved to be tedious, a novel detection manner for SHG was developed and presented in chapter 8.

Chapter 2

Second-harmonic generation reveals the oxidation steps in semiconductor processing

As explained in chapter 1, the interface between the semiconductor layer and the insulating layer is of great importance for the device operation of a metal-oxide-semiconductor field-effect transistor (MOSFET). Therefore, a technique is required to characterize specifically the interfaces of a metal-oxide-semiconductor (MOS) gate stack. For this, we used second-harmonic generation (SHG), since it is very sensitive in determining the surface and interface properties of structures. We continued the research on the Si/SiO_2 interface, which has been extensively investigated earlier and followed the same approach. However, in our case, the Si layer was grown on top of a Ge layer, since Ge has poor native oxide properties. In this manner, the good native oxide properties of Si could still be utilized. Additional to the Si/SiO_2 interface, a Si/Ge interface was introduced and could be characterized by SHG.

The Si/Ge wafers with HfO_2 layer were manufactured at imec by dr. Benjamin Vincent. I performed the SHG measurements and analysis of the data. I submitted our findings to Journal of Applied Physics where our manuscript was accepted.

M. K. Vanbel, V. K. Valev, B. Vincent, V. V. Afanas'ev, J.-P. Locquet, S. Van Elshocht, M. Caymax, T. Verbiest,
Second-harmonic generation reveals the oxidation steps in semiconductor processing
Journal of Applied Physics, **111** (6), 064504 (2012).

In order to comprehend the different chapters in this thesis and understand their connections, a small section is added to the introduction of each chapter where reflections are made on the performed research. These reflections follow from the chapter itself.

Due to the sequence of a Si layer on top of a Ge layer, Ge can diffuse or segregate into the Si layer due to the elevated temperature of the deposition process. This segregation of Ge into the Si layer is an exchange of a Si atom to a Ge atom. Therefore, the Si layer consists of segregated Ge at different depths. Depending on the thickness, accompanied with a cleaning step, a different amount of Ge remains in the Si capping layer. Therefore, when this layer is partially oxidized, a difference in effective oxide thickness is observed, since Ge oxidizes more easily compared to Si. Hence, more Ge segregation will result in a thicker oxide layer and more of the Si layer will be consumed. This phenomenon is observed by second-harmonic generation. In fact, the segregation can be correlated to the effective oxide thickness.

Also a change in operating temperatures for different precursors is used. Since trisilane requires less energy to decompose, the trisilane CVD process is performed at a lower temperature compared to the silane case. Therefore, a difference in Ge segregation is also expected between these structures. The difference in modulation in the polarization patterns in the SHG response could be an indication for this.

Experiments on similar structures are presented in chapter 3. There, a correlation between the chapters considering the interface between Ge and Si and its oxide is presented.

Abstract

Monitoring oxidation steps is an important factor during the fabrication of semiconductor devices, because transistor performance can be greatly affected by defects in the passivation layer. As an example, we discuss the formation of a gate stack in metal-oxide-semiconductor field-effect transistor (MOSFET) devices using Ge as an alternative channel material. Building an MOSFET gate stack on Ge requires passivation of the interface between the dielectric (typically a high-k material such as Al_2O_3 or HfO_2, grown by means of atomic layer deposition (ALD)) and the Ge channel. Such passivation can be obtained from a very thin Si layer, epitaxially grown on the Ge. The Si surface receives an oxidizing clean (O_3 or wet chemical clean) before the ALD step. In this work, second-harmonic generation (SHG) data are presented for silicon layers with varying thickness, grown with either trisilane (Si_3H_8) or silane (SiH_4) and with various cleaning steps. The trend in second-harmonic (SH) response upon azimuthal rotation of the samples was comparable for both silane and trisilane as Si precursor. Our results show that upon oxidation, the SHG intensity reduces, most likely due to a reduction of the amount of crystalline Si, which is converted to SiO_2.

2.1 Introduction

Transistor performance heavily relies on the condition of the interfaces in the gate stack close to the channel. Therefore it is of the utmost importance to understand how the different steps of the manufacturing process influence the electrical passivation of these interfaces. Especially, for alternative channel materials such as Germanium (Ge), this has been shown to be a serious issue.[85] As a potential solution, the use of a thin Si cap layer on top of the Ge is being considered.[86]

In the past few years, research in microelectronics has been driven by scaling down the dimensions of the transistors in integrated circuits, often in agreement with Moore's law.[87, 88, 89] This has brought significant challenges for both the manufacturing process and the characterization techniques.[90]

As opposed to Si channel devices, where Si forms a natural interface with SiO_2 as dielectric or interfacial layer, the use of Ge implies additional process steps to grow the dielectric. Moreover, alternative methods of passivation would need to be employed, due to the limitations of GeO_2. Therefore, the use of a thin Si cap layer on top of the Ge is investigated so that the standard passivation schemes known for Si can be considered. However, one of the problems associated with integrating a silicon cap is the unwanted induced

segregation of underlying Germanium into the silicon cap. This segregation reduces the passivation capacity of the silicon cap. Often, an additional wet cleaning step is needed to reduce the effect of segregation. Clearly, the impact of the Si cap layer thickness and the presence of the additional interfaces between e.g. Ge and Si needs to be assessed.[49, 91, 92]

Although, there are many known techniques to analyze surfaces and to measure layer thickness[86] (e.g. spectroscopic ellipsometry (SE), X-ray photoelectron spectroscopy, total X-ray fluorescence, Rutherford backscattering spectroscopy, SE combined with reflectometry), they all have associated limitations with respect to sensitivity, depth resolution or penetration depth, considering a gate stack consisting of $Ge/Si/SiO_2$ on Si. Furthermore, the latest research in semiconductor industry is focusing on studying specific layers or interfaces embedded in the transistor rather than surface characterization.

A technique such as second-harmonic generation (SHG) is highly suited to investigate buried interfaces.[46, 67, 93] SHG is an optical technique with interface sensitivity down to the atomic level.[94] Additionally, the technique has been intensively used in the past to characterize silicon.[58, 95] For instance, the optimization with respect to defects at the Si/SiO_2 interface of silicon-on-insulator (SOI) wafers have been investigated using electric field-induced second-harmonic generation (EFISH).[48] Attempts to fully characterize the thickness dependency of SOI wafers have also been made. This research was performed on miscut wafer substrates.[96] The oxidation process itself has been investigated as well by SHG. Heinz *et al.*[97] showed that time-dependent second-harmonic generation (TD-SHG) intensity changes as a function of oxidation time of the top layer of a Si(111) substrate.

Within the electric dipole approximation, SHG is inherently sensitive to non-centrosymmetry, e.g. at interfaces and surfaces. Due to its extreme sensitivity, second-harmonic generation is an ideal candidate for interface probing, allowing the characterization of the passivation of the channel beneath a dielectric, without destroying the sample. Hence, the interface can be probed as such or can be characterized upon oxidation.

This paper presents SHG results of silicon cap passivated germanium upon azimuthal rotation of the samples for different thicknesses of silicon cap and for different oxidation steps. Due to the sensitivity of the SHG measurements, the oxidation steps and Si growth are identified and the standard deviation is compared with the error on SE measurements.

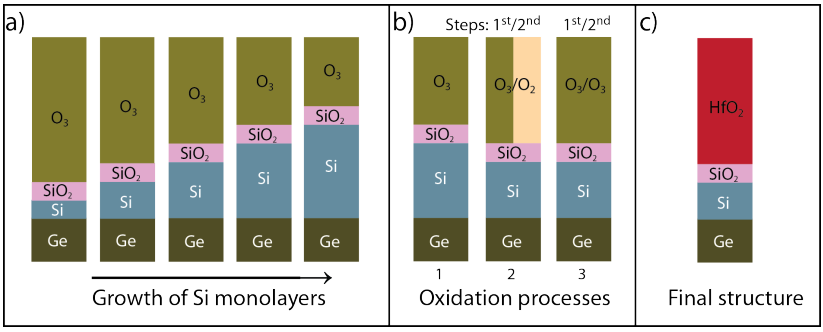

Figure 2.1: The growth of the samples and dependency of silicon thickness on the oxidation. In a), a schematic diagram of the monolayer growth of silicon on top of germanium is shown. The amount of ozone is the same for all cases. In b), a schematic diagram of the second oxidations is displayed. For samples 2 and 3, the first oxidation is an ozone step, followed by an HF clean, which etches the oxide layer away. Thereafter, an oxidation in ambient O_2 or O_3 is performed. The thickness of the silicon layer decreases, because of the etching step. In c), the final structure of the investigated samples is shown.

2.2 Sample preparation

The samples were treated differently to obtain different thickness of the silicon caps and to vary the oxidation conditions. The additional oxidation step to the standard cleaning process is a wet cleaning step prior to an ALD step, enabling a smoother deposition of dielectric material. The presence of Ge in the Si cap, due to segregation during the Si deposition, can cause the silicon cap to oxidize faster, resulting in a larger oxidation depth. More specific, in the initial part of the sample fabrication, Ge was deposited on a (001) cut silicon wafer. Thereafter boron was implanted with a concentration of 10^{16}cm^{-3} at the surface to obtain a p-type (001) Ge semiconductor. Because Ge is a good candidate for use as n-MOS material, the research on germanium is often performed on p-type Ge. An annealing step at 600 °C concluded the preparation of the germanium wafer. Prior to the Si cap deposition, the surface of the wafer was prepared with a one minute treatment with a NH_4OH, H_2O_2 and H_2O in a 1:1:5000-mixture, followed by a 5min de-ionized water rinse. Subsequently, the wafers received a H_2 bake at 650 °C. Silane (SiH_4) or trisilane (Si_3H_8) were used as silicon precursors at deposition temperatures of 500 °C and 350 °C, respectively. The thickness of the Si cap layer, ranging from 2 monolayers (MLs) to 6ML in steps of $\sim$ 1ML, was controlled by varying the deposition time (fig. 2.1). The thickness of the Si layer was measured with SE on a KLA Tencor

F5 spectroscopic ellipsometer. Thicknesses were measured immediately after unloading the samples from the reactor, i.e. without extensive air exposure. The silicon thickness extracted from spectroscopic ellipsometry in 10^{-9}m is transformed into a number of MLs, assuming 1ML $\simeq$ 0.13nm. For all samples, part of the Si cap was oxidized in ozone for 60s, forming a native oxide on top. In addition, two samples of 5.4ML (grown from Si_3H_8) and two samples of 4.2ML thick (grown from SiH_4), were further oxidized in a 1 ppm ozone-water solution for 60s followed by a water rinse of 5min and a cleaning step. This step includes a 120s 0.5%HF-dip and a 5min water rinse. After an HF-dip, all oxide is removed from the surface. One sample of the 5.4ML and 4.2ML samples for Si_3H_8 and SiH_4 respectively is oxidized using ambient oxygen, while the other is oxidized using ozone. The second oxidation step is relevant for reducing the Ge segregation in the silicon layer prior to the ALD process.[86] All samples underwent a Marangoni drying procedure.[98] Finally, an 8nm HfO_2 layer is deposited on top of all samples by atomic layer deposition, to prevent further oxidation of the wafer. This HfO_2 is formed using $HfCl_4$ as Hf-precursor and water as oxidizing agent in the ALD process. An overview of the samples with different silicon cap thicknesses is given in table 2.1.

2.3 Experimental methods and theoretical description

The second-harmonic generation experiments are carried out using a Titanium-sapphire (Ti-Al_2O_3) laser at a wavelength of 800nm with a power output of 130mW, with a pulse width of approximately 120fs and a repetition rate of 82MHz. The average power density after focusing is approximately 2kW/cm^2.

The beam is initially guided through a half-wave plate and a polarizer to control its polarization. Thereafter the beam passes through a RG 665 filter and is then focused using an achromatic doublet. Subsequently, the beam is incident on the sample at an angle of 45 °. The sample is mounted on a rotation stage for azimuthal rotation of the sample. The outgoing beam is collimated with an achromatic doublet and then the beam passes through a BG 36 filter allowing light of 400nm to pass, while the 800nm fundamental beam is blocked. When the signal has passed an analyzer, the light is detected by a photomultiplier tube. From different polarizer-analyzer configurations, physical parameters can be extracted upon rotation of the sample. In this experiment, the position of the polarizer and analyzer can be s-polarized or p-polarized, meaning that the electric field is aligned perpendicular or along the plane of incidence, respectively.

For intense electromagnetic fields, such as those generated by a pulsed laser beam, the induced polarization is no longer linearly proportional to the incident electric field $E(\omega)$.[99] Instead, the induced polarization contains higher harmonics of the frequency ω. Among these, the second-harmonic polarization $P(2\omega)$ at the double frequency can be written as the sum of a dipolar $P^D(2\omega)$ and a quadrupolar $P^Q(2\omega)$ polarizations:

$$P(2\omega) = P^D(2\omega) + P^Q(2\omega) = \chi^D : E(\omega)E(\omega) + \chi^Q : E(\omega)\nabla E(\omega) \qquad (2.1)$$

where ω is the frequency of the light $E(\omega)$ and $E(\omega)$ the electric fields of the incident light and χ^D and χ^Q indicate the dipolar and the quadrupolar nonlinear susceptibilities, respectively. The susceptibility χ^D is a third rank tensor, which consists of 27 components, but it can be considerably simplified based on the symmetry considerations of the sample. In our case, the Si (001) surface and interfaces are four-fold symmetric in the plane of the sample, hence the susceptibility tensor reduces to:[23, 99]

$$\chi^D = \begin{bmatrix} 0 & 0 & 0 & 0 & \chi^{(2)}_{xzx} & 0 \\ 0 & 0 & 0 & \chi^{(2)}_{yyz} & 0 & 0 \\ \chi^{(2)}_{zxx} & \chi^{(2)}_{zyy} & \chi^{(2)}_{zzz} & 0 & 0 & 0 \end{bmatrix} \qquad (2.2)$$

where $\chi^{(2)}_{zxx} = \chi^{(2)}_{zyy}$ and $\chi^{(2)}_{yyz} = \chi^{(2)}_{xzx}$. By changing the polarizer-analyzer configuration, different tensor components can be addressed.
For a (001)-oriented lattice, in the S_{in}-P_{out} polarizer-analyzer configuration, in χ^D a single tensor element is addressed; the dipolar contribution is therefore a constant: P^D_{iso}.
The quadrupolar polarization has the following form:[95]

$$P^D(2\omega) = (\delta - \beta - 2\gamma)(\mathbf{E}\cdot\nabla)E + \beta E(\nabla\cdot\mathbf{E}) + \gamma\nabla(\mathbf{E}\cdot\mathbf{E}) + \zeta\sum_i \hat{e}_i E_i \nabla_i E_i \quad (2.3)$$

For clarity, we omitted the frequency dependence symbol of the fundamental fields. The vectors $\hat{e}_i$ are unit vectors along the crystallographic directions and β,γ,δ,ζ are linear combinations of the χ^D tensor elements. Considering a single plane-wave excitation, the first term in eq. (2.3) is zero, while the second term cancels due to Maxwell's equations. For S_{in}-P_{out}, the value of the third term is a constant: P^Q_{iso}. The fourth term is anisotropic and, within the framework

of Sipe's theoretical model,[23] in the beam coordinate system $\hat{s}\hat{k}\hat{z}$, it can be expressed as:

$$P^{Q}_{P-out,anis}(2\omega) = in\tilde{\omega}[f_c(f_s\Gamma'^{a}_{2121} - f_c\Gamma'^{a}_{2131}) + f_s(f_s\Gamma'^{a}_{3121} - f_c\Gamma'^{a}_{3131})]E'_l E'_l \quad (2.4)$$

where n is the complex refractive index of the medium, $\tilde{\omega} = \omega/\omega cc$, $f_c = c/cnn$, $f_s = k/k(n\tilde{\omega})(n\tilde{\omega})$, k is the length of a unit vector $\hat{k}$, while Γ'^{a} and E' are both expressions in the $\hat{s}\hat{k}\hat{z}$ coordinate system, of on the one hand side, linear combinations of the χ^Q tensor elements and on the other, the fundamental electric field.

Evaluating eq. (2.4)leads to:

$$P^{Q}_{P-out,anis}(2\omega) = in\tilde{\omega}\frac{f_c f_s[1 - cos4(\phi+\theta)]}{4}E'_l E'_l = P^{Q}_{anis} sin^2 2(\phi+\theta) \quad (2.5)$$

where P^{Q}_{anis} regroups all constant terms, ϕ is the angle upon azimuthal rotation and θ is the phase.

Finally, the intensity of the SHG signal in the S_{in}-P_{out} polarizer-analyzer configuration becomes:

$$\begin{aligned} I_{Sin-Pout}(2\omega) &\propto |P^{D}_{iso} + P^{Q}_{iso} + P^{Q}_{anis} sin^2 2(\phi+\theta)|^2 \\ &\propto |I_0(2\omega)| + |B| sin^2 2(\phi+\theta) + |A| sin^4 2(\phi+\theta) \end{aligned} \quad (2.6)$$

where $I_0(2\omega) = (P^{D}_{iso} + P^{Q}_{iso})^2$, while $B = 2(P^{D}_{iso} + P^{Q}_{iso})P^{Q}_{anis}$ and $A = (P^{Q}_{anis})^2$. The latter term is small with a maximal signal of 10 counts/s, verified by SHG measurements in the S_{in}-S_{out} configuration. In similar systems, the dominating contribution has been reported to have electric-dipole character, originating from the surface.[22] Nevertheless, for Si (001) a large electric-quadrupole response from the bulk has also been reported.[100] Moreover, in some cases it has been shown that contributions from the electric dipole, electric quadrupole and/or magnetic dipole could be inseparable.[100, 101]

Note that we did not include an EFISH term in the total SHG intensity. A possible EFISH contribution is not likely to contribute upon azimuthal rotation. First, the sample was characterized using highly intense laser light, which saturates the photo-induced carriers and defects.[102] This EFISH contribution can be considered to be represented by I_0 in eq. (2.6) and is considered constant for all samples. In addition, the inherent EFISH contribution arising from

fixed charges at the interface should be constant, due to the 8nm HfO_2 on top of the total structure, because the total thickness of all oxide layers is approximately constant. The defects, which give rise to an internal electric field, are predominantly present at the SiO_2/HfO_2 interface.[103] The number of charges at the interface are invariant upon growing more Si because of the similarities in the growth procedure. Hence, the voltage drop over the oxide layer is constant.

2.4 Discussion and results

The SHG experiments were conducted for four different polarizer-analyzer configurations, namely P_{in}-P_{out}, P_{in}-S_{out}, S_{in}-P_{out} and S_{in}-S_{out}, however only the S_{in}-P_{out} configuration is presented. This configuration is the most informative one, since it only depends on one electric-dipole allowed susceptibility component χ_{zyy} (representative for the surface) in addition to a bulk contribution. Note that we assume that the surface is not reconstructed during deposition of subsequent layers.

The SHG measurements were performed for all samples, grown as specified above. The S_{in}-P_{out} configuration for the samples with a native oxide are presented in fig. 2.2, while the samples oxidized with ozone are shown in fig. 2.3. The SHG intensity is given as a function of the rotation angle of the sample. From fig. 2.2, it can be noticed that the overall intensity of SHG increases with an increasing number of silicon monolayers. The rise in SHG signal is observable for both SiH_4 and Si_3H_8 as Si precursors.
We summarize the possible mechanisms which can induce this increase in SHG intensity. First, due to the strain in the Si interlayer, the tiny increase in material, can have a drastic increase in SHG signal.[49] Second, screening of the Ge/Si interface can explain this behavior when the Si/SiO_2 interface is grown. Because the Ge/SiO_2 interface generates less second-harmonic than the Si/SiO_2 interface, upon deposition of Si, the "top" interface can screen the "bottom" one. This has been reported previously on similar structures fabricated from other materials.[104, 105] Especially, if the tensor components of these interfaces have opposite sign, the intensity will first decrease and then increase, which can be observed in our experiment. Third, the possibility of contributing quantum well states should not be excluded.[106, 107] Due to a change in thickness, the energy band diagram can drastically change, hereby changing the SHG response intensively. Fourth, segregation of Ge in the Si layer is possible and can greatly affect the second-harmonic generation.[108] Those effects can all have an influence on the SHG response.

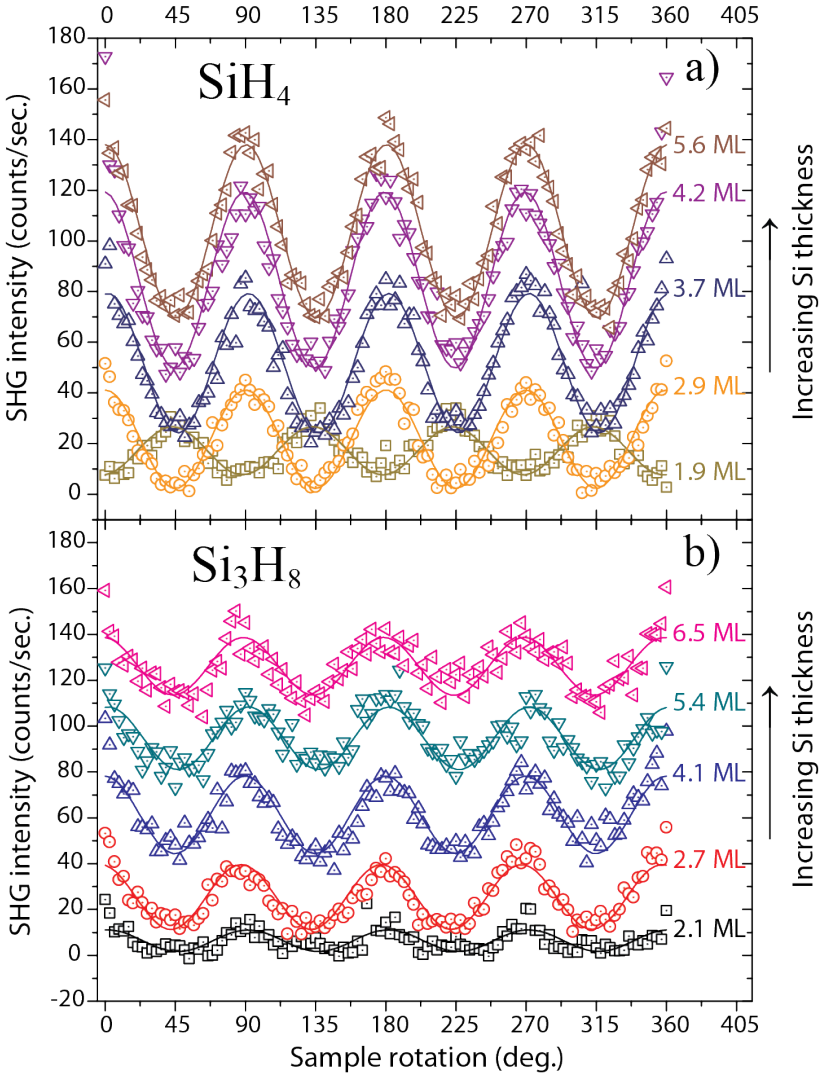

Figure 2.2: SHG intensity as a function of sample rotation, for various Si thicknesses (in monolayers). The SHG intensity in the S_{in}-P_{out} polarizer-analyzer configuration as a function of sample rotation is shown in a) and b) for all samples grown with SiH_4 and Si_3H_8 precursors respectively. Increasing Si thickness results in an increase in SHG intensity for both precursors. The lines are fittings to eq. (2.6).

From fig. 2.2, it can be noticed that the phase of the 1.9ML sample prepared with SiH_4 is shifted 45 ° compared to the other silicon cap thicknesses. Similar phase shifts have been reported before from Si/oxide,[48, 102] and Si/metal interfaces,[109] and have been attributed to EFISH. Can in our case the phase shift be attributed to EFISH? When measuring the SHG response of semiconducting samples, the high intense laser light can induce charges, which accumulate at the surface or interfaces. These accumulated charges can lead to an internal field and hence EFISH. The samples were subjected to the high intensity laser beam well before starting the experiment. Hence, the EFISH arising from charging of defects is approximately constant when the measurement starts. Consequently, we believe that the phase shift in fig. 2.2 is related to the presence of different interfaces during Si growth.[110] More specifically, upon increasing the thickness of Si, first the Ge/SiO_2 interface forms then the Ge/Si one. Note that the phase shift in fig. 2.2a is not observed for the layer grown with Si_3H_8, see fig. 2.2b. However, the thickness of the thinnest silicon cap layer of both precursors differs by 0.2ML. This indicates that between 1.9ML and 2.1ML, a silicon onset is introduced, while before the layer is fully oxidized. Because the oxidation process is well controlled in length and due to the presence of HfO_2 layer, the thickness of the SiO_2 layer is thinner than grown as a native oxide in ambient atmosphere.

It should be noted that there is a significant difference in the anisotropic modulation in fig. 2.2. This difference can be attributed to the different growth conditions used for the different precursors. The growth temperature for trisilane is 350 °C while, for silane, the process can only occur at 500 °C. At lower temperatures, the amount of defects introduced in the structure increases. It appears that the enhancement in defect density decreases the anisotropic modulation.

In fig. 2.3, we show the influence of oxidation on SHG intensity. The first sample was a silicon cap passivated Ge wafer with native oxide without an HF-dip (Sample 1). The other samples were oxidized in ozone for 60 seconds and subsequently the oxide layer is etched away. Next, the samples were exposed to ambient atmosphere (Sample 2) or exposed to ozone for 60 seconds (Sample 3). It is clear that the three samples show a drastically different SHG response and that oxidation decreases the overall SHG intensity emanating from the sample. Furthermore, we can clearly distinguish between O_2 and O_3 oxidation. The fact that the SHG intensity decreases upon further oxidation, strongly suggests that the SHG signal originates from the silicon. Indeed, the etching step and oxidation step will remove Si and based on the results in fig. 2.2, this is accompanied by a strong decrease in SHG intensity. This is in agreement with previous studies of the SHG intensity decrease upon oxidation time.[97] Due to the presence of strain in the Si interlayer, the change in SHG signal can

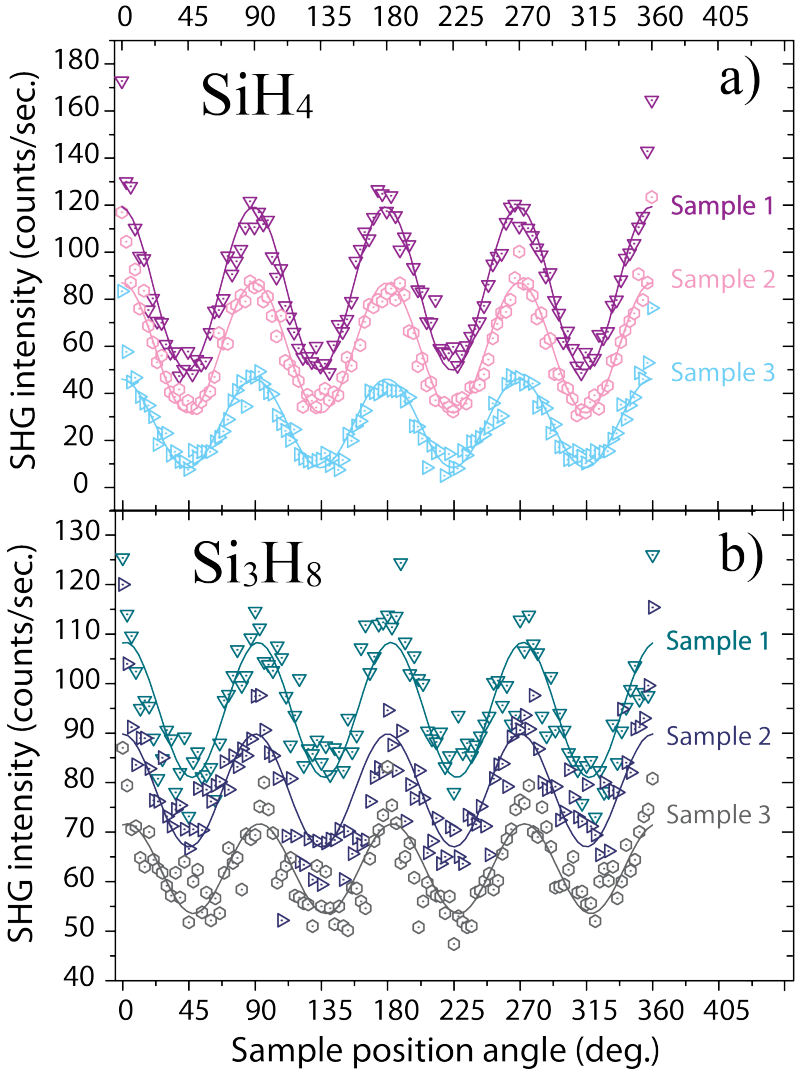

Figure 2.3: SHG intensity as a function of oxidation steps. The effect of oxidation on the SHG intensity in the Sin-Pout polarizer-analyzer configuration is shown in a) and b) for SiH_4 and Si_3H_8 precursors, respectively. Sample 1 is a silicon cap passivated Ge wafer with a native oxide. The other samples are oxidized first in ozone and then the oxide layer was etched away. Next, the samples were oxidized in ambient atmosphere (sample 2) or in ozone (sample 3). The lines are fittings to eq. (2.6).

be enhanced.

This thickness dependency can be more clearly seen in fig. 2.4, where the isotropic contribution of the total SHG signal, extracted by fitting the total SHG signal using eq. (2.6), is plotted as a function of number of monolayers determined by ellipsometry after each oxidation. The difference in SHG response from the SiH_4 grown silicon layer and the Si_3H_8 can be noticed here as well. A very likely explanation for this difference is the variation of Ge segregation. In silane grown Si caps, the segregation is larger than in the trisilane grown structures. Hence, after silicon cap passivation, more Ge is segregated in the silane-formed silicon layer than the trisilane-formed layer. Segregated Ge atoms accumulate at the Si/SiO_2 interface. Upon oxidation, the presence of Ge on the Si surface leads to deeper oxidation of the Si cap. When cleaned with HF, more material is removed and a thinner silicon cap remains. This mechanism could explain the difference in decrease of the silicon cap layer formed by SiH_4 or Si_3H_8.[86] A similar trend is observed when the anisotropic parameter B is plotted as function of number of Si monolayers. (not shown)

Because second-harmonic generation is not an absolute technique for measuring material thickness, a calibration to complementary measurement techniques would still be necessary for quantitative measurements. In addition, thickness measurements by SHG can only be performed for a well-known process where surface or interface properties are well known. Consequently, second-harmonic generation should be seen as a very accurate technique that require calibration for quantitative measurements.

It can be clearly observed from fig. 2.4 that the SHG intensity decreases, as expected, after the second oxidation step, indicating a decrease in Si thickness. This observation goes beyond the information that can be obtained by ellipsometry measurement alone, due to the standard deviation on the SE measurements. Hence, for silicon cap passivated germanium, the change in silicon thickness as a result of oxidation can be more accurately observed with second-harmonic generation as compared to ellipsometry. Note that the first sample (1.9ML) grown with silane does not follow the linear trend. This is because all of the silicon oxidized and no silicon interlayer is present in the structure.

2.5 Conclusion

In conclusion, we have shown that second-harmonic generation can be used to characterize buried interfaces with extremely high sensitivity. As a test case, we have found SHG to provide highly accurate relative measurements of the

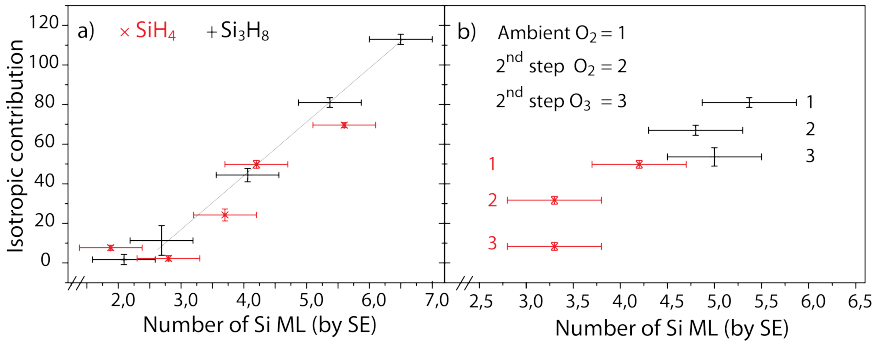

Figure 2.4: SHG sensitivity to oxidation steps. The isotropic (surface) contribution for the fitted curves in fig. 2.2 and fig. 2.3 are given as function of the number of silicon ML in a) and b) respectively. The number of monolayers is measured with ellipsometry. The data indicated with an x is recorded for SiH_4 as Si precursor, whereas the data indicated with a + is for Si_3H_8. For the different oxidized samples, the second oxidation step is specified. The line in a) is a guide to the eye.

thickness of silicon layers with only a few ML thickness on top of germanium substrates. Furthermore, these results show the subtle differences in oxidizing behavior of the Si layer during oxidizing cleaning steps as a function of the Si precursor used to grow the layer. In the absence of surface roughness or interface defects, we can conclude that SHG can distinguish different oxide treatments during semiconductor growth accurately, in contrast to spectroscopic ellipsometry. This emphasizes the usefulness of SHG as a solid probing technique for buried interfaces. However, thickness measurements by SHG can only be performed for a well-known process where surface or interface properties stay constant. To obtain an absolute measurement of the layer thickness, calibration is needed. In the future, second-harmonic generation can be extended for use in semiconductor growth monitoring and further research on new generations of semiconductor devices.

Acknowledgements

This work was supported by the Katholieke Universiteit Leuven (GOA). M.K.V. is grateful for the feedback on the figures and text and trial reading of M. Bloemen, W. Brullot and S. Vandendriessche. M.K.V. acknowledges the financial

support from imec and the opportunity for collaboration. V.K.V. is grateful for the financial support from the fund for scientific research Flanders (FWO-Vlaanderen).

	1.9ML	2.9ML	3.7ML	Sample 1 SiH_4: 4.2ML	5.6ML	2.1ML	2.7ML	4.1ML	Sample 1 Si_3H_8: 5.4ML	6.5ML	Sample 2 SiH_4	Sample 3 SiH_4	Sample 2 Si_3H_8	Sample 3 Si_3H_8
Preparation of wafers before ALD														
Boron implantation ($10^{16}cm^{-3}$)	x	x	x	x	x	x	x	x	x	x	x	x	x	x
Annealing step	x	x	x	x	x	x	x	x	x	x	x	x	x	x
silicon cap passivation														
10 minute H_2 bake at 650 °C + SiH_4 growth at 500 °C	x	x	x	x	x						x	x		
10 minute H_2 bake at 650 °C + Si_3H_8 grown at 350 °C						x	x	x	x	x			x	x
Oxidation step: 1 ppm ozone 60"											x	x	x	x
5 minute water rinse											x	x	x	x
HF-dip: 120" 0.5% HF + 5 minute water rinse											x	x	x	x
Oxidation step: 1 ppm ozone 60"	x	x	x	x	x	x	x	x	x	x		x		x
Marangoni dry	x	x	x	x	x	x	x	x	x	x	x	x	x	x
HfO_2 deposition														
HfO_2 ALD (8nm)	x	x	x	x	x	x	x	x	x	x	x	x	x	x

Table 2.1: Summary of the investigated samples

Chapter 3

Second harmonic generation indicates a better Si/Ge interface quality for higher temperature and with N_2 rather than with H_2 as the carrier gas

On similar structures as presented in chapter 2, the quality of the Ge/Si interface is evaluated. This interface is of great importance for device operation, since its location is close to the channel region of a MOS stack. Again, this research fits in the total research goal of providing valuable information of the interface properties in a MOS stack and how these interfaces are best optimized. In this chapter, the influence of carrier gas and temperature was studied. The interface quality was best when using N_2 rather than H_2 during the silicon-cap growth and at higher temperature. The capability of studying buried interfaces by second-harmonic generation is further exploited.

My contribution to this work were the second-harmonic generation measurements and its analysis. The samples were provided by dr. Benjamin Vincent from imec. Dr. Ventsislav Valev performed additional analysis and

submitted our work to IEEE Electron Device Letters, where it was accepted for publication.

V. K. Valev, **M. K. Vanbel**, B. Vincent, V. V. Moshchalkov, M. Caymax, T. Verbiest,
Second harmonic generation indicates a better Si/Ge interface quality for higher temperature and with N_2 rather than with H_2 as the carrier gas
IEEE Electron Device Letters, **32** (1), 12-14 (2011).

The research in this chapter can be connected to the work presented in chapter 2. It is important to note here that, although the structures are similar with respect to the sequence of layers, the processing temperature between the structures used in this chapter is different compared to previous chapter. Therefore, the structures under investigation in both chapters can be different when considering the Ge segregation in the Si layer or decomposition efficiency at the surface during the ALD process. Care has to be taken when correlating the results from both chapters.

One of the most important differences between the chapters appears due to the difference in Si cap thickness. The thickness of the silicon capping layer was verified using spectroscopic ellipsometry. Due to the complexity of the fitting model, the Si thickness is not very accurately defined. Therefore, correlating the thickness the data presented here to the data in previous chapter is not as straight forward. The fitting model used for the spectroscopic ellipsometry measurements for this chapter resulted in a doubling of the thickness compared to chapter 2. However, the values presented in this chapter present a more realistic measurement of the Si cap thickness due to the intrinsic thickness of one unit cell of SiO_2. The correlation between number of monolayers and the thickness in nm is still valid in both chapters, but the fitting model differed in both cases. Hence, besides considering the differences in structure, one has to take into account a difference in determined thickness of the Si capping layer on top of Ge.

When reading both chapters carefully, it seems that a different physical explanation is given for a similar process. However, this is not the case. In both cases, the SHG response is described as an electric dipole and electric quadrupole contribution. In this chapter, we do not elaborate on the physical meaning of these contributions, while in the previous chapter, different physical explanations are suggested to describe the observed trends in second-harmonic generation. When talking about interference between interfaces, we refer to the electric dipole contribution to the total SHG signal. However, the electric quadupole contribution can also change, since the amount of 'bulk' material in

the Si cap increases as well. Therefore, we preferred to explain the oxidation effect from previous chapter in a more rigorous manner than the surface quality experiments in this chapter.

In this chapter, we elaborate on the differences in SHG response of structures prepared with Si precursors in H_2 and N_2 as carrier gasses. We hypothesize that during Si cap growth, H_2 can interact with the surface of the wafer, while N_2 will not since it is an inert gas. Henceforth, the quality of the Ge/Si interface is determined by the rate of deposition of the Si cap. When a Si precursor reacts with the substrate's surface, the precursor and surface will form radicals or charges species such as dangling bonds. If these dangling bonds are not passivated again by H_2, the site is more reactive than if it were passivated with a hydrogen atom. Due to the sequence rate of the different processing steps, the first few monolayers are not fully covered, resulting in a poor interface quality. We believe that this could be the explanation for the difference in surface quality. However, this explanation is only suggested as possible mechanism for the difference in interface quality.

Abstract

In order for germanium (Ge) to replace silicon in advanced metal-oxide-semiconductor field-effect transistor (MOSFET) channels, proper passivation of Ge is required. For this purpose, an ultrathin epitaxial Si cap was grown on Ge(001), and we applied second-harmonic generation (SHG) in order to probe the Si/Ge interface quality. SHG indicates a better interface quality for a growth temperature of 500 °C rather than 450 °C. Similarly, a better quality of the interface is observed upon replacing the conventional H_2 carrier gas with N_2. Additionally, from the SHG signal, we were able to extract both the thickness of the native SiO_2 layer ($\sim$ 4 monolayers (ML)) and the thickness of the strained Si layer (relaxation at $\sim$ 12MLs). These results are important for building Ge-based electronic components.

3.1 Introduction

Nowadays, billions of MOSFETs are present on silicon (Si) microchips in electronic equipment and appliances. However, as device requirements are pushed forward, they encounter the fundamental limits of Si. Consequently, new materials with higher mobility than Si are being investigated for postsilicon technology. Germanium (Ge) is one of the best substitutes. Ge presents important advantages over Si: it exhibits two times higher electron mobility and four times higher hole mobility. Additionally, it can be grown on Si substrates having the same crystalline structures, which eases its integration into existing devices. Unfortunately, however, the high chemical reactivity of Ge makes formation of native germanium oxide (GeO_x) unavoidable. Whereas germanium seems a better choice for the semiconductor part of the MOSFET, GeO_x is much more unstable compared with SiO_2. An ultrathin Si cap layer has been suggested as an efficient way to passivate the Ge surface and, henceforth, prevent it from oxidizing.[39, 111, 112, 113] Within this method, the top few monolayers (MLs) of Si are partially oxidized to form an ultrathin SiO_2 layer, and subsequently, a high-k dielectric material can be deposited. Although this solution combines indeed the advantages of Ge and SiO_2/Si interlayers, its optimization requires the use of probing tools that are sensitive to the quality of buried interfaces. Optical second-harmonic generation (SHG) is well known for its surface/interface sensitivity down to the atomic layer, and in the past, it has been successfully used to characterize Si.[58, 114] Recently, we have applied SHG to the study of Si/Ge layers depending on Si precursor and temperature.[91] Here, we demonstrate that SHG can evaluate the quality of the buried Si/Ge interface as a function of temperature and carrier gas. These results are important for constructing Ge-based MOSFETs. Additionally, we

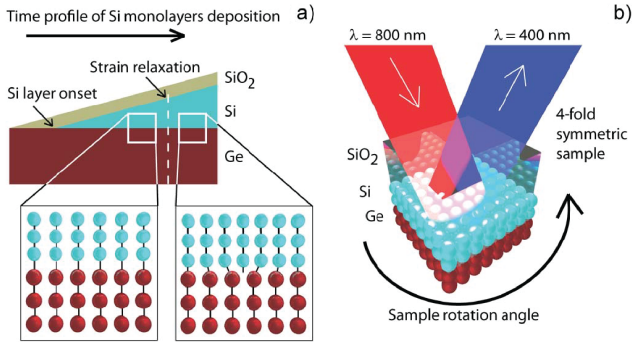

Figure 3.1: a) Silicon (Si) growth process. After exposure to the atmosphere, the top few MLs form a natural oxide (SiO_2). Because of the lattice mismatch, the first Si MLs on top of the Ge are strained. For thicker Si, the strain is released through formation of misfit dislocations. b) Schematic of the surface/interface-specific SHG experiments. Upon rotating the sample, SHG probes the fourfold symmetry of the (001)-oriented Si and Ge lattices.

demonstrate that SHG can define the inferior and superior limits for an efficient Si cap layer. These are the number of Si MLs that form SiO_2 and the number of Si MLs before creation of interface defects [see fig. 3.1a]. The significance of these observations is best understood upon following the sample growth.

3.2 Sample preparation and characterization

The first part of the sample growth process produces clean Ge (001) surfaces. To this end, 200mm Ge blanket wafers are obtained by first growing 1μm Ge on Si substrates followed by chemicomechanical polishing, which removes about 300nm germanium and yields smooth Ge surfaces (root mean square (RMS) = $0.2-0.4$μm and Zmax = 5μm determined by atomic force microscopy). In order to remove germanium native oxide prior to Si growth, the Ge surfaces receive a HF clean and an in situ bake at 650 °C, under H_2. Next, pure ultrathin Si caps are grown, i.e., with minimal Ge surface segregation into Si. The caps are deposited in an ASM-Epsilon RPCVD reactor. Trisilane (Si_3H_8) is used as the Si precursor because it allows Si growth at very low temperature (below 500 °C),[108] and strongly limits Ge surface segregation.[115] Si thickness is measured by spectroscopic ellipsometry immediately after growth and is

converted in MLs, whereby 1ML = 0.13nm. It should be noted that, upon exposure to the ambient, the top few Si MLs form a natural oxide [see fig. 3.1(a)]. As the thickness of the unoxidized Si layer increases, the 4.2% lattice mismatch with the underlying Ge causes an increase in stress within the first few Si MLs. For larger Si thickness, this strain is released through misfit dislocations, whereby Si dangling bonds appear at the interface. Upon completion of the growth process, the samples are ready to be measured with SHG. The SHG experiments are performed with a Ti:sapphire laser at an 800nm fundamental wavelength and with a standard setup. Because the sample surface has a fourfold symmetry, we can expect a fourfold symmetric expression in the equations describing the SHG signal as well.

3.3 Theoretical specifications

For a (001)-oriented lattice, in the S_{in}-P_{out} polarizer-analyzer configuration, we can calculate the SHG intensity by means of Sipe's theoretical model [23], i.e.,

$$I_{S_{\text{in}}-P_{\text{out}}}(2\omega) \propto |P^D_{iso} + P^Q_{iso} + P^Q_{anis} sin^2 2(\phi+\theta)|^2 \tag{3.1}$$

$$\propto |I_0(2\omega)| + 2|C| sin^2 2(\phi+\theta) + ... \tag{3.2}$$

where P^D_{iso}, P^Q_{iso} , and P^Q_{anis} are the nonlinear polarizations, which can be dipolar (superscript D), quadrupolar (superscript Q), isotropic (subscript iso), and anisotropic (subscript anis). Additionally, ϕ is the angle of sample rotation, and θ is the phase. Furthermore, $I_0(2\omega) = (P^D_{iso} + P^Q_{iso})^2$, whereas $C = 2(P^D_{iso} + P^Q_{iso})P^Q_{anis}$, and we neglected the term to the power of 4 because the isotropic contributions are much larger than the anisotropic one. Indeed, in our samples, the latter was evaluated alone, in the S_{in}-P_{out} polarizer-analyzer configuration, and for all samples, the signal was found to be less than 20 counts/s, P^Q_{anis} regroups all constant terms, ϕ is the angle of sample rotation, and θ is the phase.

3.4 Results

Equation (3.2) describes the SHG signal from an ideal surface or interface. However, large interdiffusion, roughness, defects, etc., could lower the quality of the interface. Therefore, fitting the experimental data to eq. (3.2) provides a

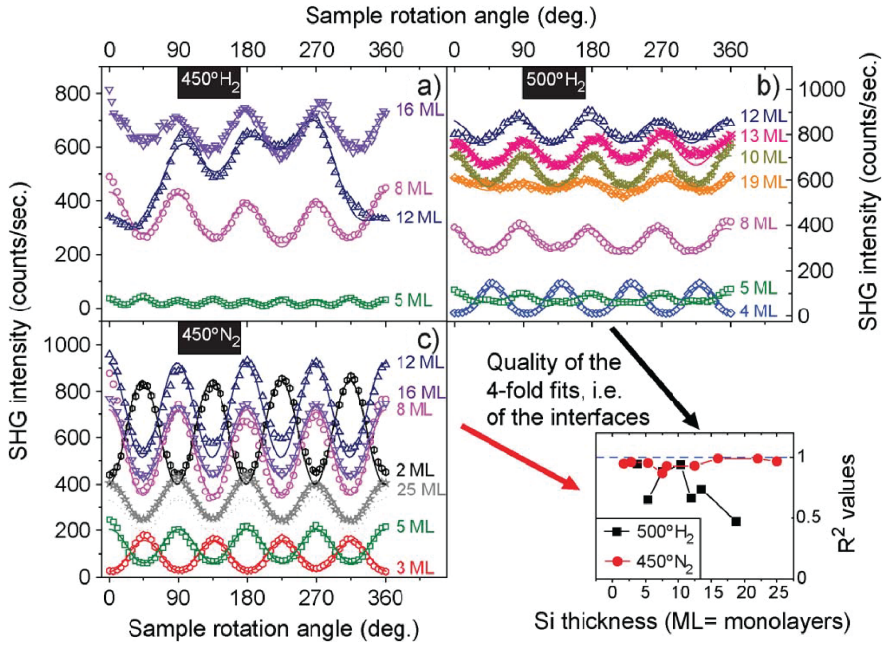

Figure 3.2: a) Upon deposition of the Si MLs at 450 °C with H_2 as the carrier gas, the interface-specific SHG yields an irregular response that indicates a poor quality of the Si/Ge interface. b) Rising the temperature or c) switching to N_2 as the carrier gas dramatically improves the quality of the interface. While fitting the SHG response to the fourfold symmetry of a (001)-oriented Si/Ge interface is impossible for a), the inset shows that, in c), the fits are better than in b); therefore, the interface quality is highest in c). All data were measured in the S_{in}-P_{out} polarizer-analyzer configuration.

measure of interface quality: High-quality interfaces will fit well, poorer ones will not.

For the purpose of optimizing the interface quality during the growth process, we studied the influence of temperature (450 °C versus 500 °C) and carrier gas (H_2 versus N_2). We believe that while temperature affects the dynamics of the growth mechanism, the carrier gas determines its nature. Indeed, the presence of H_2 insures good surface H passivation of Ge, and henceforth, during growth, Si atoms must take the place of H atoms. In a different manner, the presence of N_2 might result in poorer H surface passivation of Ge, and henceforth, during growth, Si atoms can bind to Ge at vacancy sites, i.e., without displacing H atoms.

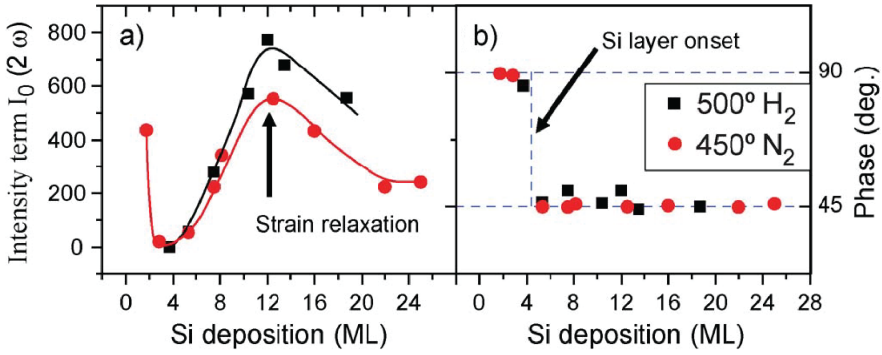

Figure 3.3: Fitting the interface-specific SHG curves in fig. 3.2 to a fourfold symmetrical response yields the a) intensity term $I_0(2\omega)$ and b) phase term θ. Plotting these parameters as a function of the number of deposited Si MLs clearly reveals the onset of Si layer growth and the strain relaxation.

In fig. 3.2(a), the SHG response as a function of sample rotation angle can be seen for samples that were grown at 450 °C with H_2 as the carrier gas. For 5MLs of Si, the material is mostly oxidized, and there is no real Si/Ge interface. For 8, 12, and 16MLs, fitting the graphs with eq. (3.2) alone is impossible. Both increasing the temperature [see fig. 3.2b] and changing the carrier gas [see fig. 3.2(c)] dramatically improve the interface quality. Indeed, all the graphs in these figures can be fitted with eq. (3.2), and as shown in fig. 3.2 (inset), the best fits are obtained upon switching to N_2 as the carrier gas. Furthermore, the fitting parameters themselves contain interface-specific information.

In fig. 3.3, the intensity term $I_0(2\omega)$ from eq. (3.2) is plotted as a function of the deposited Si thickness, for both the growing conditions at 500 °C with H_2 and at 450 °C with N_2. Both curves indicate clear extrema that are associated with the interface events of Si layer onset and strain relaxation [see also fig. 3.1a]. More specifically, from the point of view of an interface-specific technique such as SHG, the appearance of new interfaces within the sample is a dramatic event. A large change in the signal is therefore expected for a Si thickness of 4-5MLs, since this is the depth of SiO_2, as measured by ellipsometry after native oxide formation (see also [91]) Moreover, the signal from the Si/Ge interface is opposite in phase to the signal from the SiO_2/Si interface because these interfaces have opposite orientations (directions of the surface normal) with respect to Si. Additionally, for the purpose of comparing the SHG signal before the Si layer onset and afterward, we consider that the oxide/semiconductor interfaces SiO_2/Si and SiO_2/Ge are similarly oriented. Therefore, when the

signals from both SiO_2/Si and Si/Ge interfaces cancel, the total SHG amplitude is zero. However, how thick should the Si be for this cancellation? We can find the answer in fig. 3.3b, where the total SHG phase θ in eq. (3.2) is plotted as a function of the thickness of deposited Si. It can be seen that, within a thickness of 2MLs, the phase reverses completely, which indicates that 2MLs of Si are all that is needed for the amplitude $I_0(2\omega)$ to cancel. Both the amplitude minimum and the phase change are therefore clear indicators for the onset of the Si layer. Subsequently, as the thickness of the Si layer increases, the two Si interfaces move away from complete cancellation, and henceforth, the SHG signal increases until the maximum of $I_0(2\omega)$ is reached. With increasing Si thickness, the contribution from the lower interface should eventually decrease due to absorption in Si for both the fundamental and the second-harmonic. However, the absorption in Si is negligible for a thickness of 7-8MLs. On the other hand, strain relaxation in Si, together with formation of misfit dislocations at the Si/Ge interface, is expected to occur in the range from 0.8 to 1.5nm.[112, 39, 40] This indicates that the maximum of $I_0(2\omega)$ at 12MLs ($\sim$ 1.5nm) is indeed related to strain relaxation.

3.5 Conclusion

In conclusion, we have demonstrated that SHG is a valuable tool to evaluate the quality of the Si/Ge interfaces, which is particularly useful for optimizing ultrathin Si cap growth on Ge. In our case, the influence of carrier gas and temperature was studied, but other growth parameters with an impact on the interface can be investigated as well (i.e., nature of the Si precursor, crystalline orientation, preparation of the Ge surface, and film contamination, etc.). In the past, SHG has been widely applied in the study of Si surfaces. Surfaces, however, can readily be investigated at the atomic scale with surface probe microscopes. Therefore, our work shows that SHG is even better suited for the study of buried semiconductor interfaces for next-generation devices.

Acknowledgments

This work was supported in part by the Fund for Scientific Research-Flanders (FWO-Vlaanderen), by the University of Leuven through the Concerted Research Action (GOA) Program, by Methusalem Funding by the Flemish government, and by the Belgian Interuniversity Attraction Poles Programmes. The work of V. K. Valev was supported by FWO-Vlaanderen.

Chapter 4

Second-harmonic generation as characterization tool for Ge/high-k dielectric interfaces

In this chapter, we elaborate further on the advantages of second-harmonic generation as characterization tool for surface and buried interfaces. In chapter 2 and chapter 3, we elaborated on the use of a Si capping layer on Ge to overcome some of the passivation problems of Ge itself. In this case, the thermal oxide of Si was used instead of Ge. However, there are different methods for Ge passivation. In this chapter, the Ge surface itself was passivated by means of a sulphur monolayer, prior to growing a high-k dielectric with ALD. We elaborate on the interface properties of sulphur passivated Ge surface. Sulphur was introduced at the semiconductor/oxide interface to further improve the surface properties. We show that the second-harmonic signal from a MOS structure is not defined by the oxide layer, but is primarily determined by the semiconducting layer and the interface between the oxide and semiconducting layer. The isotropic SHG response from samples with different oxide thickness yield the same trend. Furthermore, it is hypothesized that the oxidizing agent determines the final structure of a MOS transistor. In order to clearly assign the difference in SHG response of the structures after a different number of ALD steps, a clear view on the elemental composition near the interface is necessary.

The sulphur passivated Si wafers were provided by dr. Annelies Delabie and dr. Sonja Sioncke from imec. I performed the SHG measurements and analysis of the data. I submitted our findings to a proceedings of SPIE, were our manuscript was accepted. I presented our conclusions on SPIE Europe 2012 in Brussels.

M. K. Vanbel, A. Delabie, S. Sioncke, C. Adelmann, V. V. Afanas'ev, J.-P. Locquet, S. Van Elshocht, M. Caymax, T. Verbiest,
Second-harmonic generation as characterization tool for Ge/high-k dielectric interfaces
Proceedings to SPIE, **8434**, 2012, 84341F.

Abstract

Because the germanium native oxide constitutes a poor dielectric, building metal-oxide-semiconductor field-effect transistor (MOSFET) gate stacks on Ge requires passivation of the interface between the dielectric and the Ge channel. Different approaches to perform this passivation are available: GeO_2 growth prior to high-k depositing, sulphur passivation, etc. The interface properties of these MOSFET stacks are important, because they determine the electrical properties of the whole structure. Dangling bonds introduce extra energy levels within the band gap, which results in a loss of efficiency in switching a MOS - field effect transistor on and off. Fixed charges near the interface enlarge the voltage needed for switching between on and off state as well. Hence, characterizing these interfaces is a key challenge in semiconductor fabrication. This can for example be achieved using second-harmonic generation (SHG) to probe the interface, because SHG is an inherent surface and interface sensitive technique. In this work, we present SHG as an promising surface and interface characterization tool passivated germanium samples. Different SHG responses are shown for germanium samples with a sulphur passivated Ge or high-k dielectric on top of Si. We show that the oxide layer as such is not probed by SHG and that different bonds over the Ge/oxide interface result in a difference SHG response.

4.1 Introduction

Since the dawn of semiconductor devices, there has been a driving force to shrink the dimensions of transistors. This enabled a drastic increase in the number of transistors that can be implemented in an integrated circuit (IC), which enhanced drastically the usefulness of a transistor. This trend is described as Moore's law: every 2 years, the number of transistors approximately doubles.[87, 89, 116] In other words, the performance of an IC doubles every two years. This law is nowadays used as a guideline for technological challenges in semiconductor industry. In addition to Moore's law, an ITRS (international technology roadmap for semiconductors) roadmap,[43] is developed to specify the research topics in transistor optimization. This ensures that all participants who are working on the improvement of semiconductor devices, are striving for the same goals.

To increase the number of transistors on one IC, the dimensions of each individual transistor should decrease. Hence, one of the proposed research topics aims at reducing the channel length. The channel length is the distance between the source and the drain, as it is shown in fig. 4.1a. This is the area of

the transistor which can be electrically screened to provide current through the device or to prevent a current from flowing through the device. The transistor performance heavily relies on the condition of the interfaces in the gate stack close to the channel. Therefore, it is of great importance to understand how the different manufacturing steps influence the interfaces in semiconductor devices and how these process steps influence the electrical passivation of a device. To keep up with the performance enhancement, alternative channel materials were investigated to replace Si in standard metal-oxide-semiconductor (MOS) devices.[117] The use of high mobility material in the channel enhances the "on" current of a semiconductor device. For pMOS, Ge seems to be an ideal candidate.[118] However, the implementation of Ge in semiconductor devices cannot be taken for granted. Passivation of Ge has been shown to be a serious issue.[85] As opposed to Si, Ge does not form a thermally stable native oxide (GeO_2). Moreover, the Ge-O bonds (bond-dissociation energy of 157 ± 5kcal/mol) are weaker than Si-O bonds (bond-dissociation energy of 185 ± 7kcal/mol),[119] resulting in a weaker Ge-O network in the native oxide layer compared to SiO_2. Most of all, hydrogen passivation to optimize the interface has little influence on the electrical or crystallographic properties of a Ge interface.[120] Hence, additional processing steps have to be undertaken to deposit a dielectric or gate oxide layer.

Another research topic which is specified in the ITRS roadmap is the reduction of the gate oxide thickness or equivalent oxide thickness (EOT). The reduction in oxide thickness increases the oxide capacitance, which increases the "on" current of the device. Consequently, narrowing the oxide thickness has a positive influence on the device performance. However, upon decreasing the oxide thickness, leakage currents, due to a tunneling current, drastically increase. For a silicon oxide gate dielectric, tunneling current appears when the SiO_2 layer is reduced to approximately 2nm. When implementing an oxide layer with higher dielectric constant than SiO_2, the same capacitance can be retained for a thicker oxide layer, which also reduces the leakage currents. Both HfO_2 and Al_2O_3 are thus being considered as replacement for SiO_2.[121] Another major research topic is sulfur passivation of Germanium.[41] The implementation of both an alternative channel material and an alternative oxide layer brings additional challenges to semiconductor research as well as to characterization techniques.[90] Any electrical defects at the interface screen the channel below and induce a delay in switching the semiconductor device on or off. Hence, improvement in understanding or production of the passivation layer is of great importance. More specifically, proper passivation, segregation, defects which induce energy levels within the band gap and reduce the efficiency of the semiconductor and fixed charges at the insulator/semiconductor interface are amongst the largest difficulties in semiconductor processing.

To overcome these difficulties, surface and interface specific characterization techniques are employed in semiconductor research to optimize transistors. A technique such as second-harmonic generation (SHG) is highly suited for investigation of interfaces in semiconductors. SHG is forbidden in centrosymmetric media within the dipole approximation. Centrosymmetry is broken at surfaces and interfaces in elemental semiconductors, resulting in a high interest for implementation of SHG in semiconductor research. In literature, it has been reported that SHG is a valid tool for studying interfaces in semiconductors.[122] Most of the research has been done on Si. Rotational anisotropy SHG on Si provides insight in surface and interface properties, such as strain,[49, 50] roughness,[51, 52] and surface reconstruction.[14] When including electric field-induced second-harmonic generation (EFISH), the electric field near the interface from externally applied voltage,[58] or doping can be characterized.[60]

In this publication, we combine the novel approaches in semiconductor research with the high sensitivity of second-harmonic generation. We have investigated MOS structures with different oxide thickness. A Si wafer was passivated with an Al_2O_3 oxide layer and those structures give all the same magnitude of isotropic SHG response, meaning that the oxide layer is not probed in an SHG measurement. Furthermore, we investigated sulfur passivated Ge substrates with a Al_2O_3 gate oxide layer grown in different oxidation conditions, namely water and ozone. We show that SHG distinguishes a pure sulfur passivated Ge wafer from a sulfoxide passivated Ge wafer, which results from the different oxidizing agents during the ALD process.

4.2 General concepts

The operation of a transistor is key in understanding the goals which are specified in the ITRS roadmap. As can be seen from fig. 4.1a, a transistor consists of a source, drain and gate area, where the channel is located directly under the gate oxide. The sequence of the layers in a transistor is responsible for its name: metal-oxide-semiconductor field-effect transistor (MOSFET). In silicon or germanium-based transistors, the source and drain consist of negative or positive doped material. The body is oppositely doped compared to the source and drain. The oxide layer prevents the creation of a short circuit in the device. For use in transistor devices, the oxide layer should not contain any charges, which ensures a rapid screening of the channel and no power loss when turning a device “on” or “off”.

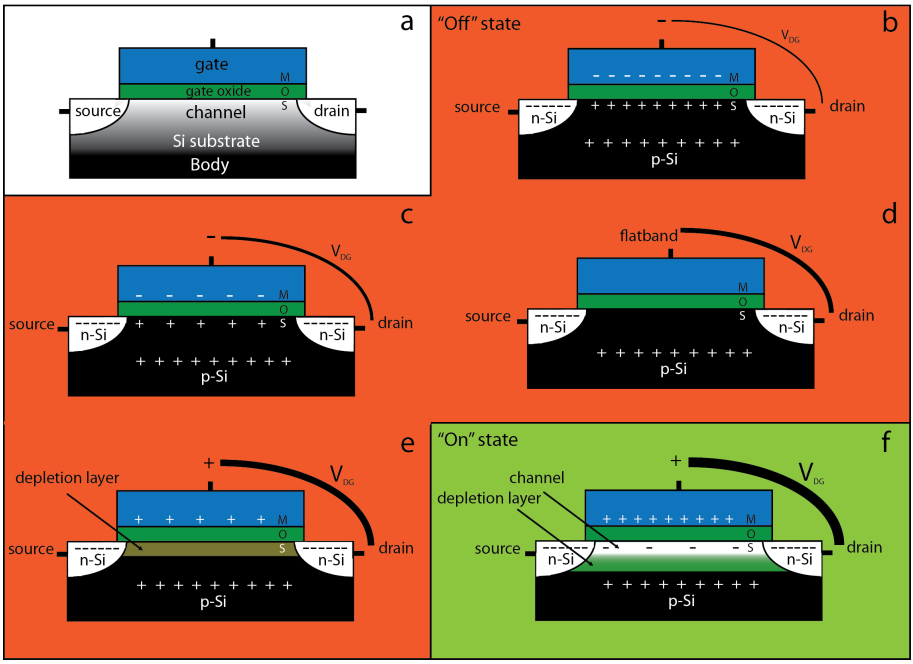

Figure 4.1: Representation of the working principle of a pMOS transistor. The different areas in a semiconductor device are shown in a. From b to f, the state of the MOS device is shown for increasing voltage from the gate to the drain. From b to e, the device is in the "off" state, while the "on" state is depicted in f.

By supplying a voltage from the gate to the drain, a conduction channel can be formed, depending on the sign and magnitude of the voltage. The doping level of a semiconductor device is always specified because it determines the operation of the device. The doping can be positive in the source and drain area (p-type transistor) or negative (n-type transistor). In the case of a n-doped channel (electrons flow through the channel), the source and drain are n-doped and the body is p-doped, see fig. 4.1b. When the device is turned "on", a current can flow from the source to the drain through the channel. When the device is turned "off", there is no conducting path between the source and the drain of the transistor. More specifically, when applying a negative voltage over the gate and drain, positive ions will be attracted to the gate/body interface, preventing a "negative" current from flowing from source to drain. The accumulation of the positive charges near the interface is called the accumulation layer (shown in fig. 4.1b), because the majority carriers of the body are accumulated there. However, when the voltage on the gate is increased, less holes (positive charges)

are attracted to the interface between the body and the passivation layer, which reduces the thickness of the accumulation layer (Shown in fig. 4.1c). At a certain voltage, which is called the flatband voltage, no net charges are present at the body/oxide interface. In this situation, the accumulation layer has completely disappeared, which is demonstrated in fig. 4.1d. When increasing the voltage even further, positive charges are inserted from the gate towards the oxide layer. Due to the electrostatic repulsion, the holes are pushed away from the oxide/body interface, which results in a depletion layer, where no more deficit of electrons is present (fig. 4.1e). No negative charges are present due to the presence of majority carriers in the area, i.e. holes. If the voltage is increased again, majority charges are even further removed from the interface and a so-called inversion layer of channel is formed. In the channel, minority carriers are present and enable a current flow between the source and the drain (fig. 4.1f). At this moment, the device is turned "on". Hence, changes in supply voltage, modulate the current through the transistor. As can be noticed, the interfaces where charges can accumulate are of greatest importance in a semiconductor device. The main goal is to understand and optimize these interfaces.

4.3 Methodology

The rotational anisotropy second-harmonic generation experiment was carried out using a Ti-Al_2O_3 laser at the fixed fundamental wavelength of 800nm with an average power output of 70mW. The pulse length and repetition rate are respectively 120fs and 82MHz. The polarization of the incident beam on the sample is controlled by a polarizer and half-wave plate. This configuration allows us to adjust the polarization of the incident beam. In the experiment, the input polarization can be p-polarized or s-polarized, meaning that the electric field of the linearly polarized laser beam is parallel or perpendicular to the plane of incidence, respectively. The incident beam was cleared of the SHG originating in the laser cavity by a RG665 filter and then focused on the sample to a spot of approximately 40μm. The angle of optical incidence is 45 ° on the sample, which can be rotated around its surface normal. The generated photons of the half wavelength (400nm) are then filtered trough two BG39 filters, which blocks the fundamental beam. An analyzer is placed after the sample, to vary the output second-harmonic beam. This output beam is detected with a photo multiplier tube and analyzed with a photon counter.

Within the electric dipole approximation, SHG is forbidden in centrosymmetric media,[99] that is to say, it is only allowed in the case of broken symmetry. Symmetry in the material can be broken by externally applying electric,[27] or magnetic dc fields,[123] though care should be taken while estimating the

dependence of the SHG signal on the latter.[124] Moreover, the technique is also capable of imaging ferroelectric,[125] and ferromagnetic,[126] domains within the material. Additionally, chiral geometry,[127] as well as the surface and interfaces in a multilayered system constitute symmetry breaking and all can give rise to dipolar SHG signal. In the latter case, the technique exhibits spectacular sensitivity, down to the atomic monolayer.[94] For this reason, surface/interface specific properties, such as plasmon field enhancementsn[128, 129] or charge accumulation can be readily investigated by SHG. However, not all SHG signal is of dipolar origin and additional, higher multipoles should be taken into account.[10] Hence, for intense incident electromagnetic fields, the polarization of the medium can be described by

$$\mathbf{P}(2\omega) = \mathbf{P^D}(2\omega) + \mathbf{P^Q}(2\omega) = \chi^D : \mathbf{E}(\omega)\mathbf{E}(\omega) + \chi^Q \vdots \mathbf{E}(\omega)\nabla\mathbf{E}(\omega) \qquad (4.1)$$

where ω the frequency of the light, $E(\omega)$ the electric fields vectors of the incident light and χ^D and χ^Q indicate the dipolar and the quadrupolar nonlinear susceptibilities, respectively. The dipolar nonlinear susceptibility χ^D is a third rank tensor with 27 components. However, the number of contributing components is reduced by symmetry considerations of the sample.[23] Additionally, by changing the polarizer-analyzer configuration, different tensor components can be addressed. For a (001) oriented substrate, e.g. Si(001) and Ge(001) which are used in the investigated samples, the S_{in}-P_{out} polarizer-analyzer configuration, in χ^D a single tensor element is addressed, namely χ_{zyy} : the electric dipolar contribution is therefore a constant.
Despite the centrosymmetry, the bulk of the sample will contribute to the total signal as well through electric-quadrupole or magnetic dipole interactions. This nonlocal response, which corresponds to the last term in eq. (A.15), can be described by a quadrupolar polarization of the form,[26]

$$P_i^{(2\omega)}(r) = (\delta - \beta - 2\gamma)(\mathbf{E}\cdot\nabla)E_i + \beta E_i(\nabla\cdot\mathbf{E}) + \gamma\nabla_i(\mathbf{E}\cdot\mathbf{E}) + \zeta\sum_i \hat{e}_i E_i \nabla_i E_i \quad (4.2)$$

where β, δ, γ and ζ are phenomenological constants. We omitted the frequency dependence symbol ω of the fundamental fields for clarity reasons.
In a typical SHG experiment, the sample is rotated around its surface normal and the second-harmonic intensity is recorded for a certain input-output polarization. For the S_{in}-P_{out} polarizer-analyzer configuration, the azimuthal rotation can be phenomenologically described by:[130, 131]

$$I_{S_{\mathrm{in}}-P_{\mathrm{out}}}(2\omega) \propto |I_0(2\omega)| + 2|B|sin^2 2(\phi+\theta) + |A|sin^4 2(\phi+\theta) \qquad (4.3)$$

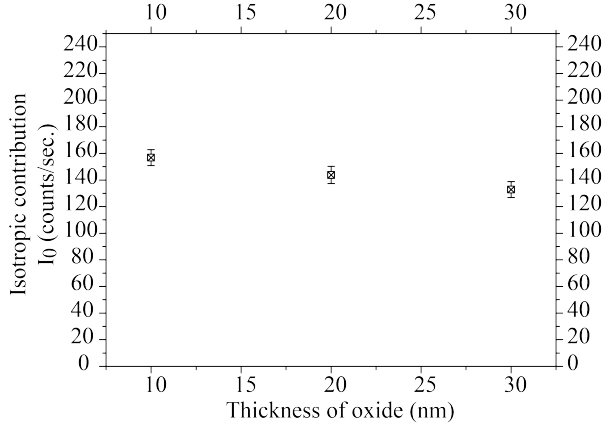

Figure 4.2: The isotropic contribution of an Al_2O_3 layer on top of partially oxidized Si as function of oxide thickness.

where $I_0(2\omega)$ is a combination of all isotropic terms squared from the dipolar and quadrupolar susceptibility, while A is the squared anisotropic contribution from the quadrupolar susceptibility. B is the product of the isotropic and anisotropic terms. In our results, the A term was measured in S_{in}-P_{out} and was found to be very small, consequently it was neglected in the fitting of the data. ϕ is the azimuthal rotation of the sample and θ is a phase factor. We set $\phi = 0$ along the [110] direction of the crystal.

4.4 Results and discussions

Can the thickness of the oxide itself influence the SHG response? It is known that, upon growing an oxide layer, after a certain thickness of oxide layer is achieved, the morphology of the lower interface does not change. In this study, we investigated the SHG response of thick oxide layers. In fig. 4.2, the isotropic contribution of the total SHG signal is plotted as function of the oxide thickness of Al_2O_3 oxide layer on top of SiO_2 passivated Si wafers. On the silicon wafers, a chemical Si oxide of 1.1nm was grown on top of the wafer. Thereafter, aluminiumoxide was deposited in an ALD reactor using the $Al(CH_3)_3/H_2O$ process, resulting in the final structure of Al_2O_3 on top of a Si wafers with a SiO_2 surface. Different thickness of Al_2O_3 was deposited, ranging from 10 to 30nm. From fig. 4.2, it can be seen that the isotropic contribution does not

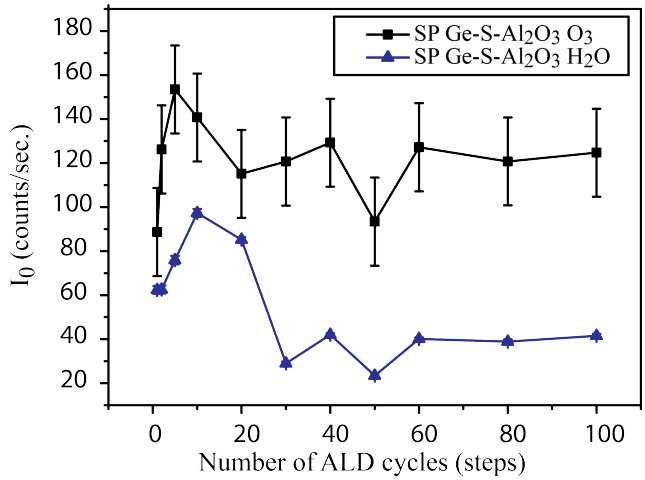

Figure 4.3: The isotropic contribution of Ge-S-Al_2O_3 structures grown with ozone (squared) or water (triangles) is shown as function of the number of ALD steps.

change when varying the oxide thickness. Hence, the oxide is not probed as such by SHG.

In fig. 4.3, the SHG response in the S_{in}-P_{out} polarizer-analyzer configuration of sulphur passivated Ge samples is shown. The samples at study consist of a p-type germanium wafer which was Ga doped with a resistivity of 0.04 to 0.4Ωm. These wafers were cleaned in an HF solution, removing most of the oxide on top of the Ge. Thereafter, the samples were annealed at 650 °C in hydrogen gas atmosphere for 10minutes. Subsequently, the Ge substrate was exposed to H_2S at 20Torr, enabling the formation of 1 atomic layer of sulphur passivation layer. Finally, Al_2O_3 was deposited using the ALD growth mechanism of $Al(CH_3)_3/H_2O$ or $Al(CH_3)_3/O_3$.[121] The different behaviour of these two structures, with different oxide thickness, are investigated with SHG. The SHG response from bulk Si and bulk Ge is similar, due to the same symmetry consideration of the bulk materials, which enables comparison with the previous Si substrates. It can be observed that the trend is similar for both materials. The SHG responses of both materials initially increases and thereafter the response decreases and stays approximately constant. However, the magnitude of I_0, the isotropic contribution in the SHG signal is different for different oxidizing agents during the ALD process, namely ozone treatment or water treatment. Sioncke *et al.*[41] revealed that the structures grown with

water or ozone as oxidizing agents in the ALD process differ in both electrical properties and morphology at and near the interface. We believe that the difference in the isotropic contribution of both sample series is arising from the difference in nature of the morphology of the interface. When performing the ALD process with water as oxidizing agent, the interface which is formed is a pure S-passivated Ge interface from which the Al_2O_3 is starting to grow in a rather uniform manner.[132] However, when using ozone as the oxidizing agent, both Ge-S-Al_2O_3 and Ge-O-Al_2O_3 bonds at the interface are present. Even the presence of Ge-O-S-O-Al_2O_3 or Ge-S-O-Al_2O_3 bonds cannot be excluded. This difference in material can be correlated with the difference in SHG response. A difference in material yields a different susceptibility tensor, resulting in a different isotropic behaviour. It can be seen that for larger numbers of ALD steps (or thicker oxide layers) the isotropic SHG response is approximately constant, which is consistent with the case of Al_2O_3 passivated Si. The precise physical mechanism behind this trend will be the subject of future research.

4.5 Conclusion

In this study, we provide evidence that the oxide layer of a MOS transistor is not probed in a rotational anisotropy SHG measurement. We report the same trend in isotropic SHG response from samples with different oxide thickness. Furthermore, it can be stated that the oxidizing agent determines the final structure of a MOS transistor. The difference in structure of the interface, arising from different oxidizing agents can be detected by SHG. The use of water as oxidant in the ALD process, results in a lower SHG response of the interface, compared to the sample which was prepared with ozone as the oxidizing agent. At this stage of out investigations, this can be attributed to the difference in bonds, which are present at the interface: the semiconductor is passivated with a pure sulphur interface when water is used as oxidizing agent, while Ge-S-Al_2O_3, Ge-O-Al_2O_3, Ge-S-O-Al_2O_3 and Ge-O-S-O-Al_2O_3bonds appear when ozone is the oxidant.

Acknowledgments

This work was supported by the Katholieke Universiteit Leuven (GOA). M.K.V. acknowledges the financial support from imec and the opportunity for collaboration. M.K.V. is very grateful for the support and scientific discussions with Ventsislav K. Valev. M.K.V. is thankful for the library services of Kevin Bogaerts.

Chapter 5

Tunneling of holes is observed by second-harmonic generation

As presented previously in chapters 1 and 4, a metal-oxide-semiconductor field-effect transistor (MOSFET) can only operate when a potential is applied over the gate and drain. Therefore, an external electric field is applied to investigate the electrical properties of an metal-oxide-semiconductor (MOS) stack. The electrical response of n-doped Si with an Al_2O_3 layer on top is evaluated by electric field-induced second-harmonic generation (EFISH), when an external electric field is applied. This electric field is applied by placing a potential over a corona wire and the sample substrate. In this manner, no second-harmonic generation (SHG) contribution of a metal electrode layer has to be accounted for. By changing the charge density in the space-charge region of silicon, the second-harmonic response of the structure can be altered. Furthermore, tunneling of holes under the influence of a negative corona field is observed with second-harmonic generation, which is confirmed by capacitance-voltage measurements.

The Al_2O_3 covered Si samples were provided by dr. Christoph Adelmann of imec. Prof. dr. Valeri Afanas'ev provided insight about the physical mechanism or the charge migration in these type of structures. I performed the SHG measurements and data analysis. Thereafter, I submitted our work to Applied Physics Letters, where it was accepted for publication.

M. K. Vanbel,V. V. Afanas'ev, C. Adelmann, M. Caymax, V. K. Valev, T. Verbiest,
Tunneling of holes is observed by second-harmonic generation
Applied Physics Letters, **102** (8), 082104 (2013).

Abstract

Al_2O_3 passivated n-doped Si substrates are investigated by second-harmonic generation (SHG) upon applying an external electric field by a corona wire. The observed change in the SHG response upon applying an external electric field, is attributed to charge transfer in the semiconductor. Capacitance-voltage (CV) measurements are performed to affirm this conclusion. Upon applying a large negative electric field over the structure, a clear alteration in SHG signal is observed, which corresponds to tunneling of holes from the n-doped silicon into the aluminum oxide layer.

5.1 Introduction

The optimization of the channel in a metal-oxide-semiconductor (MOS) is one of the key issues in the semiconductor industry. The function of an MOS device is to alter the current through the channel (or space-charge region in the semiconductor), which results in an on-current or off-current. In an actual device, the switching between on and off is achieved by changing the voltage on the metal gate. Besides electrical techniques, this switching between on and off can be investigated by second-harmonic generation (SHG) and electric field-induced second-harmonic generation (EFISH), with the advantage that it does not necessarily require the fabrication of electrodes on the structure. Moreover, SHG gives information on both the electrical properties and interface properties. Investigation of the space-charge region (SCR) of silicon and the interface properties of semiconductors with metal gate by means of EFISH has been evaluated successfully by many authors, such as Aktsipetrov *et al.*,[30, 32] Chang *et al.*,[64] Glinka *et al.*,[133] and Scheidt *et al.*[102, 134] Moreover, SHG has been used to characterize the interface of MOS structures.[16, 49] Although MOS structures form the basis of the current transistor devices, quantum well devices are promising to keep scaling the devices according to the scaling laws.[135, 136] In these devices, the tunneling current is of critical importance for device operation. Since the tunneled charges are confined in the structure, the SHG response can give valuable insights into quantum well devices.

However, in the previously mentioned investigations,[32, 64] the SHG contributions from the metal layer could not be separated from those of the charges at the interface.

In order to clearly investigate the role of the SHG signal from the relevant semiconductor interface, we chose a different approach to charge the structure, namely by positioning a charged corona wire above the aluminum oxide passivated semiconductor. In this manner, no additional metal layer is present,

which in turn, cannot contribute to the total SHG signal and facilitates the analysis.

In this letter, we report the SHG response upon changing the electric corona field from zero to positive or negative and vice versa. Applying a positive corona field, decreases the initial electric field in the space-charge region of Si, decreasing the SHG signal. Upon applying a large negative electric field over the structure, a clear increase and subsequent decrease in SHG signal is observed, where the latter corresponds to tunneling of holes through the SiO_x layer. The second-harmonic signals are verified by capacitance-voltage measurements on the same structures, to justify the physical model that is proposed here. The change in SHG intensity is correlated to the exponential tunneling decay and the decrease of electric field in the silicon space-charge region (SCR) due to dissipation of the corona charges at the surface.

5.2 Materials and methods

The Si-SiO_2-Al_2O_3 structures were prepared on 300mm n-type Si (100) wafers. Initially, a $\sim$ 200nm thick As-doped epitaxial Si layer was deposited by chemical vapor deposition in an ASM Epsilon reactor. The doping level was 10^{16}cm^{-3}. Subsequently, a $\sim$ 1nm thick chemical SiO_2 was grown on the surface in ozonated H_2O. Different thickness of Al_2O_3 was then deposited by atomic layer deposition in an ASM Pulsar reactor from trimethyl aluminum and H_2O at 300 °C.

The time-dependent second-harmonic generation (TD-SHG) experiments were carried out using a Ti-Al_2O_3 laser at the fixed fundamental wavelength of 800nm with an average power output of 70mW. The pulse length and repetition rate are respectively 120fs and 82MHz. For our measurements, the polarizer-analyzer combination of P_{in}-P_{out} was used.[137]

The charging of the passivated semiconducting samples is achieved by corona poling, as is schematically presented in fig. 5.1. The corona wire was placed at 3cm from the sample. A voltage of -3kV and 2.7kV was used to charge the surface, which did not lead to oxide breakthrough. Upon charging, the voltage was quickly ramped from 0V to the maximal value. The current from the corona wire to the substrate was monitored and remained constant during the measurements.

In centrosymmetric materials like Si, SHG is forbidden within the electric dipole approximation. However, the total SHG response of uncharged structures can be written in terms of electric dipole contributions $\overrightarrow{P}^D(2\omega)$ and electric quadrupole contributions $\overrightarrow{P}^Q(2\omega)$ by

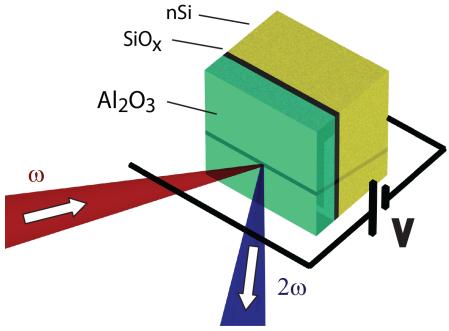

Figure 5.1: Schematic representation of the TD-SHG experiment on aluminum oxide passivated silicon with a corona wire. An external electric field can be applied between the surface of the metal-oxide-semiconductor structure and the corona wire. Due to this electric field, an internal field in the space-charge region in silicon is induced.

$$\begin{aligned}\overrightarrow{P}^{\text{eff}}(2\omega) &= \overrightarrow{P}^{D}(2\omega) + \overrightarrow{P}^{Q}(2\omega) \\ &= \chi^{D} : \overrightarrow{E}(\omega)\overrightarrow{E}(\omega) + \chi^{Q} \vdots \overrightarrow{E}(\omega)\nabla\overrightarrow{E}(\omega)\end{aligned} \tag{5.1}$$

where χ^{D} and χ^{Q} indicate the dipolar and the quadrupole nonlinear susceptibilities. A separation of the dipolar and quadrupole contributions is usually not possible in an experiment with a single fundamental beam in a polarizer-analyzer combination of P_{in}-P_{out}. Hence, the nonlinear polarization attributed to Si, will be treated as an effective polarization.

Furthermore, upon applying an electric field, an electric field-induced second-harmonic generation (EFISH) term can be written as

$$\overrightarrow{P}^{\text{dc-induced}}(2\omega) = \chi^{(3)} \vdots \overrightarrow{E}(\omega)\overrightarrow{E}(\omega)\overrightarrow{E}_{dc} \tag{5.2}$$

where $\overrightarrow{E}_{dc}$ is the internal electric field, arising from the external applied electric field and $\chi^{(3)}$ is a fourth rank tensor. Since $\overrightarrow{E}_{dc}$ is oriented in the z direction

only, eq. (5.2) can be written as

$$\overrightarrow{P}_{\text{eff}}^{\text{dc-induced}}(2\omega) = \chi_{\text{eff}}^{(3)} \vdots \overrightarrow{E}(\omega)\overrightarrow{E}(\omega)\overrightarrow{E}_{z,dc} \tag{5.3}$$

where $\overrightarrow{E}_{z,dc}$ is only oriented in the z-direction, perpendicular to the surface and $\overrightarrow{P}_{\text{eff}}$ denotes that the measurements are performed in equilibrium.[32]

From eq. (A.16) and eq. (5.3), the total SHG polarization and SHG intensity in reflection can be described as,[4, 32, 138]

$$\begin{aligned} \overrightarrow{P}_{\text{total}} &= \chi^{D} : \overrightarrow{E}(\omega)\overrightarrow{E}(\omega) + \chi^{Q} \vdots \overrightarrow{E}(\omega)\nabla\overrightarrow{E}(\omega) \\ &\quad + \chi^{(3)} \vdots \overrightarrow{E}(\omega)\overrightarrow{E}(\omega)\overrightarrow{E}_{z,dc} \\ I_{(2\omega)} &\sim (\overrightarrow{P}_{\text{total}})^2 \end{aligned} \tag{5.4}$$

where χ^{D} reflects the centrosymmetry of the structure and the symmetry of surface or interface, χ^{Q} reflects the crystal lattice and the gradient of the light within the penetration depth and $\chi^{(3)}$ corresponds to EFISH. Only $\chi^{(3)}$ is affected by the applied electric field, while χ^{D} and χ^{Q} stay invariant. The major contribution in $\chi^{(3)}$ arises mostly from the χ_{zzzz} and $\chi_{zxxz} = \chi_{zyyz}$, since the direction of the electric field in the SCR of silicon is in the z-direction.

Upon applying a corona field, only the $\overrightarrow{E}_{z,dc}$ term will be affected. Since the number of charges particles $Q(t)$ can be written as,

$$Q(t) = q \cdot N_t(1 - exp(\frac{-t \cdot I_e \cdot \sigma}{q})) \tag{5.5}$$

where q is the charge, N_t is the number of charges, t is the time, I_e is the current of the charges in the SCR of the semiconductor and σ is the capture cross section. The electric field in the SCR $\overrightarrow{E}(t)$ in a semiconductor can be written as

$$\overrightarrow{E}(t) = \overrightarrow{E}(0) + A \cdot (1 - exp(\frac{-t \cdot I_e \cdot \sigma}{q})) \tag{5.6}$$

where A describes the amplitude of decay, which is dependent on structure design.

In equilibrium, I_e is equal to the current of ions at the surface due to the corona charging. Hence, for a decrease in electric field in the SCR due to tunneling, the EFISH intensity, according to eq. (5.4) can be written as

$$I_{\mathrm{EFISH}}(2\omega) \sim (\overrightarrow{P}_{\mathrm{total}})^2 \sim (\overrightarrow{E}(0) + A \cdot (1 - exp(\frac{-t \cdot I_e \cdot \sigma}{q})))^2 \tag{5.7}$$

When the corona field is turned off, due to dissipation of the corona charges, the electric field in the SCR of the semiconductor obeys,[139]

$$\overrightarrow{E}(t) = \beta \cdot ln(B(t + t_0))^{-1})^2 \tag{5.8}$$

where β is the field dependency with SCR thickness, $B = C\beta/\epsilon_i$, C is the capacitance, ϵ_i is the insulator dielectric constant and t_0 is the constant of integration obtained from $\overrightarrow{E}(0)$.

From eq. (5.4), the EFISH intensity upon turning the corona field off can be expressed as

$$I_{\mathrm{EFISH}}(2\omega) \sim (\overrightarrow{P}_{\mathrm{total}})^2 \sim (\beta \cdot ln(B(t + t_0))^{-1})^2 \tag{5.9}$$

It should be mentioned that the oxide thickness influences the electric field, since a voltage drop appears over the oxide layer, however this decrease in field is small compared to the applied corona field. Moreover, fixed charges in Al_2O_3 and interface charges influence the dc-induced polarization. Furthermore, multiple reflections in the oxide layer are neglected, since the SHG intensity is similar for all the samples with different oxide thickness and is predicted to be small over the range of 20nm, under non-Brewster angle conditions.[140]

5.3 Results and discussions

The SHG intensity of the Si-SiO_x-Al_2O_3 structures is shown in fig. 5.2. Initially, the SHG intensity corresponds to an uncharged situation. In situation (a) in fig. 5.2, the uncharged sample is schematically represented, where the direction and the strength of the electric field in the SCR is represented with an arrow. Upon applying a positive external field at $t = 0$s, the SHG response decreases dramatically, which indicates that the electric field in the Si SCR decreased as well, according to eq. (5.4). Due to the corona field, electrons from the silicon

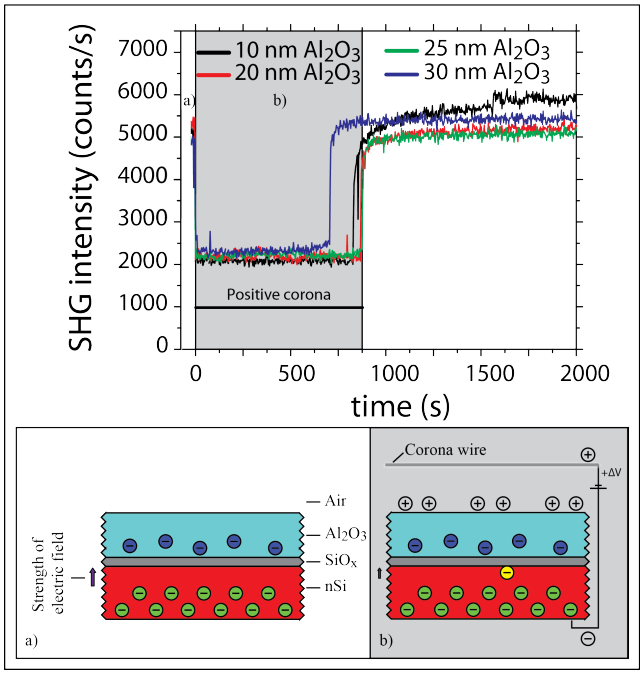

Figure 5.2: SHG response upon applying a positive corona field to an Al_2O_3 passivated Si wafer. The initial SHG response corresponds to the uncharged sample. This situation is schematically represented in situation a). The strength of the electric field in the SCR of Si is represented by the magnitude of the arrow. At 0s, a positive corona field of 2.7kV is applied, resulting in a drop in SHG intensity. The negative doping charges are attracted to the interface, shown in situation b). After several hundreds of seconds, the corona field was turned off, resulting in a recovery of the SHG signal to its original intensity.

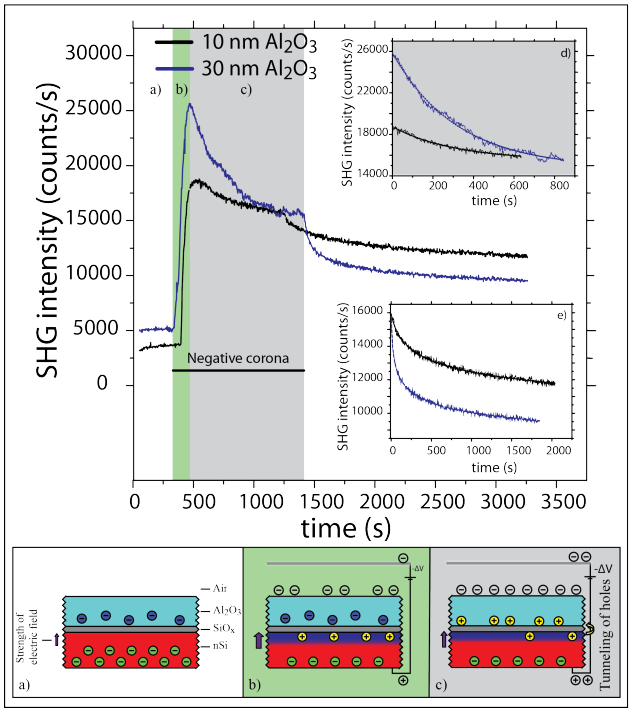

Figure 5.3: SHG response upon applying a negative corona field to an Al_2O_3 passivated Si wafer. Similar curves were obtained for another thickness of the Al_2O_3 layer. The initial SHG response corresponds to the uncharged sample. This situation is schematically represented in situation a). The strength of the electric field in the SCR of Si is represented by the magnitude of the arrow. Upon applying a -3kV corona field, a large increase in SHG intensity is observed. This correlates to the increase in electric field in the space-charge region of Si, shown in situation b). From a certain electric field over the oxide layer, tunneling of holes from Si to Al_2O_3 occurs, which reduces the effective electric field in the silicon space-charge region. Hence, the SHG intensity drops exponentially, as predicted by theory. Schematically, the situation is described by situation c). Upon switching the corona charge off, the SHG drops logarithmically due to the removal of charges in the space-charge region in Si. However, the SHG signal does not recover to the initial intensity due to remaining positive charges in the oxide layer, enabling a larger electric field in the silicon space-charge region. In inset d), the fitting on the time-shifted tunneling to an exponential decay of situation c) is shown. Similar relaxation times (313s vs. 320s) are obtained for both the 10nm and 30nm thick oxide layer. In inset e), the logarithmic decay upon turning the corona field off is shown.

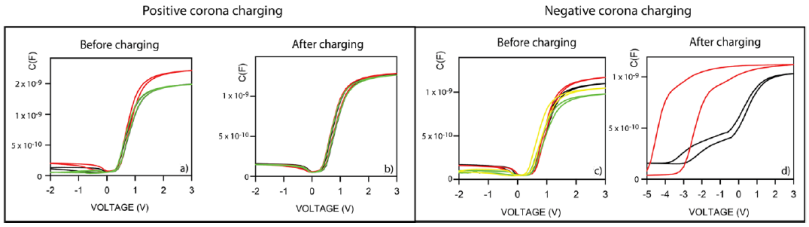

Figure 5.4: Capacitance-voltage characteristics before and after negative corona poling. For the positive corona charging, there is no significant difference in the CV response (a) vs b)), confirming that the structure was not electrically altered during the corona poling. For the negative corona, there is a clear difference in CV response (c) vs d)), indicating that there is an electrical difference between the samples before and after poling. Due to the shift in flat-band potential and the increase in hysteresis in b), it is clear that the amount of charges in the oxide layer increases and change sign to positive charges.

bulk are attracted to the Si/oxide interface, resulting in a decrease in field in the silicon space-charge region (situation b in fig. 5.2). Upon increasing the corona field, no drastic change is observed in the structure, only an increase of the amount of charges near the interface. At 700s or 860s, depending on the sample, the electric field is switched off, whereby the SHG signal recovers to its original intensity, i.e. the intensity level without electric field. Hence, the charge distribution recovers to the original structure and the field in the SCR increases due to the dissipation of charges. It can be clearly observed that the charging effect is equal for all structures, independent of oxide thickness. This is easily explained, because the voltage drop over the oxide layer is small, compared to the corona field that is used to charge the surface. The initial (before corona charging) and final (after removal of the corona field) SHG intensities are equal, indicating that the electrical properties in the Si-SCR have not been altered by the measurements, which is confirmed by capacitance-voltage (CV) measurements shown in fig. 5.4. For the positive corona, the hysteresis difference before and after the charging is similar. Moreover, the positive flat-band potential is not shifted. From this, we can conclude that the initial and final amount of charges in the oxide layer are equal and that the small amount of charges present in the oxide layer are negative.

Applying a negative corona field induces a drastic increase in SHG intensity compared to the uncharged initial intensity (fig. 5.3). Due to the negative corona field, electrons are removed from the SCR and minority carriers (i.e. holes) are attracted to the interface. The minority carriers increase dramatically the electric field, inducing a large electric field built-up in the Si space-charge

region. Due to the positive nature of the charges, a larger field arises in the SCR. This results in an increase in SHG intensity, which is described in situation b in fig. 5.3. However, after a few tens of seconds, the SHG intensity starts to decreases exponentially. The observed decrease in SHG intensity, can be explained by tunneling, since the electric field over the SiO_x layer becomes too large. The internal electric field in the SCR of silicon decreases exponentially, according to eq. (5.6). Positive charges tunnel through the SiO_x layer, resulting in a decrease of minority carriers in the Si SCR. According to eq. (5.7), the EFISH contribution of this electric field decreases as well (shown in inset d in fig. 5.3). Schematically, the situation is represented in situation c in fig. 5.3. Moreover, when corona field is turned off and the charges dissipate, the change in SHG intensity can be described by eq. (5.9). The fittings are shown in inset e in fig. 5.3. Furthermore, the final SHG response is considerably larger than the initial value, suggesting that the structure is electrically changed during the measurement. The effect of tunneling can be confirmed by CV measurements, shown in fig. 5.4. The CV characteristics of the charged structure exhibit a shift to negative voltage and a large hysteresis. Due to this shift of flat-band potential and large hysteresis, the positive nature of the charges in the oxide can be confirmed. Hence, holes tunneled from the Si layer to the Al_2O_3 layer and remained in the oxide layer. This results in a larger field in the space-charge region, enabling a larger final SHG response, compared to the initial SHG response.

5.4 Conclusions

We show that, due to changes in charge density in the space-charge region of silicon, the time-dependent second-harmonic generation response of a structure can be altered. Furthermore, tunneling of holes under the influence of a positive corona field is observed with second-harmonic generation, which is confirmed by capacitance-voltage measurements. Previous methods of electric-field induced second-harmonic generation could not separate the influence of the metal layer and the important Si space-charge region, while our method can. This approach can lead to valuable insights into quantum well devices.

Acknowledgements

This work was supported by the Katholieke Universiteit Leuven (GOA). M.K.V. acknowledges the useful scientific discussions with W. Brullot, S.

Vandendriessche and M. Bloemen. V.K.V. is grateful for the financial support from the fund for scientific research Flanders (FWO-Vlaanderen).

Chapter 6

Electric-field-induced second-harmonic generation demonstrates different interface properties of molecular beam epitaxy grown MgO on Si

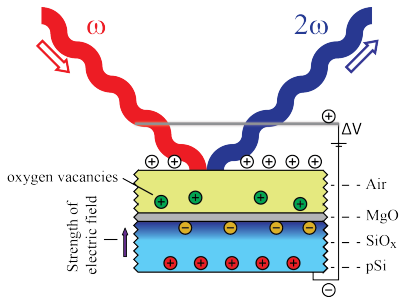

Figure 6.1: Graphical table of content

When an external electric field is applied on a metal-oxide-semiconductor field-effect transistor (MOSFET), charges can migrate through the structure, as shown in chapter 5. The electrical properties of the device depend on the amount of charges present and on the quality of the interfaces in the structure. In this chapter, the electric field-induced second-harmonic generation (EFISH) response of a MgO/Si MOS structure is investigated. In contrast to chapter 5, we now tried to identify the charge carrier which is responsible for the EFISH response.

It is shown that the interface determines the electrical properties of a MgO capped semiconductor. Electric field-induced second-harmonic generation (EFISH) reveals the differences of the first monolayer of MgO caused by altering the growth sequence of the molecular beam epitaxy. The EFISH contribution in p-doped Si with a MgO layer is altered because of the migration of oxygen vacancies. Moreover, the electronic properties of the different semiconductor-oxide interfaces are distinguished by EFISH upon applying an *in situ* corona field.

The MgO covered Si samples were prepared by drs. Chen-Yi Su. Also the capacitance-voltage characteristics were determined by her. I performed the SHG measurements and data analysis. I submitted our work to Journal of Physical Chemistry C, where it was accepted for publication.

M. K. Vanbel, C.-Y. Su, J.-P. Locquet, T. Verbiest,
Electric field-induced second-Harmonic generation demonstrates different interface properties of molecular beam epitaxy grown MgO on Si
Journal of Physical Chemistry C, **118** (4), 1919-1924 (2014).

Additional to the explanation in chapter 1 of distribution of potentials over a gate stack structure and the related band bending, fig. 6.2 clarifies the methodology used in this chapter as well as the observed effects. However, the representation of the structures in this illustration of the band bending is for ideal structures, instead of structures with charges in the oxide layer or interface traps. The electron affinity χ, band gap E_g, Fermi level E_F and energy of the conduction, intrinsic and valence band, E_c, E_i and E_v respectively are illustrated, corresponding to their definitions. In our case, the metal layer represented in the figure is in fact air, where charges accumulate at the oxides surface. Although a Fermi level is not often defined for air, it is possible. But for a clear image, we represent the air by a metal layer of which the Fermi level can be changed when an external voltage is applied. In equilibrium, (i.e. without applying a voltage which is at flatband potential conditions for an ideal MOS structure) the Fermi level of the metal is equal to the Fermi level of the

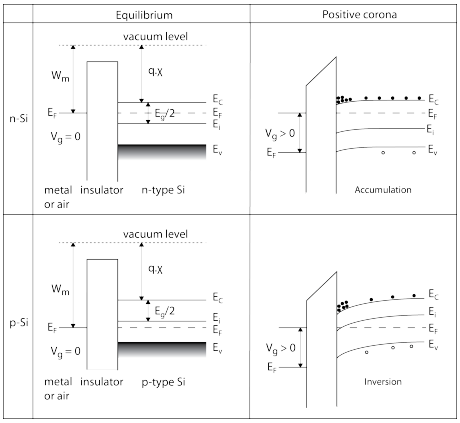

Figure 6.2: Illustration of band bending for both n and p-doped si when a positive corona is applied to a gate stack. After Sze.[6]

semiconductor. Note that the intrinsic energy levels define the doping of the Si. When a positive corona is applied, the Fermi level of the metal layer drops. Part of this drop in Fermi level is accounted for by the oxide layer, which is represented as the alteration of the direction of the energy band of the oxide layer. The other part is accounted for by the bending of the energy band inside the semiconductor for both types of doping. Due to the banding of the energy bands to lower energies, the charges in the conduction band, i.e. electrons, are trapped near the interface. For n-Si, the electrons are the majority charge carriers, while for p-Si, electrons are minority carriers.

These charges are responsible the some effects probed in the experiment described in this chapter. For the MgO passivated n-doped Si, the second-harmonic signal will be dominated by charge accumulation due to band bending. In the case of MgO passivated p-doped Si, the electrons are the minority carriers. Therefore, the steady state condition when the corona field is turned on, has to be reached by other types of charges. It is shown that the charges present in the oxide layer are responsible for this behavior. In the publication, different types of charges are excluded as candidate for this charge migration in the structure. It is however believed that the MOS structure itself remains intact while its composition remains invariant as well.

Abstract

The ability to tune the electrical properties of a metal-oxide-semiconductor structure, especially the chemical nature and the associated electrical properties of the first few layers of the oxide, is of increasing importance in the semiconductor industry. Oxide deposition using molecular beam epitaxy facilitates the control of the interface with the semiconductor at the atomic level. Depending on the characteristics of the first monolayer, the electric-field-induced second-harmonic generation can be shifted, which is correlated to the flat-band voltage shift. Three different oxide-semiconductor interfaces, which originate from different first monolayers, are investigated by electric-field-induced second-harmonic generation and are shown to exhibit different electronic characteristics. Migration of positive oxygen vacancies from the oxide layer toward the Si space-charge region is observed.

6.1 Introduction

In metal-oxide-semiconductor (MOS) structures, the oxide-semiconductor interface is of critical importance for device operation. Excessive scaling of semiconductor devices dictates the need for more advanced materials because the traditional Si-SiO_2 stack fails for very thin SiO_2 in device operation because of high leakage or tunneling current,[141] reduced drive current,[142] enhanced power consumption, and poor device reliability.[143] Thus, alternative dielectrics, which exhibit a higher capacitance and lower leakage current than those of SiO_2, are required.[144] With moderate dielectric constant and band gap, MgO is thus a promising dielectric material. Because the electrical properties of the high-k dielectric-semiconductor interface determine the device operation of the MOS device, it is crucial to probe these electrical properties at the interface, which can depend on the growth conditions.[145, 146] Because of the interface specificity of second-harmonic generation (SHG), this technique is often used to determine the interface properties, for both organic,[147, 148] and inorganic structures.[49, 91, 130] The ability to probe buried interfaces offers advantages over other surface techniques. As a consequence, SHG has been shown to be a versatile method to characterize semiconductor interfaces.[58] Moreover, electric field-induced second-harmonic generation (EFISH) has been used extensively to characterize electrical properties of passivated semiconductors.[32, 149] Typically, EFISH can be observed by exposing the structure to intense laser light to induce an internal electric field due to photoinduced charging, which has been reported to occur for different passivation layers, e.g., SiO_2,[102] MgO,[150] Al_2O_3, HfO_2, and ZrO_2.[56] Alternatively, EFISH experiments can be conducted by applying an external electric field on a deposited metal electrode.[32, 133]

Recently, an EFISH experiment was conducted by using a corona wire on top of a semiconductor sample without the need of the deposition of a metal electrode.[16] This approach enables the separation of the SHG contribution of the metal-oxide interface from the SHG contribution of the oxide-semiconductor interface.

The changes upon charging an oxide-semiconductor structure are often explained only by energy band diagrams.[149] To emphasize the role of electrical properties of the interface during operation, the charging of the oxide on the semi- conductor structures must also be interpreted as interface trapped charges and oxide charges, which cause distortions of the capacitance-voltage curves, such as stretch out and flat- band voltage shifts. These flat-band voltage shifts can, in addition to capacitance-voltage characteristics, also be investigated using EFISH experiments, which enables the correlation of both techniques.[64]

Here, we report time-dependent EFISH responses upon applying a positive electric corona field on MgO on silicon structures. The MgO layer is formed using different sequences during molecular beam epitaxy growth, which results in an altered composition of the first monolayer.[151] When a positive corona is applied, a weak inversion in p-doped Si will be formed, while an accumulation layer will be formed in n-doped Si. When a weak inversion layer in p-doped Si is formed, positive oxygen vacancies migrate from the MgO layer toward the space-charge region (SCR) of Si and a decrease in total SHG response is observed. Depending on the first monolayer, the amount of oxygen vacancies varies, which results in different charge migration behavior. When an accumulation layer in n- doped Si is formed, electrons are attracted to the oxide-silicon interface and no charge migrates from the oxide layer. The oxide-semiconductor structures with different interfaces exhibit different electrical properties. The electrical properties of the structures, probed by the EFISH experiment, are correlated to capacitance-voltage characteristics. The flat-band voltage shift associated with the different few monolayers of MgO are distinguished in the EFISH experiments.

6.2 Sample preparation

The MgO films were deposited in an ultra high vacuum MBE system with a base pressure of 2×10^{-9}mbar on both p-type and n-type Si(100) substrates.[64] The dopant concentration is 1×10^{15} and 4.4×10^{14}cm^{-3} for p-doping and n-doping, respectively. Before entering the MBE system, the Si wafers were first dipped in HF to remove the native oxide. The resulting H-terminated surfaces were then heated for H_2 desorption. The three different interface treatments were made possible by introducing different species in the beginning of the

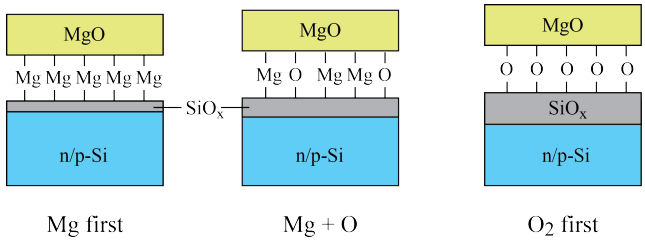

Figure 6.3: Sequence of deposition by molecular beam epitaxy (MBE). When the sequence is altered, the first monolayer of the MgO layer can be tuned. When Mg is deposited first, the oxide/semiconductor interface will be Mg rich. When O_2 is deposited first, this interface will be oxygen rich.

oxide deposition sequence. In the case where magnesium was deposited first, one monolayer of Mg was deposited before introducing oxygen into the system. When the oxygen was introduced first, the structure surface was exposed to O_2 for 1min. After this step, the MBE sequence continued. The thickness of the suboxide layer is expected to be thicker when oxygen is introduced first. Details of this method are published elsewhere.[151] A schematic representation of the formed structures, with an emphasis on the first monolayers, is depicted in fig. 6.3.

6.3 Experimental methods and theoretical description

The electric-field-induced second-harmonic generation experiments were performed using a femtosecond (120fs, 80MHz) pulsed 800nm Ti-sapphire laser with an average output power of 70mW. At these power levels, small photoinduced charging was observed because the initial time-dependent second-harmonic intensity varied little. Applying the corona charge was performed after the initial SHG signal was constant. The EFISH measurements were performed in a p_{in}-p_{out} polarizer-analyzer combination with an incidence angle of 45 ° with respect to the surface normal. The full experimental setup with the *in situ* corona charging is described elsewhere.[16] A voltage of 3.3kV was used while the leakage current through the samples during the corona charging was kept constant. The corona wire was placed 2cm from the sample surface. Depending on the sign of the corona charge, the electric-field- induced second-harmonic generation contribution will change.[133] Moreover, depending on the type of doping under positive corona, the EFISH contribution will also change.

The total second-harmonic signal from an oxide on semiconductor structure can be described by

$$\overrightarrow{P}^{\text{eff}}(2\omega) = \overrightarrow{P}^{D} + (2\omega) + \overrightarrow{P}^{Q}(2\omega) + \overrightarrow{P}^{\text{EFISH}}(2\omega) \tag{6.1}$$

where $\overrightarrow{P}^{D}$ describes the electric dipole contribution, $\overrightarrow{P}^{Q}$ the electric quadrupole contribution, and $\overrightarrow{P}^{\text{EFISH}}$ the electric-field-induced second-harmonic generation contribution. Figure 6.3 can be written as

$$\overrightarrow{P}^{\text{eff}}(2\omega) = \chi^{D} : \overrightarrow{E}(\omega)\overrightarrow{E}(\omega) + \chi^{Q} \vdots \overrightarrow{E}(\omega)\nabla\overrightarrow{E}(\omega) + \chi^{(3)}\overrightarrow{E}(\omega)\overrightarrow{E}(\omega)\overrightarrow{E}_{z,dc} \tag{6.2}$$

where χ^{D} , χ^{Q} and $\chi^{(3)}$ are the dipolar, quadrupolar, and EFISH nonlinear susceptibility tensors, respectively, and $\overrightarrow{E}_{z,dc}$ is the internal electric field. When the second-harmonic signals are measured, the signal cannot be uniquely attributed to one of these susceptibilities. However, when an external electric field is applied, which in turn influences the internal electric field, the change in second-harmonic signal can be attributed to the $\chi^{(3)}$ EFISH tensor, while χ^{D} and χ^{Q} remain constant.

When a gate voltage V_g is applied to an oxide-semiconductor gate stack, the voltage is divided over the different layers of the gate stack.[144]

$$V_g = \frac{W_m}{q} - \left(\frac{\chi + E_g/2 + k_B T log(N_a/N_i)}{q} \right) + V_{ox} + \frac{\Phi}{q} \tag{6.3}$$

where W_m is the work function of the metal layer, χ the electron affinity, E_g the band gap, N_a/N_i the relative dopant concentration, and Φ (in eV) the band bending. Because the Fermi level is equal for all measured structures and W_m = 0, the voltage is divided only between the band bending and the voltage over the oxide layer.

When a corona is applied, the number of charge carriers will vary as a function of time. The empirical formula to quantify the change in charge carriers in second-harmonic generation can be written as[16]

$$I_{\text{EFISH}}(2\omega) \sim C\left|\overrightarrow{E}(0) + A \cdot (1 - exp(\frac{-t \cdot I_e \cdot \sigma}{q}))\right|^2 \tag{6.4}$$

where C incorporates the susceptibility tensor components and the geometry of the experimental setup; A describes the amplitude of the decay, which is dependent on the structure, I_e the current of charges in the space-charge region (SCR), σ the capture cross section, and q the total charge.

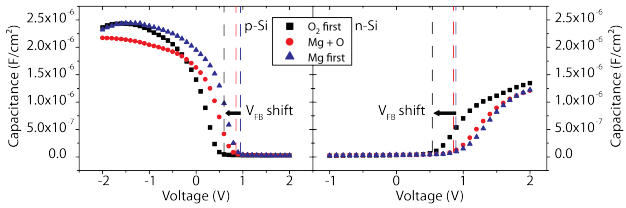

Figure 6.4: Capacitance-voltage characteristics of MgO passivated p-doped and n-doped silicon respectively. The dashed line indicates the theoretical flat-band voltages for the different structures. A clear negative flat-band potential shift due to positive charges for both n-type and p-type substrates can be observed when an oxygen-rich interface was grown.

The capacitance-voltage measurements were performed after depositing 40nm Pt contacts through a shadow mask. The MOS capacitor structure was mounted in a probe station connected to a Keithley 4200 Semiconductor Characterization System. High-frequency capacitance voltage characteristics were measured at 1MHz on $40 \times 40\mu m^2$ pads.

6.4 Discussion and results

From fig. 6.4, it can be observed that the capacitance-voltage characteristics can shift, depending on the deposition sequence of the MBE process. Specifically, the flat-band voltage is shifted toward smaller positive potentials for structures where oxygen was deposited first, compared to the combination of Mg and O and the Mg first structures. This flat-band shift is a clear expression of a difference in number of charges in the structure. For the case of high-k dielectrics,[152, 153, 154] and more specifically MgO,[155] this shift in flat-band voltage has been related to the presence of oxygen vacancies in the high-k oxide layer. This positively charged oxygen vacancy is created when a Mg atom substitutes a Si atom in the SiO_x layer. The positive charge of the resulting oxide layer influences the electrical properties of the structures and influences their behavior in EFISH measurements.

The time-dependent SHG response, upon applying a positive corona on a p-doped substrate with a deposited MgO film, is shown in fig. 6.5. Three different situations can be distinguished in the SHG response curves, and their charge distribution is illustrated. Initially, the SHG intensity corresponds to the situation where no external electric field is applied, which is depicted as

situation a in fig. 6.5. It should be mentioned that there could be an EFISH contribution to the total SHG signal not due to the application of an external potential, corresponding with eq. (6.2). An internal electric field can be present because the presence of defects, vacancies, or dangling bonds can lead to charges distributed in the structure, which in turn lead to an electric field. Combined with the influence of the dopant, the overall potential distribution in silicon leads to an EFISH contribution or electric quadrupolar contribution to the SHG signal.

When positive corona of 3.3kV at $t = 175$s is applied, the SHG signals increase drastically. The externally applied electric field influences the internal electric field, giving rise to the EFISH contribution in the total SHG signal. Under the presence of a positive corona on the p-doped substrate, a weak inversion layer in the SCR of silicon is formed; hence, the positive doping charges are repulsed from the interface. This charge distribution is illustrated as situation b in fig. 6.5. According to eq. (6.3), the band bending is altered. Because of the induced negative character of the weak inversion layer in Si, the electric field in the space-charge region increases, which according to eq. (6.2), gives rise to a change in SHG intensity. Because the absorption depth in Si of the fundamental wavelength is 10μm and the band bending is limited to 1.5μm, all charges, including doping charges, can contribute to the total EFISH contribution. Hence, the EFISH contribution arises from all charges present near the interface in both the oxide layer and semiconductor and the charges from the dopant implantation.

After several seconds, depending on the composition of the first monolayer, the total SHG intensity starts to decrease. The decrease in SHG intensity from its maximal value can be attributed to removal of charge carriers from the oxide layer to the top of the silicon layer, which decreases the electric field in the SCR.[16] Because the electron concentration in the Si SCR under weak inversion is very low (approximately 8000cm^{-3}), the equilibrium is reached by charge carriers from the oxide layer, which migrate slowly through the structure. These charge carriers are positive moieties from the oxide layer, which can be deduced from the capacitance-voltage characteristics. The electric gradient in the weak inversion layer enables the positive charges to migrate from the oxide layer toward the silicon SCR. Because of the positive nature of the charges in the oxide, the candidate number of charge carriers from the general possible oxide defects can be reduced.[156] Mobile ionic charge introduction, and more specifically sulfur implantation during the MBE process, results in positive charges in the oxide. However, the amount of sulfur implantation should be equal for all structures because their total MgO thickness is equal. Hence, a different first monolayer cannot give rise to a difference in mobile ionic charge density. The same argument holds for the fixed oxide charge. Moreover, they

are not mobile under an applied field. The effect of the interface traps on the electrical properties is dependent on the position of the Fermi level at the interface. This Fermi level changes in the order of 0.1s while sweeping the voltage. Hence, the effect of the interface traps is visible only at these time scales in the EFISH response. The remaining charge carriers, responsible for the EFISH contribution over hundreds of seconds upon applying an corona field, are thus Mg^{2+}, Mg^{+}, and oxygen vacancies.

The discrimination between the Mg ions and the oxygen vacancies can be obtained when correlating the capacitance- voltage characteristics to the EFISH response. From fig. 6.5, it can be observed that the initial EFISH contribution for the O_2 first structure is highest, then the Mg + O structure, and then the Mg first structure. Moreover, the relative difference of the maximal and the initial SHG intensity follows this trend. The relative difference of the initial and the maximal SHG intensity enables the calculation of solely the EFISH contribution. This trend is consistent with the shift in flat-band potential, which can be described by the oxygen vacancy model.[153] Because of the oxygen-rich interface of the O_2 first sample, the suboxide layer becomes effectively thicker compared to the Mg first sample. A thicker suboxide layer results in a higher concentration of positive oxygen vacancies due to the migration of Mg atoms into the SiO_x layer and O atoms from the SiO_x to the MgO layer. Hence, the presence of more positive oxygen vacancies in the suboxide results in a larger electric field when a weak inversion layer is formed. The increased internal electric field results in a higher SHG intensity. When Mg is deposited first, fewer oxygen vacancies are present in the suboxide, which results in a smaller electric field. Hence, the SHG intensity of the Mg-rich first monolayer is smaller than that of the O_2 rich first monolayer. The presence of the positive oxygen vacancies could be enhanced by laser-induced desorption of Mg ions with a photon energy less than the band gap energy.[157] The small decrease in the initial SHG intensity is a direct evidence of this effect. The presence of the oxygen vacancy has a significant influence on the surface or interface properties.[158, 159]

The decay of the SHG intensity is correlated to the migration of oxygen vacancies. Because the voltage is mostly divided into band bending, the redistribution of oxygen vacancies is expressed in the SHG signal because this signal arises mostly from the oxide-Si and Si layer.[130] Hence, the charge migration of positive charges from the oxide is observed because the Si band bending, which is primarily probed by means of EFISH, is altered by these charges.

Situation c in fig. 6.5 represents the equilibrium condition when applying the corona field. Because of the redistribution of the charges in the oxide in situation b, the amount of charges in the silicon SCR is smaller, thereby reducing the

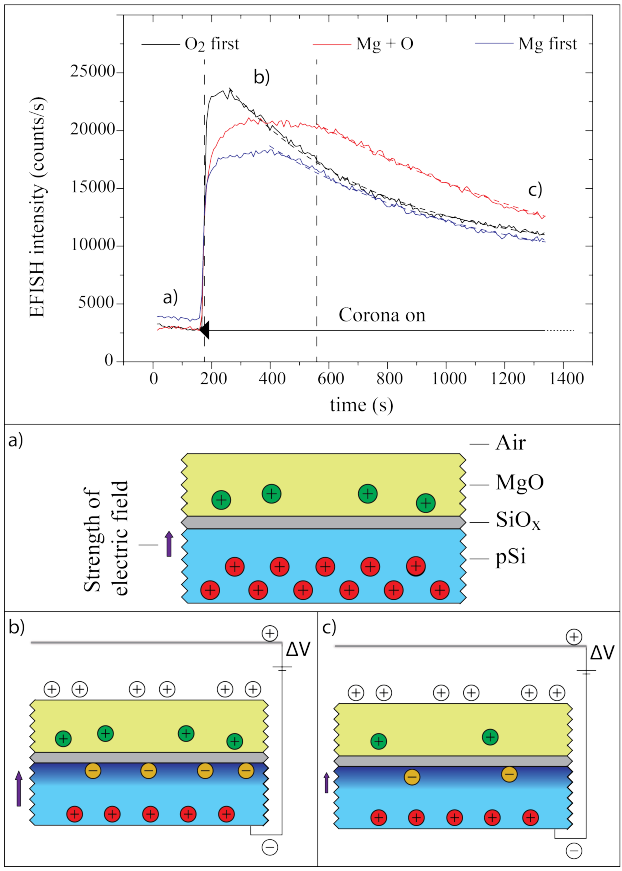

Figure 6.5: Electric-field-induced second-harmonic response for MgO on p-doped Si changes upon applying a positive corona. The initial signal corresponds to the externally uncharged sample, although charges can contribute to the total initial SHG signal (situation a)). The green charges represent the oxygen vacancies, and the red charges are the doping atoms. When a positive corona field of 3kV is applied, the SHG intensity increases drastically, which is direct evidence of a change in electric field in the silicon space-charge region and the formation of an inversion layer. A schematic representation of the charge distribution of this situation is depicted in b), where the vertical dashed lines include the maxima of all curves. The yellow charges represent the induced charges in the SCR of Si, which form the weak inversion layer. The Si SCR is depicted as the dark blue gradient. Then the SHG signal starts to decrease exponentially. Because of migration of positive charges from the oxide layer, the electric field decreases in the silicon space-charge region, as shown in c). Depending on the first monolayer of the MgO layer, the decrease of the SHG signal occurs slower or faster because of differences in availability of oxide vacancies. The decay in SHG intensity is fitted according to eq. (6.4) and is shown as a dashed line.

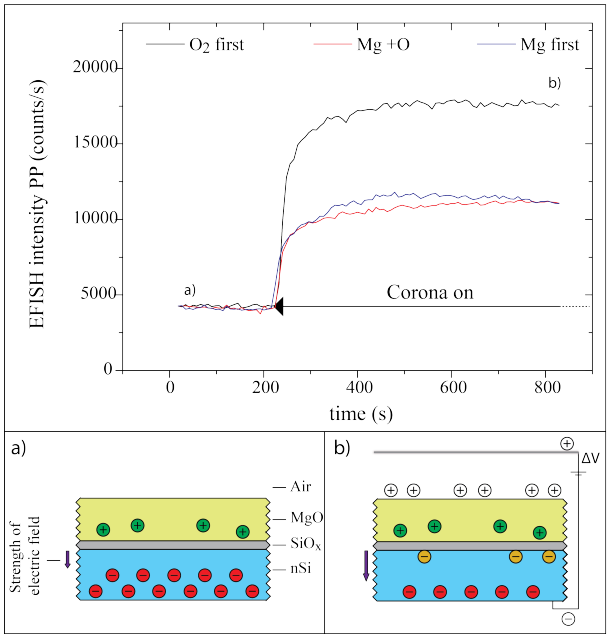

Figure 6.6: Electric-field-induced second-harmonic signal for MgO-passivated n-doped Si changes upon applying a positive corona. The SHG intensities are normalized to the O_2 first structure to emphasize the role of the EFISH contribution. The initial signal (situation a)) corresponds to the externally uncharged sample, of which a schematic representation of the charge distribution is depicted. The green charges represent the oxygen vacancies, and the red charges are the doping atoms. Upon applying a positive corona field of 3kV, the SHG intensity increases and saturates at a constant value because of the formation of an accumulation layer in the silicon space-charge region (situation b), where the yellow charges represent the induced charges in the SCR of Si, which form the accumulation layer). Depending on the first monolayer, the EFISH contribution changes and relates to different electrical properties of the interface.

voltage over this layer. The SHG intensity decreases to a steady state, where no migration of charges is occurring and the electric field normal to the Si layer is smaller than that of the initial charge distribution with the corona field on.

It should be noted here that the fitting of the decay of the SHG intensity according to eq. (6.4) also represents the difference in electrical properties of the structures (dashed line in fig. 6.5). Changes in the decay constant

represent changes in σ/q because the leakage current is kept constant during the experiment. In addition, the width of the peak in Figure 2 can be correlated to the speed of charge displacement. It has been shown that this can be attributed to differences in availability of defect sites and their distance to the interface.[160] Depending on the first monolayer, the depth profile of oxide charges may differ, leading to different internal electric fields.

The time-dependent SHG intensity upon applying a positive electric corona field on a MgO passivated n-doped substrate is shown in fig. 6.6. Two different situations can be distinguished in the SHG response curves, and their charge distribution is illustrated. The SHG intensities are normalized to the O_2 first structure. The differences in initial SHG intensity confirm that the Si/MgO interface is different for the three structures and that their charge distribution may alter as well. However, a normalization emphasizes the role of the EFISH contribution. After $t = 223$s, a positive corona field was applied to the structures and an immediate increase of the SHG intensity can be observed (situation b). Because of the positive external corona field, an accumulation layer in the silicon space-charge region is formed, which increases the internal electric field. This internal field is probed by EFISH according to eq. (6.2). Two hundred seconds after applying the corona field, the SHG intensity stabilizes to a constant value, which arises from the stagnating internal electric field in the Si SCR. Because the electrons are now the majority carriers, the electrical equilibrium will be reached by migrating electrons from the Si SCR toward the Si-oxide interface. The electrons in the SCR of Si can respond quickly to the applied electric field and are abundant. Moreover, no charge carrier exchange between the oxide and silicon can be observed because for n- doped Si, the applied voltage is mostly distributed over the oxide layer and only partially expressed as band bending.[144] This change in band bending contributes to the SHG signal, whereas the voltage over the oxide layer does not. Hence, the migration of charges when the voltage is applied is not expressed in the SHG signal. Nevertheless, the differences in maximal SHG intensity, upon applying a corona field, can be correlated to the capacitance-voltage characteristics.[56] When the EFISH contributions are compared with the sequence from highest to lowest capacitance for positive voltage values, the trend and absolute values correspond. The O_2 first structure exhibits the highest capacitance and the highest EFISH contribution. Whereas the Mg + O and Mg rich interface structures exhibit lower but similar capacitances at positive voltage values and corresponding EFISH contributions. Hence, the difference in electrical properties of the different first monolayers is probed by SHG.

Note that for both n-Si and p-Si, the change in SHG intensity is an increase although an inversion layer is created for p-doped Si while an accumulation layer

is formed in n-doped Si. Nevertheless, the dipole direction in the Si SCR in the structure is similar for both structures; namely, out of the structure toward the corona wire. Hence, according to eq. (6.2), the $E_{z,dc}$ has the same direction in both cases, which in turn results in an increase of the SHG intensity for both doped substrates.

6.5 Conclusions

In conclusion, the interface determines the electrical properties of a MgO-passivated semiconductor. Electric field-induced second-harmonic generation (EFISH) reveals the differences of the first monolayer of MgO caused by altering the growth sequence of the molecular beam epitaxy. The EFISH contribution in p-doped Si with a MgO layer is altered because of the migration of oxygen vacancies. Moreover, the electronic properties of the different semiconductor-oxide interfaces are distinguished by EFISH upon applying an *in situ* corona field.

Acknowledgments

This work was supported by the KU Leuven (GOA, DBOF). M.K.V. acknowledges the useful scientific discussions with M. Bloemen, W. Brullot, S. Vandendriessche, and M. Menghini.

Chapter 7

SHG/2PF microscopy of single and multi-layer graphene

The ITRS roadmap suggests other types of materials to keep on increasing the performance of transistors in integrated circuits. One of the suggested possibilities is graphene.[43] This zero bandgap semi-metal has the advantages of a very high charge carrier mobility at room temperature compared to Si. Intregrating graphene as channel material in a transistor is still challenging, however the characterization of this material has become a hot research topic. Due to the small size of pristine graphene, nonlinear optical microscopy could give valuable insight in the material optical and interface properties. We determined the capability of visualizing pristine and chemical vapor deposition (CVD) transferred graphene on glass using second-harmonic generation (SHG) and two-photon fluorescence (2PF).

The graphene samples were prepared by drs. Alexander Klekachev of imec and he performed the Raman measurements on the single and double layer graphene sheets. He grouped our findings into an SPIE proceedings publication. I performed the SHG and two-photon fluorescence (2PF) measurements on graphene in collaboration with dr. Monique van der Veen. Drs. Klekachev presented our work at SPIE Optics and Photonics 2012 in San Diego.

A. V. Klekachev, I. Asselberghs, C. Huyghebaert, **M. Vanbel**, M. A. van der Veen, A. L. Stesmans, M. M. Heyns, S. De Gendt, T. Verbiest,
SHG/2PF microscopy of single and multi-layer graphene
Proceedings to SPIE, **8474**, 2012, 847405.

After this research, it was revealed that degradation of graphene is unavoidable when illuminating with high intense fundamental laser light. Therefore, further steps were undertaken to be able to measure a polarization pattern, while the structure was degrading. This research is presented in chapter 8.

Abstract

Since the discovery of graphene in 2004 by Novoselov and Geim, a lot of research emphasis has been directed towards its characterization. Most of the important scientific breakthroughs have been obtained on exfoliated graphene (produced via the well known 'scotch tape' method), nowadays, different synthetic routes have been developed to obtain large-scale graphene. Among several optical techniques, Raman spectroscopy is the one most often employed to characterize the defects, number of graphene layers and other properties of the graphitic films regardless of their fabrication method. In this work, we will report on the microscopic imaging of the two-photon fluorescence (2PF) properties and the second-harmonic generation (SHG) in both single layer and few layer graphene.

7.1 Introduction

From the family of all carbon materials, built only from sp^2 hybridized C-atoms, graphene is discovered the latest and it is the 2 dimensional allotrope, being only one single atom thick.[161] The discovery was achieved by Novoselov and Geim in 2004, by basically peeling of a single layer from natural graphite using adhesive tape.[69] This method is referred to as the scotch tape method, and is still the most employed method, due to its high accessibility. It also results in achieving the highest quality graphene samples available so far. The increased research boost after 2004, revealing many intriguing and unique properties, such as strong field effect, high carrier mobilities and low sheet resistance,[73, 74] only increased the need for synthetically grown graphene. Different methods are currently available for growing graphene layers in artificial conditions obtaining large uniform areas. However, difficulties are still encountered due to the presence of grain boundaries and defects in the graphene lattice in synthesized graphene. These anomalies alter some of the unique properties observed in exfoliated material. Another degree of variation of graphene properties is the number of layers and their stacking. The latter can result in different electronic structure as has been recently evidenced in three-layer graphene by Raman scattering spectroscopy,[162] and electrical characterization in transistor configuration.[163] Nowadays, a broad variety of possible applications are screened, as well as large emphasis is put into fully understand the behavior. Yet, second-harmonic generation (SHG) and two-photon fluorescence (2PF) imaging are capable of providing structural information with spatial resolution. Examples are the organization of nanoparticles[164, 165] and host/guest systems.[18, 166] Even point group symmetry determination is possible based on nonlinear optical microscopy alone.[167, 168, 169] One of the fields, which is yet limited explored,

is the field of nonlinear optical imaging. In this work, we are combining for the first time the results obtained from both second-harmonic generation and two-photon luminescence 2PF imaging for graphene. We report on the results obtained for single layer and bilayer graphene, as well as the difference obtained for pristine and synthetic material.

7.2 Experimental techniques

7.2.1 Sample preparation

Two types of graphene samples are prepared and compared in this work; the exfoliated graphene, produced by micromechanical cleavage of natural graphite and graphene produced by CVD. In both cases, graphene was positioned onto standard 170μm thick microscope coverslips required to fulfill the experimental setup conditions.

7.2.2 Exfoliated graphene samples

The exfoliated graphene samples are obtained after applying the classical scotch tape method,[69] in which a piece of the graphite is thinned with a sharp razor blade. A small part is pealed off by the tape, and is uniformly redistributed over the tape by softly double folding and releasing the tape. (See fig. 7.1) After obtaining a dense graphite film over the tape, the tape is pushed onto the glass substrate and released slowly. By carefully inspecting the sample by means of an optical microscope, the graphene pieces of different thickness are detected. A typical example of an exfoliated graphene sample on a glass slide is shown in fig. 7.1d in which the assignment of the number of layers is done based on the optical contrast difference. This was later on confirmed by Raman spectroscopy. (See section 7.3.)

7.2.3 Transferred CVD graphene samples

The synthetic graphene samples were grown by CVD on copper, and were provided by Prof. Cho (KAIST, Korea) using their standard procedure as reported in [70, 170]. For transferring the graphene from the Cu surface to the glass substrate the following method was used; the $Si/SiO_2/Cu/Graphene$ stack is covered with a thin Poly(methyl methacrylate) (PMMA) film. The Cu/Graphene/PMMA stack is then extracted from the source wafer with the help of a piece of adhesive tape attached to a small corner of the substrate.

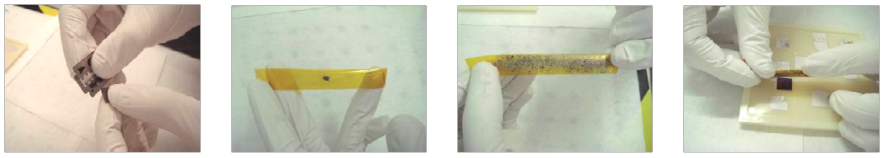

(a) Thinning the graphite by razor blade

(b) Transferring a small graphite piece to tape

(c) Uniformly redistributing the graphite over the tape

(d) Gently transfer the graphite / graphene to substrate

Figure 7.1: Schematic representation of preparation method of graphene exfoliated samples.

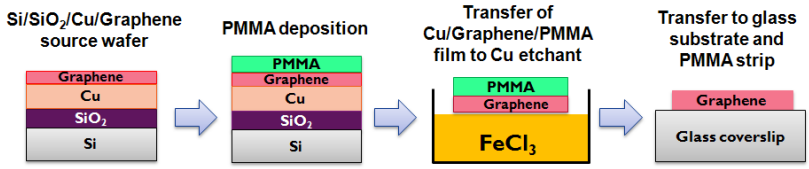

Figure 7.2: Schematic representation of graphene transfer techniques employed in this work.

The as such obtained floating layer of Cu/Graphene/PMMA is transferred to a Cu-etching solution of 0.1M $FeCl_3$ during 15min. After etching, the PMMA/graphene layer is transferred to deionized water for several minutes in order to remove the residual ions (fig. 7.2). The resulting Graphene/PMMA film is transferred onto the glass coverslip and, finally, the PMMA film is removed by putting the sample in acetone (50 °C) during 12h followed by rinsing in isopropyl alcohol (IPA) and N_2 drying step.

7.3 Raman spectroscopy

Raman scattering spectroscopy is a powerful technique in terms of studying graphene properties.[171] Graphene has a very specific and unique Raman fingerprint. It shows a narrow band around 1585cm^{-1}; which is assigned to the stretching modes of the sp^2 C bonds, and is referred to as G band. A second feature is the breathing mode of the sp^2 C bonds and results in a very sharp

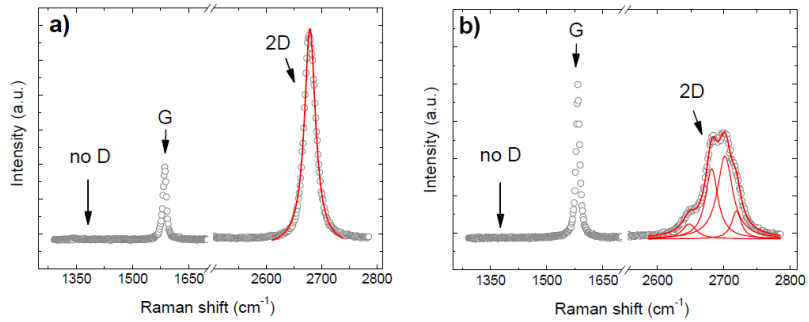

Figure 7.3: Raman spectrum of a typical graphene sample for a) single layer and b) bilayer graphene measured on exfoliated graphene samples.

D and/or 2D band, around 1250 and 2650cm^{-1}, respectively. The 2D band is the second-order of the D band and has a specific shape depending on the number of interacting graphene layers. In case of single layer graphene the 2D band is very sharp, while in case of a bilayer system, the band is broader and can only by fitted to four Lorentzian curves. In a perfect graphene lattice, the D band is absent, while a large intensity is representative for highly defective graphene. The intensity ratio of D to G (ID/IG) is often used as a measure of crystalline quality of graphene, while 2D to G ratio (I2D/IG) is typically above unity for undoped graphene.[172, 173] Raman spectra of graphene films deposited onto the glass substrate were characterized by means of conventional confocal micro-Raman spectrometer (HORIBA Jobin Yvon LabRam 800). The excitation light of 532nm DPSS laser was focused into a spot with a diameter of 0.7µm and safe enough power density of 30kW/cm^2.[174] In fig. 7.3 a typical graphene spectrum is represented for both single and bilayer graphene. One notices immediate the absence of the D peak, proving the good crystalline quality of the graphene sample.

For the transferred CVD graphene samples, both Raman spectroscopy and atomic force microscopy (AFM) images are performed in order to confirm the quality of the graphene layer after transfer. In each sample a sharp and highly intense 2D peak was observed (FWHM $= 38.53 \pm 1.54$cm^{-1}) and confirms the single layer nature of the sample.[171] The presence of weak D-peak suggests low defect density and considerable crystalline quality of the graphene lattice over the whole flake area. Both ratios averaged over several samples are I2D/IG $= 1.77 \pm 0.17$ and ID/IG $= 0.18 \pm 0.05$. Additionally, we analyze the surface of transferred CVD graphene films employed in this work by atomic force microscopy (AFM) (fig. 7.4b). The RMS surface roughness value was found around 0.51nm. Considering all these points, the transferred CVD graphene used

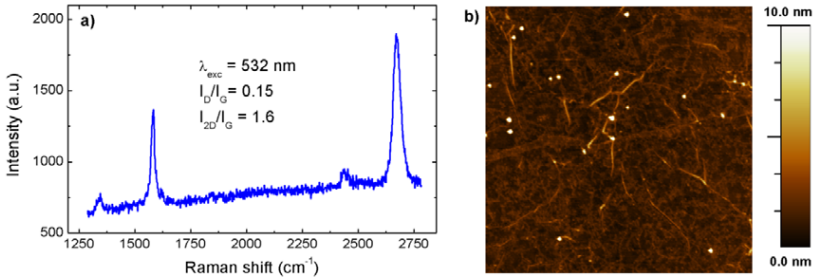

Figure 7.4: a) Typical Raman spectrum of transferred CVD graphene; b) AFM image of the same sample; the image size is $3 \times 3\mu m^2$

in this work is of sufficient quality for usage in nonlinear optical experiments.

7.4 Second-harmonic generation (SHG) and two-photon fluorescence (2PF) Imaging

The SHG and 2PF images are obtained by using a home built set-up in which a high power femtosecond-pulsed laser is coupled to an olympus IX71 microscope. The laser beam of a Ti:sapphire laser (Spectra Physics, Tsunami), emitting at $\lambda_0 = 800$nm is focused by a long distance focusing lens ($f = 7.5$cm), approximating the beam properties of a collimated beam, under normal incidence. The transmitted light is collected by a high power objective and focused onto the built in microscope EM-CCD camera (electron multiplying charge coupled device; Hamamatsu). To discriminate between the SHG and 2PF signals, the appropriate band-pass filters are applied (400nm and $420-650$nm, respectively). In the schematic representation of the set-up (fig. 7.5), the Z-axis corresponds to the normal incidence direction. In the recorded images, the horizontal and vertical direction corresponds to the X and Y- axis, respectively. The recorded polarization patterns are taken over $360\,^\circ$ in steps of $5\,^\circ$, by rotating a halve-wave plate. The complete description of the experimental set-up can be found in [175] . The experimental conditions are similar for all samples.

7.5 Results and Discussion

Initially, we start to record data from the exfoliated graphene samples. From the optical image (See fig. 7.6a), we select a region of interest, which clearly

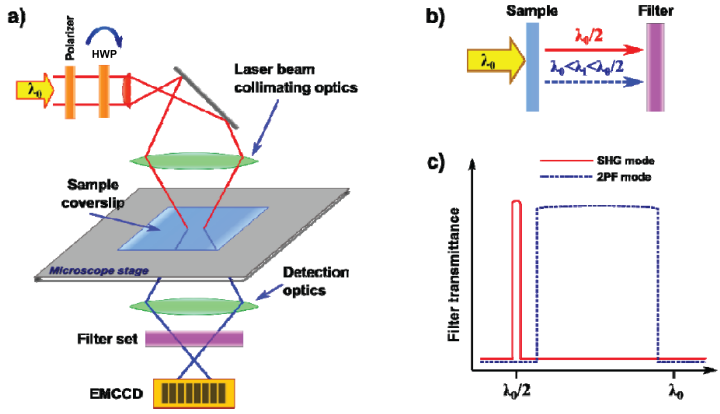

Figure 7.5: Schematic representation of the experimental set-up: a) simplified setup structure; b) a sketch showing difference between two types of experiments (SHG or 2PF modes) depending on the transmittance curve c) of installed filters set.

shows thinner and thicker parts. The thinner regions are assigned to single layer graphene and the more dense part to bilayer graphene. This was confirmed by Raman spectroscopy (fig. 7.6b), where an intensity map of the ratio of 2D and G is plotted. When illuminating the sample with 800nm laser light, and collecting the emitted light in transmission in the optical window ranging from $420 - 650$nm, a clearly distinct intensity response is observed, where the bilayer part is emitting at a higher intensity as compared to the single layer part.

Due to its semi-metallic nature, graphene does not exhibit any photoluminescence response under continuous mode excitation: photoexcited electron-hole pair will immediately recombine nonradiatively (fig. 7.6d, top). In order to make graphene flakes fluorescent, an energy gap has to be introduced like it has been demonstrated for O_2-plasma treated graphene [176] and chemically derived graphene oxide sheets and solutions.[177, 178] However, a periodic ultra short light pulse illumination/excitation pulse will create a non-equilibrium electron-hole plasma in graphene. This effect has been recently employed in graphene-based saturable light absorbers for mode-locking lasers.[179, 180] A high-density electron hole plasma in graphene will also make radiative electron-hole process possible which is responsible for the observed photoluminescence as seen schematically in fig. 7.6(d, bottom).

When assigning a certain pathway on the photoluminescence image (fig. 7.7a), and plotting the intensity of the response as a function of distance on this path

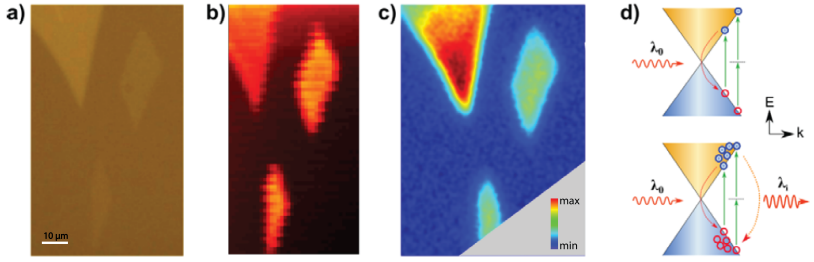

Figure 7.6: a) Optical image of single layer and bilayer graphene flakes; b) Raman image of I2D/IG ratio; c) Photoluminescence image; d) Schematic of single and two-photon absorption followed by e-h pair generation and recombination in graphene for the case of continuous mode excitation (top) and pulsed pumping regime resulting in high-density electron-hole plasma formation (bottom).

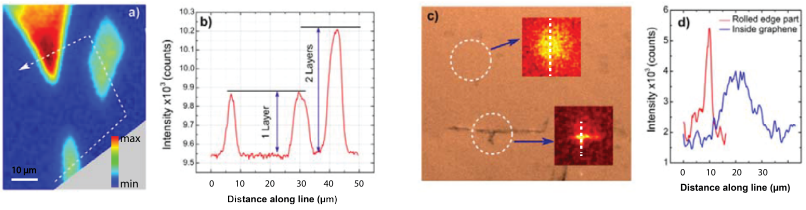

Figure 7.7: a) Photoluminescence image and its profile scan b) shown by white dashed line; c) Optical image of transferred CVD graphene film where insets show 2PF scans in the graphene area and at the rolled edge of graphene film. The top 2PF image shows the gaussian distribution of the fundamental beam with little detail in the 2PF image. In the bottom 2PF image, details of the graphene edge are visible on top of the gaussian beam profile of the fundamental beam. d) Intensity profiles for 2PF signal inside graphene area and at the rolled edge part.

(fig. 7.7b), a stepwise profile is observed. The steps observed, are consistent with the assignment of the single and bilayer graphene. This is consistent with data reported in the literature by Liu *et al.*[81] and Stohr *et al.*[75]; although reflection geometry is used in their experiments. In both reports, they demonstrate the simple additivity of the emission signals dependent on the number of layers. This allows us to quickly map a graphene sample in terms of the presence of the number of layers.

When applying the same procedure to a CVD transferred graphene sample (fig. 7.7c), a uniform illumination image is observed on the smooth single layer

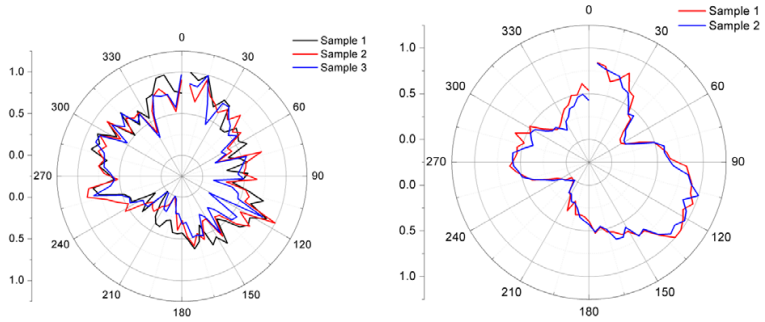

(a) SHG intensity as a function of input polarization: Single layer graphene

(b) SHG intensity as a function of input polarization : bilayer graphene

Figure 7.8: Polarization pattern of single and bilayer graphene.

sample part, while focusing on a mechanical folded graphene edge region, a more intense signal is observed (fig. 7.7d). Although, further experiments should be performed to fully understand the spectroscopic response of both types of graphene sources.

In a second experiment, we change the filter settings of the imaging microscope to the SHG mode. Note that, opposed to previous literature reports,[77] we collect any SHG effect in the perpendicular input direction. Figure 7.8 shows the plot of the SHG response as a function of input polarization of the fundamental light. For the single layer graphene no clear polarization dependence is observed, while for the bilayer graphene sample, a 3-fold symmetry pattern is observed. Opposed to what is observed by Van Driel *et al.* in [77], a different polarization pattern is observed. However, one has to be careful to do a direct comparison since the data are collected in different experimental geometry. However, for the bilayer graphene, the same symmetry pattern is observed. In case of single layer graphene, a different polarization pattern is observed. Additional to a difference in measurement conditions, also different substrates are used, which have an influence on the SHG response.

Opposite to the observation of photoluminescence in the $420 - 620$nm region, no SHG signal is observed for the CVD transferred samples in the same experimental conditions as the exfoliated samples. It can be assumed/argued that this absence of SHG signal originates in C_3-symmetry breaking of the carbon lattice due to the presence of defects and grain boundaries in the crystalline lattice of CVD graphene. Therefore, SHG intensity imaging can be employed as a fast defect mapping technique providing significantly better

throughput than Raman scattering spectroscopy imaging.

7.6 Conclusions

We have performed an analysis of pristine graphene samples and compared the outcome with the response of CVD transferred graphene. In both type of samples, similar emission intensity is observed from single to bilayer/multilayers regions. We benchmark transferred CVD graphene towards exfoliated graphene by 2PF microscopy for the first time. On the other hand, for the second-harmonic signals, no effect is observed for CVD transferred graphene, while a different polarization pattern is observed for pristine samples. However, this work is not yet totally conclusive and more experiments will be required to fully understand the ongoing processes.

Acknowledgments

We would like to acknowledge Prof B.J. Cho from KAIST, Korea, for providing us with CVD grown graphene. MvdV thanks the Fund for Scientific Research-Flanders (FWO-V) for a post-doctoral fellowship.

Chapter 8

Fast Fourier-transform Second-harmonic generation provides a solution for measuring nonlinear effects on fragile structures

It was observed during multi-photon and high-harmonic generation experiments, presented in chapter 7, that graphene degraded dramatically under the influence of femto-second pulses. Hence, the characterization of graphene by means of SHG proved to be tedious, since the SH signal degraded as well. Therefore, a novel detection method for the second-harmonic signal was developed based on the continuous rotation of the polarization and a fluorescence-lifetime imaging microscopy (FLIM) detection system. We demonstrated that fast Fourier-transform Second-harmonic generation (FFT-SHG) is an interesting technique for the study of fragile structures.

Drs. Rik Paesen from the UHasselt provided the elaboration on the detection of SHG using fast Fourier transformation to characterize fragile structures. We validated the technique using structures provided by dr. Inge Asselberghs and drs. Pieter-Jan Valvekens. I submitted our work as a proceedings of OSA and presented our conclusions on FiO 2013 in Orlando, USA.

M. K. Vanbel, R. Paesen, W. Brullot, S. Vandendriessche, I. Asselberghs, K. Markey, P. Valvekens, M. A. van der Veen, D. De Vos, M. Ameloot, V. K. Valev, J.-P. Locquet, T. Verbiest,
Fast Fourier-transform second-harmonic generation (FFT-SHG) provides a solution for measuring nonlinear effects on fragile structures,
Frontiers in Optics, **3**, 2013, FTu2F.5.

The information on the detection system in the publication should be extended with the filter information. A band pass filter (405 ± 5nm) in front of the detector was used to remove the fundamental beam from the outgoing beam.

Abstract

The intense laser power required to measure nonlinear effects can damage the structures upon measuring. We demonstrate that fast Fourier-transform Second-harmonic generation (FFT-SHG) technique provides an elegant solution to obtain polarization patterns of degrading structures.

8.1 Introduction

Nonlinear optics is a broad research area with diverse research facets. Since the development of second-harmonic generation (SHG), which is a second-order nonlinear effect, the technique has been used to study structures in centrosymmetric materials by probing surface and interface specific properties such as adsorption of polymer films,[13] chirality in polymer films,[148] chirality in metamaterials,[181] passivation of semiconductors,[16] and diffusion of molecules into porous materials.[17, 18] Besides the surface and interface properties, the crystal structure of a material can be obtained by analyzing the SHG polarization pattern which is typically measured by rotation of the polarization of the fundamental light and SHG detection through an analyzer.[99] One advantage of using SHG to probe the material crystal structure is that the SHG process itself does not require absorption of the photons to induce a real excited state.[99] The excited state is rather a virtual state where no energy transfer due to the incident photons occurs. Therefore, little damage is induced by the SHG experiment providing the possibility to probe fragile structures. However, when absorption at the fundamental frequency does occur, the SHG signal is enhanced due to resonance effects. A major drawback is that energy transfer is possible and heating of the structure is inevitable. This causes oxidation and breaking of bonds, resulting in structure degradation and ultimately leads to a drastic change in SHG response. Indeed, a full SHG characterization is usually done by recording the SH-intensity vs. input polarization for all SHG polarization components, leading to so called polarization curves. These polarization curves can be used to determine the symmetry of the sample. Since such measurements take a significant amount of time, degradation of the sample poses a serious problem. In analyzing the SHG polarization pattern, taking the damage induced intensity decay into account can be difficult since little is known on the degradation process. However, including the unknown decay component can be circumvented by performing a fast Fourier transform (FFT) to get information on only the different harmonic contributions, and by that the symmetry of a structure. An additional advantage of performing an FFT is that low signal to noise (SNR) data can still be used to obtain the required information. Therefore low signal to noise (SNR) and fast

measurements allow us to obtain sufficient data point before sample degradation becomes problematic. Finally, upon measuring the SHG response of structures by pointing a laser beam on the sample surface, a spatial average of the SHG response is detected. Any inhomogeneity in the sample cannot be probed separately and causes fluctuations in the SHG response when different areas of the same structure are probed. This problem can be overcome by combining the second-harmonic generation method with a microscope, in which only a limited area of the sample can contribute to the total signal. In this paper, we introduce microscope aided fast Fourier-transform Second-harmonic generation (FFT-SHG) analysis of chemical vapor deposited graphene, which has serious degradation issues, to obtain a polarization pattern of the structure. Moreover, the validity of the technique was confirmed with the metal-organic-framework (MOF) [$Ba_2TMA(NO_3)(DMF)$]. By obtaining a polarization pattern by means of fast Fourier-transform Second-harmonic generation (FFT-SHG), the issues with degradation of the graphene are resolved.

8.2 Theory and experimental methods

In general, the SHG polarization response can be written as

$$I(t) = \frac{a_0}{2} + a_1 sin(\omega_0 t) + a_2 sin(2\omega_0 t) + a_3 sin(3\omega_0 t) + a_4 sin(4\omega_0 t) + \cdots \quad (8.1)$$

where a_i represents the amplitude of the i^{th}-harmonic in the FFT-SHG spectrum, and ω_0 is the polarization modulation frequency set at 0.899rad/s. A possible phase shift is not taken into account since this does not contribute to the determination of the crystal structure. The FFT-SHG measurements were carried out on a commercial Zeiss multi-photon microscope consisting of a LSM510 mounted on an Axiovert 200M. The detection occurs in non-descanned (ND) mode using a photon counting detector (Hamamatsu H7422P-40). The photon counting detector is controlled using a Becker & Hickl SPC830 FLIM system. The fundamental wavelength was set to 810nm on the Mai Tai Deep See Laser (Spectra Physics) with a mean output power of 5mW. The polarization direction of the 810nm fundamental beam is continuously rotated using an in house developed stepper motor controlled half wave plate which is contained in a slider and positioned directly under the microscope objective. The images are recorded with a 10× objective (NA of 0.3) and a pixel dwell time of 6.4µs. A time series frame scanning is performed on a uniform region with a size of at least a few point spread functions (white rectangle fig. 8.1a), which in addition to the FFT-SHG technique also slows sample deterioration. Every time frame is averaged into a single data point resulting in a time dependent SHG signal

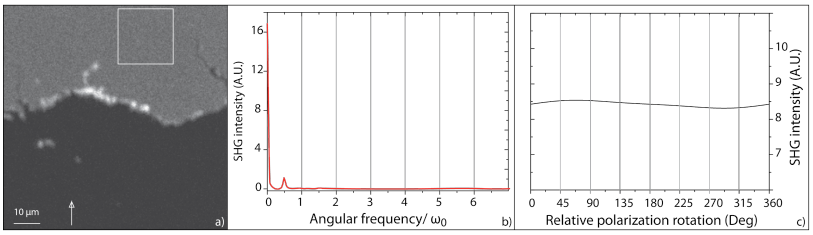

Figure 8.1: Polarization pattern determination of graphene. The location of the graphene layer was determined by second-harmonic generation microscopy (shown in a)). The arrow indicates the polarization direction of the fundamental beam before passing through the system for this figure. The highlighted white square is the region where the FFT-SHG measurements were performed. In b), the FFT-SHG spectrum of graphene is shown, displaying the possible harmonic contributions. From the FFT-SHG spectrum, the inverse polarization pattern with relative angle is calculated (shown in c)). All the parameters, but the frequency at $1/2\omega_0$ were taken into account. This result is in agreement with the C_∞ symmetry of graphene.

on which the FFT analysis is performed using Matlab's (The Mathworks) built in FFT function.

8.3 Sample description

A sheet of single layer CVD graphene is transferred from a Cu foil to a glass substrate by using classical transfer techniques.[70, 170] Prior to graphene deposition, these glass slides are modified with location markers using standard photolithography. [Ba2TMA(NO3)(DMF)] (Ba MOF) was formed by combining $Ba(NO_3)_2$, H_3TMA and DMF at 423K. Details on the synthesis can be found elsewhere.[182] Foo *et al.* reported that the structure has a threefold rotation axis parallel to its c axis and a twofold rotation axis parallel to its b axis.[182] The crystals form colorless needles with their b axis mostly parallel to the substrate surface.

8.4 Discussion and results

The graphene flake is located using SHG microscopy. After illumination, the structure exhibited a lower SHG response as compared to the first image

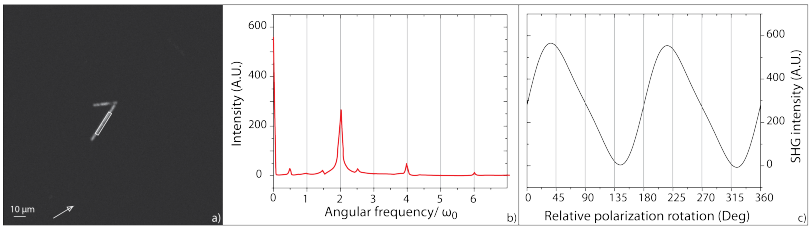

Figure 8.2: Polarization pattern determination of a Ba MOF needle. The location of the Ba MOF was determined by second-harmonic generation microscopy (shown in a)). The arrow indicates the polarization direction before passing through the system for this figure. In b), the FFT-SHG spectrum is shown. The peaks in this spectrum determine the amplitude of the modulation at their respective frequencies. From this, the polarization pattern of the Ba MOF is reconstructed, which is shown in c). All the parameters, but the frequency at $1/2\omega_0$ were taken into account.

revealing the problem of degradation of graphene samples. Therefore the proposed alternative FFT-SHG method is used to obtain a polarization pattern, and hence the symmetry of the sample. The area on which the FFT-SHG measurements were performed, are indicated with a white square (fig. 8.1a). In the FFT-SHG spectrum of graphene (fig. 8.1b), a large peak at 0Hz can be observed and a small peak at $1/2\omega_0$. According to eq. (8.1), the first peak corresponds to the isotropic contribution of the SHG signal, which is frequency independent. The second peak occurs at the half of the polarization frequency, which is not expected to be present in the SHG polarization pattern. This peak is an artefact associated with the effective rotation speed of the half-wave plate. The polarization pattern can be calculated and is shown in fig. 8.1c. For this, all frequencies except $1/2\omega_0$ are taken into account. It can be seen that there are no features in the polarization pattern, which is expected for a hexagonal structure symmetry of the graphene sample.[167]

The Ba MOF needles were analyzed in a similar manner as the graphene layer. This Ba MOF exhibits a constant SHG response under illumination. The structure is shown in fig. 8.2a. A two fold symmetry is expected for this structure, since it has a two fold rotation axis and two symmetry planes in the structure. Two main peaks were observed in the FFT-SHG spectrum (fig. 8.2b), one at zero frequency and one at the double frequency. The extracted polarization pattern is shown in fig. 8.2c. The obtained polarization pattern is compatible with the two-fold symmetry of the sample.

8.5 Conclusion

We demonstrated that fast Fourier-transform Second-harmonic generation (FFT-SHG) is an interesting technique for the study of fragile structures. SHG-polarization patterns can be obtained in a straightforward way, without problems with degradation of the sample.

Acknowledgments

This work was supported by the KU Leuven (GOA). We acknowledge the graphene sample preparation of Prof. B. J. Cho of KAIST Korea, Alexander Klekachev of imec and Frederik Drieskens. M.K.V. is grateful for the scientific discussions with M. Bloemen.

Chapter 9

Conclusions

Since the 80's and 90's, second-harmonic generation (SHG) and electric field-induced second-harmonic generation (EFISH) have been used to characterize the industrially relevant Si/SiO_2 interface.[95, 58] Many interface specific problems were investigated and insights were gained on the interface specific properties and the electrical properties of the metal-oxide-semiconductor (MOS) structure. Up to the late 90's, the main semiconducting material was Si. Making use of its native oxide, the quality of the Si/SiO_2 interface determines the transistor's performance. Due to previous research on the Si/SiO_2 interface by SHG, the knowledge obtained by this research was very useful to semiconductor processing for a long time.

Until the nineties, the performance of transistor devices was enhanced by scaling down the dimension of silicon based transistors. As their dimensions decreased, the fundamental limits of Si were reached, which resulted in high leakage currents or device failure over time. Therefore, alternative materials were needed to replace specific part of the Si based transistor. Hence, in different semiconductor processing steps, different materials have been introduced to keep on scaling down the dimensions and improving the device performance. When introducing new materials, different interfaces arise, which needed to be characterized, since their properties, among other, determine the electronic properties of the MOS stack. By using theoretical models of SHG and EFISH reported in literature,[23, 29] several issues could be exposed in these novel MOS stacks by means of nonlinear techniques. Moreover, certain effects on the interface or electrical properties of the MOS stack could be characterized by SHG and EFISH.

In this thesis, we demonstrated that SHG can be used as excellent interface characterization tool in semiconductor processing, with potential in-line characterization properties for interface quality control. Due to its high sensitivity for surface and interface properties, SHG gives valuable insight on layered MOS gate stacks. An example of a novel MOS gate stacks is the silicon-cap passivated Ge. SHG measurements on this type of structure revealed that the oxidizing agent used to form the native oxide influences the interface and oxidation depth. We used SHG to determine and monitor the influence of the oxidation process prior to the atomic layer deposition (ALD) process of the high-k dielectric layer. Moreover, for a silicon cap passivation, SHG provided a highly accurate relative measurement of the thickness of the Si layer of only a few monolayers thickness. In absence of surface roughness, SHG distinguished between different oxide treatments during semiconductor growth, in contrast to spectroscopic ellipsometry. A subtle difference in oxidizing behavior of the Si layer during oxidizing cleaning steps was observed, as function of Si precursor.

The interface quality of these silicon-cap passivated Ge substrates was investigated, which is shown in chapter 3. The interface quality was best when using N_2 rather than H_2 during the silicon-cap growth and at higher processing temperature. Under these growth conditions, the smoothest and best defined interface was obtained. This again illustrates the usefulness of SHG as characterization tool for dielectric/semiconductor interfaces.

SHG as characterization tool was further elaborated on in chapter 4. We exploited the capability of SHG to characterize buried interfaces of sulphur passivated Si substrates. Thereafter, Al_2O_3 was deposited using an atomic layer deposition (ALD) reactor. We showed different SHG intensities for oxide passivated Si substrates growth with H_2O and O_3 as oxidizing agents. Due to the difference in oxidizing agent, a different interface was obtained. Depending on the number of cycles in the ALD process, a different constitution of the interface is observed. Moreover, only the oxide-semiconductor interface and the bulk-contribution of Si primarily determine the SHG response, while no second-harmonic (SH) signal arises from the oxide layer.

Until now, the investigated structures did not represent a MOS structure in operation in a semiconductor device. Therefore, an external electric field has to be applied to investigate the charge migration. By using electric field-induced second-harmonic generation (EFISH), nonlinear optics can be used to probe the electrical properties of the MOS structure. A top gate was discarded due to the use of a corona charging wire in air as top electrode. By doing so, no SHG contribution of the electrode had to be accounted for. In chapter 5, we elaborated on the charge migration in an Al_2O_3 covered n-doped Si substrate. Tunneling of holes from Si into the oxide layer was observed when a negative corona field was applied to the structure. The tunneled charge remained in the

oxide after the charging experiment, which was confirmed by capacitance-voltage (CV) measurements.

The principle of charge migration in MOS structures was further investigated in another promising high-k dielectric material, namely MgO, which is shown in chapter 6. We illustrate that the electrical properties of a MOS stack are influenced by the sequence of the growth method of the interface and top layer. By using EFISH, a difference in the first monolayer of MgO deposition caused by altering the growth sequence of the molecular beam epitaxy could be identified. Moreover, when an external positive electrical field was applied, the charge migration which was observed could be identified as migrating oxygen vacancies. Depending on the first monolayer, the electrical properties were different during the whole experiment and not only in the initial stage of the measurements.

Since graphene is a promising novel channel material in a metal-oxide-semiconductor field-effect transistor (MOSFET),[43] our attention was drawn to its characterization by means of nonlinear optical methods. However, due to the small size of pristine graphene, this research has been conducted by using a multi-photon scanning and wide-field microscope, while the previous research was conducted on an optical setup where the spatial dependency of the SH signal was not probed. We elaborated on this in chapter 7, where we illustrated that both chemical vapor deposition (CVD) transferred and pristine graphene can be visualized by SHG and two-photon fluorescence (2PF). It was observed that graphene degraded dramatically under the influence of femto-second pulses. Following from the experience in imaging graphene, a novel detection method for SHG based on fast Fourier transformation is presented in chapter 8.

In conclusion, we have shown that SHG is capable of characterizing interfaces in semiconductor devices in a technological setting. Due to the gained insights of this research, future transistor devices can have improved interface quality as well as their electronic characteristics. It was shown that SHG is a versatile characterization method, sensitive to both electrical as well as interface properties of an MOS gate stack. More fundamental research is required to investigate if other parameters influence the quality of interfaces and its associated electrical properties. This can be performed *ex-situ*, in order to verify the correlations of the second-harmonic signal with the physical parameters. In order to assess SHG as a in-line characterization technique in a quantitative manner, a reference structure, with similar doping levels, passivation methods etc. has to be fully characterized. When calibrated and assigned to a specific manufacturing step, SHG can be used as in-line characterization tool where it can monitor the interface quality or doping level over time of the processed structures. This has been done in this research for different case studies. We demonstrated the characterization of a Ge channel-based transistors and for different high-k dielectric layers on top of Si. Using SHG as characterization

technique in upcoming device nodes of the same types of transistors is possible. Continued down-scaling of the transistor dimensions can increase the necessity of incorporating SHG as interface or surface characterization tool. Moreover, the technique is also a potential characterization tool for other types of materials, proposed in the ITRS roadmap. It is important to note that the spatial resolution of SHG is limited. When applying the technique to a fully processed wafer, the observed second-harmonic signal would be a spatial average of all structures within the focal point, since the focal point is larger compared to the feature size of the transistor structures. In order to obtain information from SHG measurements on semiconductor devices, a blanket wafer, i.e. where no spatial feature are present, is preferred. Then, correlating the SH signal to the physical parameters is more straight forward. However, when second-harmonic generation is used as processing control, information on the quality of the structures can still be obtained through the spatial average of the SH response. The resolution of the technique can be further improved by employing a nonlinear optical microscope to measure the nonlinear optical signals.

Outlook

As presented here, characterization by second-harmonic generation (SHG) and electric field-induced second-harmonic generation (EFISH) can yield important information on the interface properties and electrical properties of semiconductors and MOS structures.

In the front-end-of-line processing, which refers to the transistor optimization and fabrication, it is shown that SHG can give valuable insights. We demonstrated this on Si and Ge substrates. However, characterization of semiconductor interfaces by means of nonlinear optical techniques is not limited to these materials. Nevertheless, centrosymmetric bulk materials are more suited for this type of characterization than noncentrosymmetric bulk materials. In the latter case, the separation of bulk and interface response becomes challenging, since a large bulk response is expected. A noncentrosymmetric bulk material which is proposed in the ITRS roadmap as next generation semiconductor material is III-V compound semiconductors such as GaAs. Additional insight in needed on the deposition of III-V compound semiconductors on a Si substrate and its related interface properties. Still, there is a prospect for SHG as characterization tool on Si or Ge based substrates. In order to characterize the bulk of centrosymmetric semiconductors, it is possible to extend the presented research to other nonlinear optical effects, such as third-harmonic generation. For this specific nonlinear optical effect, the surface and interface specificity of the technique is no longer applied, hereby allowing to probe bulk properties as well. Combining both second- and third-harmonic generation can yield valuable

information for bulk and surface specific properties. As is shown in this thesis for SHG, the electric field-induced variant of these nonlinear optical techniques can be utilized to increase the insight in MOS structures as well as demonstrating the usefulness of nonlinear optical techniques in a technological setting.

In order to increase the spatial resolution of the SHG technique, incorporation into a microscope body is possible. Integrating SHG in a microscopy setup, enables a different approach to interface characterization. Inhomogeneous structures or gradient in structures can be visualized. It is expected that different areas of the processed wafer, due to the difference in layer sequence, will yield a different second-harmonic intensities, since their interface properties will be different. Probing the channel in such a manner, will be difficult, since the channel size is well below the diffraction limit. However, characterization of larger areas might still be possible. Visualizing the charge migration when an external field is applied to a MOS structure, while applying a source-drain current in the channel of a MOSFET could give visual insight in the electrical properties of the channel during device operation. However, an spatial average second-harmonic signal is expected, so initially large structures are required. Still, information can be gained on smaller feature sizes as well. The SH signal from the large source and drain areas can be separately investigated and subsequently subtracted from the average signal of the source-channel-drain featured wafer. It is more convenient to perform this research in a macroscopic setup rather than a microscopic setup.

The difference in SHG intensity observed when a different number of ALD cycles were performed can be connected to the interface structure and their interface quality. In this type of research, other techniques have to be employed in order to correlate the SHG signal to changes at the interface, since its constitution changes as function of ALD cycle. However, the second-harmonic signal clearly suggest that the interface in changing. Additional research is needed for clarification.

Not only in front-end-of-line processing, SHG can be a valuable asset. In the back-end-of-line, where the interconnects are manufactured, SHG could have a significant contribution in optimizing the processing steps associated with interconnecting transistors and deposition methods of the interconnects on the source, drain or gate areas. Since these interconnects are of comparable size as the detection limit in a microscope, fundamental knowledge can be gained on top of the monitoring properties of SHG in an industrial setting.

The presented research results can be extended to other type of electronic devices besides MOS structures. The knowledge obtained on MOS devices can easily be extended to inorganic light emitting diodes (LEDs). Since SHG is a very versatile characterization tool, organic light emitting diodes form

an excellent test subject for SHG measurements. Also in this type of device, SHG and EFISH can yield important information on interface and electrical properties. Similarly, solar cells are an analogue model device to MOS and LEDs which consist of a lot of layers and hence interfaces.

Liquid crystal displays, in addition to their abundantly present interfaces and electrical contacts, consist of molecules which can align in a certain direction, which makes this model device extremely interesting for nonlinear optical technique characterization. The change in direction, when a potential is applied, can be observed by second-harmonic generation. Hence, SHG combines the information of the interface, electrical and alignment properties.

As it is shown here, SHG and EFISH could continue its contribution to semiconductor industry as in-line and *ex-situ* characterization tool for electronic devices.

Health, safety and environment (HSE) protocols

In the chemical laboratories at the KU Leuven and more specifically in our lab molecular imaging and photonics, strict rules are imposed by the office of health, safety and environment (HSE). Its goal is to minimize the risk of injury or illness by providing protocols, training, information and feedback on your personal work and equipment. Our lab and the VGM department followed a mutual learning curve to ensure the correct transfer of information about optical setups and its practical application. Laser safety was a major issue in this learning process. Due to the abundance of class 3B and 4 pulsed lasers used in my thesis, the correct laser goggles were purchased. Moreover, when constructing an optical setup, (back)reflections and points of scattering were accounted for and blocked appropriately, since these pulsed laser systems can cause sever eye injury if your eye is exposed to the beam. Also skin burn can occur if one is exposed to the beam for an extended period of time. One should be careful with combustible materials, since they may present a fire risk. Prior to working with a laser system, a certificate is needed. Jozef Leenknecht of Spectra Physics gave a laser training session, from which I received my laser safety form.

In some of the research presented in this thesis, silane (SiH_4) and trisilane Si_3H_8 were used to grown a silicon capping layer on Ge in an ALD deposition tool. These compounds are extremely flammable and if mixed with air, they can lead to explosions. Inhalation, skin and eye contact should be avoided. Their risk-class is E4 with approved release.

Appendix A

Calculating the tensor components of a second-order susceptibility tensor within the electric dipole approximation.

The principle of calculating the tensor components of the second-order susceptibility tensor can be explained on an intuitive manner, as was presented in chapter 1. However, here we will be using the method of "direct inspection" of the indices. It was shown by Fumi *et al.*[183] that symmetry transformation of a tensor component can be acpressed as the product of their respective coordinates. The condensed formulation of second-harmonic generation (SHG) will be used.

$$P_i^{(2)} = \chi_{ijk}^{(2)} \cdot E_j E_k \tag{A.1}$$

We conduct single beam experiments, which implies that both electric field components should have the same index, since they propagate in the same manner. This property results in

$$\chi_{ijk}^{(2)} = \chi_{ikj}^{(2)} \tag{A.2}$$

where the index i represents the direction of the induced polarization and j and k are direction of the incident electric fields. Since the physical properties of a system remain invariant under symmetry operations, the calculated tensors should be equal before and after the symmetry operation. This will be tested for several common point groups.

A.1 $C_{\infty v}$ or C_{4v} point group symmetry

The specific symmetry $C_{\infty v}$ is in plane isotropic. The specific symmetry elements that need to be considered are:

- an infinite number of mirror planes perpendicular to the surface, but, for our purpose, it is sufficient to consider only the mirror plane in the YZ and XZ plane,
- an infinite rotation axis which, for our purpose, is equivalent to a C_4 rotation axis,

Since we use a C_4 rotation axis to simplify the infinite rotation axis perpendicular to the surface, the symmetry consideration of the $C_{\infty v}$ symmetry group as the same as for a C_{4v} symmetry group. A graphical illustration of the $C_{\infty v}$ symmetry group is presented in fig. A.1

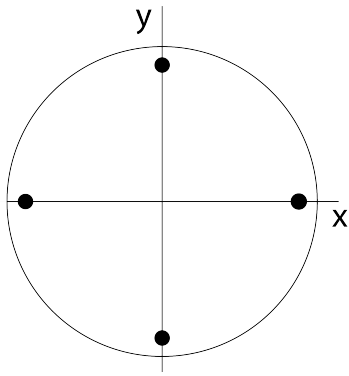

Figure A.1: Illustration of a $C_{\infty v}$ symmetry group

Evaluating all these symmetry conditions will result in a simplification of the second-order nonlinear susceptibility tensor.

A.1.1 Mirror planes

The mirror plane m_{yz} changes +x to -x while m_{zx} transforms +y to -y. When using these mirror plane operations, simplifications can be made to the susceptibility tensor, represented in eq. (A.3)

$$\begin{bmatrix} \chi^{(2)}_{xxx} & \chi^{(2)}_{xyy} & \chi^{(2)}_{xzz} & \chi^{(2)}_{xyz} & \chi^{(2)}_{xxz} & \chi^{(2)}_{xyx} \\ \chi^{(2)}_{yxx} & \chi^{(2)}_{yyy} & \chi^{(2)}_{yzz} & \chi^{(2)}_{yyz} & \chi^{(2)}_{yxz} & \chi^{(2)}_{yyx} \\ \chi^{(2)}_{zxx} & \chi^{(2)}_{zyy} & \chi^{(2)}_{zzz} & \chi^{(2)}_{zyz} & \chi^{(2)}_{zxz} & \chi^{(2)}_{zyx} \end{bmatrix} \tag{A.3}$$

For example, when considering the xz mirror plane, the sign of y changes to -y, modifying the polarization in that direction from P_y to $-P_y$ too, as well as the electrical component E_y to $-E_y$. As a consequence: $P^{(2)}_y = \chi^{(2)}_{yyy} E_y E_y$ transforms into $-P^{(2)}_y = \chi^{(2)}_{yyy} E_y E_y$. Since physical properties cannot change under symmetry operations, this necessarily means that $\chi^{(2)}_{yyy} = 0$. In a similar way, one can determine all other non vanishing components. We will use the method of "direct inspection". Performing the symmetry consideration on the indices of the second-order susceptibility tensor is equivalent to the extensive method used above.

The vanishing tensor components will be systematically deduced from the symmetry properties of the material. Firstly, the 2 different mirror planes will be taken into account.

Consider the first row in the susceptibility tensor and apply the m_{yx}, which means changing the sign of x. Using the "direct inspection" method

If $x \to -x$, then the tensor components of the first row of eq. (A.3) yield

$$xxx \to -xxx \Rightarrow \chi^{(2)}_{xxx} = 0 \tag{A.4}$$

$$xyy \to -xyy \Rightarrow \chi^{(2)}_{xyy} = 0 \tag{A.5}$$

$$xzz \to -xzz \Rightarrow \chi^{(2)}_{xzz} = 0 \tag{A.6}$$

$$xyz \to -xyz \Rightarrow \chi^{(2)}_{xyz} = 0 \tag{A.7}$$

$$xxz \to -(-xxz) \Rightarrow \chi^{(2)}_{xxz} \neq 0 \tag{A.8}$$

$$xyx \to xyx \Rightarrow \chi^{(2)}_{xyx} \neq 0 \tag{A.9}$$

However, the the tensor component from eq. (A.9) has to be examined more closely.

If $y \to -y$, then

$$xyx \to -xyx \Rightarrow \chi^{(2)}_{xyx} = 0$$

For the second row of eq. (A.3), the m_{zx} is considered. If $y \to -y$, then

$$yxx \to -yxx \Rightarrow \chi^{(2)}_{yxx} = 0$$

$$yyy \to -yyy \Rightarrow \chi^{(2)}_{yyy} = 0$$

$$yzz \to -yzz \Rightarrow \chi^{(2)}_{yzz} = 0$$

$$yyz \to -(-yyz) \Rightarrow \chi^{(2)}_{yyz} \neq 0$$

$$yxz \to -yxz \Rightarrow \chi^{(2)}_{yxz} = 0$$

$$yyx \to -(-yyx) \Rightarrow \chi^{(2)}_{yyx} \neq 0$$

Again, for the last tensor component, when performing the m_{yx} mirror symmetry, $x \to -x$ and $\chi^{(2)}_{yyx} = 0$.

For the final row of eq. (A.3), the symmetry operations are both considered and yield

$$zxx \rightarrow -(-zxx) \Rightarrow \chi^{(2)}_{zxx} \neq 0$$

$$zyy \rightarrow -(-zyy) \Rightarrow \chi^{(2)}_{zyy} \neq 0$$

$$zzz \rightarrow zzz \Rightarrow \chi^{(2)}_{zzz} \neq 0$$

$$zyz \rightarrow -zyz \Rightarrow \chi^{(2)}_{zyz} = 0$$

$$zxz \rightarrow -zxz \Rightarrow \chi^{(2)}_{zxz} = 0$$

$$zyx \rightarrow -zyx \Rightarrow \chi^{(2)}_{zyx} = 0$$

Combining these findings, eq. (A.3) becomes

$$\begin{bmatrix} 0 & 0 & 0 & 0 & \chi^{(2)}_{xxz} & 0 \\ 0 & 0 & 0 & \chi^{(2)}_{yyz} & 0 & 0 \\ \chi^{(2)}_{zxx} & \chi^{(2)}_{zyy} & \chi^{(2)}_{zzz} & 0 & 0 & 0 \end{bmatrix} \tag{A.10}$$

A.1.2 Fourfold rotation axis

The fourfold rotation axis is oriented perpendicular to the surface normal, in the z-direction. This fourfold symmetry means that upon rotation of the structure by 90 degrees, the tensor components do not change. Considering the $C_{\infty v}$ symmetry group represented in fig. A.1 and imagine a rotation of 90 degrees anticlockwise. The spatial coordinates will change as follows:

$$x \rightarrow y \quad \text{and} \quad y \rightarrow -x \tag{A.11}$$

Using these properties and the "direct observation" method on the tensor component $\chi^{(2)}_{xxx}$

$$xxx \rightarrow yyy \rightarrow -x - x - x \rightarrow -xxx \Rightarrow \chi^{(2)}_{xxx} = 0 \tag{A.12}$$

Now we use these symmetry operations on the simplified susceptibility tensor, since it is sufficient for a tensor component to be zero in one of the symmetry operation to be nonexistent in the material. In other words, one component is

not necessarily zero for one symmetry operation, but it might be for another symmetry operation for the same symmetry group. Starting from eq. (A.10),

$$xxz \rightarrow yyz \rightarrow -x-xz \rightarrow xxz \Rightarrow \chi^{(2)}_{xzx} \neq 0 \tag{A.13}$$

$$yyz \rightarrow -x-xz \rightarrow -y-yz \rightarrow yzy \Rightarrow \chi^{(2)}_{yyz} \neq 0 \tag{A.14}$$

$$zxx \rightarrow zyy \rightarrow z-x-x \rightarrow zxx \Rightarrow \chi^{(2)}_{zxx} \neq 0 \tag{A.15}$$

$$zyy \rightarrow z-x-x \rightarrow z-y-y \rightarrow zyy \Rightarrow \chi^{(2)}_{zyy} \neq 0 \tag{A.16}$$

$$zzz \rightarrow zzz \Rightarrow \chi^{(2)}_{zzz} \neq 0 \tag{A.17}$$

Following from these results, all tensor components in the simplified susceptibility tensor after performing the mirror symmetry operations remain. However, additional simplifications can be made, based on the fourfold rotation symmetry. From eqs. (A.13) and (A.14) it can be noticed that $\chi^{(2)}_{xzx} = \chi^{(2)}_{yzy}$, while from eqs. (A.15) and (A.16) $\chi^{(2)}_{zxx} = \chi^{(2)}_{zyy}$. Thus the total second-order susceptibility tensor reduces to

$$\begin{bmatrix} 0 & 0 & 0 & 0 & \chi^{(2)}_{xxz} & 0 \\ 0 & 0 & 0 & \chi^{(2)}_{xzx} & 0 & 0 \\ \chi^{(2)}_{zxx} & \chi^{(2)}_{zxx} & \chi^{(2)}_{zzz} & 0 & 0 & 0 \end{bmatrix} \tag{A.18}$$

A.2 C_{3v} point group symmetry

The point group C_{3v} has a threefold symmetric surface along the surface normal. The specific symmetry elements that need to be considered are:

- a threefold rotation axis perpendicular to the surface
- three mirror planes in the xz plane, and $\pm$ 120 degrees relative to this one

A graphical illustration of the C_{3v} symmetry group is presented in fig. A.2

Evaluating all these symmetry conditions will result in a simplification of the second-order nonlinear susceptibility tensor.

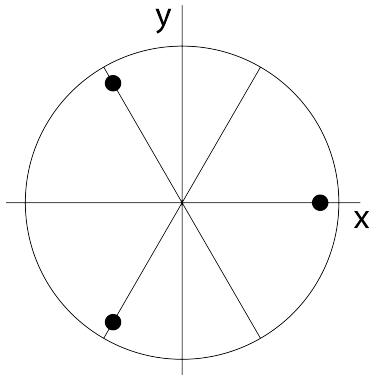

Figure A.2: Illustration of a C_{3v} symmetry group

A.2.1 Threefold rotation axis

Again using the method of "direct observation" the second-order susceptibility tensor can be evaluated and simplified. When the threefold symmetry operation is performed, the coordinates change as follows

$$x \rightarrow -\frac{1}{2}x - \frac{\sqrt{3}}{2}y \rightarrow -\frac{1}{2}x + \frac{\sqrt{3}}{2}y \tag{A.19}$$

$$y \rightarrow \frac{\sqrt{3}}{2}x - \frac{1}{2}y \rightarrow -\frac{\sqrt{3}}{2}x - \frac{1}{2}y \tag{A.20}$$

$$z \rightarrow z \tag{A.21}$$

Starting with a counterclockwise rotation of the indices, the $\chi^{(2)}_{xxx}$ tensor components yield

$$
\begin{aligned}
xxx \rightarrow & (-\frac{1}{2}x + \frac{\sqrt{3}}{2}y)(-\frac{1}{2}x + \frac{\sqrt{3}}{2}y)(-\frac{1}{2}x + \frac{\sqrt{3}}{2}y) = \\
& (-\frac{1}{2}x + \frac{\sqrt{3}}{2}y)(\frac{1}{4}xx - \frac{\sqrt{3}}{2}xy + \frac{3}{4}yy) = \\
& -\frac{1}{8}xxx + \frac{\sqrt{3}}{4}xxy - \frac{3}{8}xyy + \frac{\sqrt{3}}{8}yxx - \frac{3}{4}yxy + \frac{3\sqrt{3}}{8}yyy \\
\frac{9}{8}xxx = & \frac{\sqrt{3}}{4}xxy - \frac{3}{8}xyy + \frac{\sqrt{3}}{8}yxx - \frac{3}{4}yxy + \frac{3\sqrt{3}}{8}yyy
\end{aligned}
$$

while the clockwise rotation yields,

$$
\begin{aligned}
xxx \rightarrow & (-\frac{1}{2}x - \frac{\sqrt{3}}{2}y)(-\frac{1}{2}x - \frac{\sqrt{3}}{2}y)(-\frac{1}{2}x - \frac{\sqrt{3}}{2}y) = \\
& (-\frac{1}{2}x - \frac{\sqrt{3}}{2}y)(\frac{1}{4}xx + \frac{\sqrt{3}}{2}xy + \frac{3}{4}yy) = \\
& -\frac{1}{8}xxx - \frac{\sqrt{3}}{4}xxy - \frac{3}{8}xyy - \frac{\sqrt{3}}{8}yxx - \frac{3}{4}yxy - \frac{3\sqrt{3}}{8}yyy \\
\frac{9}{8}xxx = & -\frac{\sqrt{3}}{4}xxy - \frac{3}{8}xyy - \frac{\sqrt{3}}{8}yxx - \frac{3}{4}yxy - \frac{3\sqrt{3}}{8}yyy
\end{aligned}
$$

A similar approach can be followed for the other tensor components. Prior to the clockwise rotation, the counterclockwise rotation is evaluated.

$$
\begin{aligned}
xyy \rightarrow & (-\frac{1}{2}x - \frac{\sqrt{3}}{2}y)(\frac{\sqrt{3}}{2}x - \frac{1}{2}y)(\frac{\sqrt{3}}{2}x - \frac{1}{2}y) = \\
& (-\frac{1}{2}x - \frac{\sqrt{3}}{2}y)(\frac{3}{4}xx - \frac{\sqrt{3}}{2}xy + \frac{1}{4}yy) = \\
& -\frac{3}{8}xxx + \frac{\sqrt{3}}{4}xxy - \frac{1}{8}xyy - 3\frac{\sqrt{3}}{8}yxx + \frac{3}{4}yxy - \frac{\sqrt{3}}{8}yyy \\
\frac{9}{8}xyy = & -\frac{3}{8}xxx + \frac{\sqrt{3}}{4}xxy - 3\frac{\sqrt{3}}{8}yxx + \frac{3}{4}yxy - \frac{\sqrt{3}}{8}yyy
\end{aligned}
$$

$$
\begin{aligned}
xyy \rightarrow & (-\frac{1}{2}x + \frac{\sqrt{3}}{2}y)(-\frac{\sqrt{3}}{2}x - \frac{1}{2}y)(-\frac{\sqrt{3}}{2}x - \frac{1}{2}y) = \\
& (-\frac{1}{2}x + \frac{\sqrt{3}}{2}y)(\frac{3}{4}xx + \frac{\sqrt{3}}{2}xy + \frac{1}{4}yy) = \\
& -\frac{3}{8}xxx - \frac{\sqrt{3}}{4}xxy - \frac{1}{8}xyy + 3\frac{\sqrt{3}}{8}yxx + \frac{3}{4}yxy + \frac{\sqrt{3}}{8}yyy \\
\frac{9}{8}xyy = & -\frac{3}{8}xxx - \frac{\sqrt{3}}{4}xxy + 3\frac{\sqrt{3}}{8}yxx + \frac{3}{4}yxy + \frac{\sqrt{3}}{8}yyy
\end{aligned}
$$

$$
\begin{aligned}
xzz \rightarrow & -\frac{1}{2}xzz - \frac{\sqrt{3}}{2}yzz \\
\frac{3}{2}xzz = & -\frac{\sqrt{3}}{2}yzz \\
xzz \rightarrow & -\frac{1}{2}xzz + \frac{\sqrt{3}}{2}yzz \\
\frac{3}{2}xzz = & \frac{\sqrt{3}}{2}yzz
\end{aligned}
$$

From the latter two symmetry rotations, it can be notices that $\frac{3}{2}xzz = \frac{\sqrt{3}}{2}yzz = -\frac{\sqrt{3}}{2}yzz$. This can only be true if $\chi^{(2)}_{xzz} = \chi^{(2)}_{yzz} = 0$. This is the first simplification to the second-order susceptibility tensor from eq. (A.3).

Continuing this approach for the remaining tensor elements results in,

$$
\begin{aligned}
xyz \rightarrow & (-\frac{1}{2}x - \frac{\sqrt{3}}{2}y)(\frac{\sqrt{3}}{2}xz - \frac{1}{2}yz) \\
\frac{3}{4}xyz = & -\frac{\sqrt{3}}{4}xxz - \frac{3}{4}yxz + \frac{\sqrt{3}}{4}yyz
\end{aligned}
$$

$$xyz \rightarrow (-\frac{1}{2}x + \frac{\sqrt{3}}{2}y)(-\frac{\sqrt{3}}{2}xz - \frac{1}{2}yz)$$

$$\frac{3}{4}xyz = \frac{\sqrt{3}}{4}xxz - \frac{3}{4}yxz - \frac{\sqrt{3}}{4}yyz$$

$$xzx \rightarrow (-\frac{1}{2}x - \frac{\sqrt{3}}{2}y)(-\frac{1}{2}xz - \frac{\sqrt{3}}{2}yz)$$

$$\frac{3}{4}xzx = \frac{\sqrt{3}}{4}xyz + \frac{3}{4}yyz + \frac{\sqrt{3}}{4}yxz$$

$$xzx \rightarrow (-\frac{1}{2}x + \frac{\sqrt{3}}{2}y)(-\frac{1}{2}xz + \frac{\sqrt{3}}{2}yz)$$

$$\frac{3}{4}xzx = -\frac{\sqrt{3}}{4}xyz - \frac{3}{4}yyz + \frac{\sqrt{3}}{4}yxz$$

$$xyx \rightarrow (-\frac{1}{2}x - \frac{\sqrt{3}}{2}y)(\frac{\sqrt{3}}{2}x - \frac{1}{2}y)(-\frac{1}{2}x - \frac{\sqrt{3}}{2}y)$$

$$(-\frac{1}{2}x - \frac{\sqrt{3}}{2}y)(-\frac{\sqrt{3}}{4}xx - \frac{2}{4}xy + \frac{\sqrt{3}}{4}yy)$$

$$\frac{6}{8}xyx = \frac{\sqrt{3}}{8}xxx - \frac{\sqrt{3}}{8}xyy + \frac{3}{8}yxx + 2\frac{\sqrt{3}}{8}yxy - \frac{3}{8}yyy$$

$$xyx \rightarrow (-\frac{1}{2}x + \frac{\sqrt{3}}{2}y)(-\frac{\sqrt{3}}{2}x - \frac{1}{2}y)(-\frac{1}{2}x + \frac{\sqrt{3}}{2}y)$$

$$(-\frac{1}{2}x + \frac{\sqrt{3}}{2}y)(\frac{\sqrt{3}}{4}xx - \frac{2}{4}xy - \frac{\sqrt{3}}{4}yy)$$

$$\frac{6}{8}xyx = -\frac{\sqrt{3}}{8}xxx + \frac{\sqrt{3}}{8}xyy + \frac{3}{8}yxx - 2\frac{\sqrt{3}}{8}yxy - \frac{3}{8}yyy$$

$$yxx \rightarrow (\frac{\sqrt{3}}{2}x - \frac{1}{2}y)(-\frac{1}{2}x - \frac{\sqrt{3}}{2}y)(-\frac{1}{2}x - \frac{\sqrt{3}}{2}y) =$$

$$(\frac{\sqrt{3}}{2}x - \frac{1}{2}y)(\frac{1}{4}xx - \frac{\sqrt{3}}{2}xy + \frac{3}{4}yy)$$

$$\frac{9}{8}yxx = \frac{\sqrt{3}}{8}xxx - \frac{3}{4}xxy + \frac{3\sqrt{3}}{8}xyy + \frac{\sqrt{3}}{4}yxy - \frac{3}{8}yyy$$

$$yxx \rightarrow (-\frac{\sqrt{3}}{2}x - \frac{1}{2}y)(-\frac{1}{2}x + \frac{\sqrt{3}}{2}y)(-\frac{1}{2}x + \frac{\sqrt{3}}{2}y) =$$

$$(-\frac{\sqrt{3}}{2}x - \frac{1}{2}y)(\frac{1}{4}xx + \frac{\sqrt{3}}{2}xy + \frac{3}{4}yy)$$

$$\frac{9}{8}yxx = -\frac{\sqrt{3}}{8}xxx - \frac{3}{4}xxy - \frac{3\sqrt{3}}{8}xyy - \frac{\sqrt{3}}{4}yxy - \frac{3}{8}yyy$$

$$yyy \rightarrow (\frac{\sqrt{3}}{2}x - \frac{1}{2}y)(\frac{\sqrt{3}}{2}x - \frac{1}{2}y)(\frac{\sqrt{3}}{2}x - \frac{1}{2}y) =$$

$$(\frac{\sqrt{3}}{2}x - \frac{1}{2}y)(\frac{3}{4}xx - \frac{\sqrt{3}}{2}xy + \frac{1}{4}yy)$$

$$\frac{9}{8}yyy = 3\frac{\sqrt{3}}{8}xxx - \frac{3}{4}xxy + \frac{\sqrt{3}}{8}xyy - \frac{3}{8}yxx + \frac{\sqrt{3}}{4}yxy$$

$$yyy \rightarrow (-\frac{\sqrt{3}}{2}x - \frac{1}{2}y)(-\frac{\sqrt{3}}{2}x - \frac{1}{2}y)(-\frac{\sqrt{3}}{2}x - \frac{1}{2}y) =$$

$$(-\frac{\sqrt{3}}{2}x - \frac{1}{2}y)(\frac{3}{4}xx + \frac{\sqrt{3}}{2}xy + \frac{1}{4}yy)$$

$$\frac{9}{8}yyy = -3\frac{\sqrt{3}}{8}xxx - \frac{3}{4}xxy - \frac{\sqrt{3}}{8}xyy - \frac{3}{8}yxx - \frac{\sqrt{3}}{4}yxy$$

From earlier calculations, we know that $\chi^{(2)}_{xzz} = \chi^{(2)}_{yzz} = 0$.

$$yzy \rightarrow (\frac{\sqrt{3}}{2}x - \frac{1}{2}y)(\frac{\sqrt{3}}{2}xz - \frac{1}{2}yz)$$

$$\frac{3}{4}yzy = \frac{3}{4}xxz - \frac{\sqrt{3}}{4}xyz - \frac{\sqrt{3}}{4}yxz$$

$$yzy \rightarrow (-\frac{\sqrt{3}}{2}x - \frac{1}{2}y)(-\frac{\sqrt{3}}{2}xz - \frac{1}{2}yz)$$

$$\frac{3}{4}yzy = \frac{3}{4}xxz + \frac{\sqrt{3}}{4}xyz + \frac{\sqrt{3}}{4}yxz$$

$$yzx \rightarrow (\frac{\sqrt{3}}{2}x - \frac{1}{2}y)(-\frac{1}{2}xz - \frac{\sqrt{3}}{2}yz)$$

$$\frac{3}{4}yzx = -\frac{\sqrt{3}}{4}xxz - \frac{3}{4}xyz + \frac{\sqrt{3}}{4}yyz$$

$$yzx \rightarrow (-\frac{\sqrt{3}}{2}x - \frac{1}{2}y)(-\frac{1}{2}xz + \frac{\sqrt{3}}{2}yz)$$

$$\frac{3}{4}yzx = \frac{\sqrt{3}}{4}xxz - \frac{3}{4}xyz - \frac{\sqrt{3}}{4}yyz$$

$$yxy \rightarrow (\frac{\sqrt{3}}{2}x - \frac{1}{2}y)(-\frac{1}{2}x - \frac{\sqrt{3}}{2}y)(\frac{\sqrt{3}}{2}x - \frac{1}{2}y) =$$

$$(\frac{\sqrt{3}}{2}x - \frac{1}{2}y)(-\frac{\sqrt{3}}{4}xx - \frac{2}{4}xy + \frac{\sqrt{3}}{4}yy)$$

$$\frac{6}{8}xyx = -\frac{3}{8}xxx - 2\frac{\sqrt{3}}{8}xxy + \frac{3}{8}xyy + \frac{\sqrt{3}}{8}yxx - \frac{\sqrt{3}}{8}yyy$$

$$yxy \rightarrow (-\frac{\sqrt{3}}{2}x - \frac{1}{2}y)(-\frac{1}{2}x + \frac{\sqrt{3}}{2}y)(-\frac{\sqrt{3}}{2}x - \frac{1}{2}y) =$$

$$(\frac{\sqrt{3}}{2}x - \frac{1}{2}y)(\frac{\sqrt{3}}{4}xx - \frac{2}{4}xy - \frac{\sqrt{3}}{4}yy)$$

$$\frac{6}{8}yxy = -\frac{3}{8}xxx + 2\frac{\sqrt{3}}{8}xxy + \frac{3}{8}xyy - \frac{\sqrt{3}}{8}yxx + \frac{\sqrt{3}}{8}yyy$$

$$zxx \rightarrow \frac{1}{4}zxx - \frac{\sqrt{3}}{2}zxy + \frac{3}{4}zyy =$$

$$\frac{3}{4}zxx = -\frac{\sqrt{3}}{2}zxy + \frac{3}{4}zyy$$

$$zxx \rightarrow \frac{1}{4}zxx + \frac{\sqrt{3}}{2}zxy + \frac{3}{4}zyy =$$

$$\frac{3}{4}zxx = \frac{\sqrt{3}}{2}zxy + \frac{3}{4}zyy$$

$$zyy \rightarrow \frac{3}{4}zxx - \frac{\sqrt{3}}{2}zxy + \frac{1}{4}zyy =$$

$$\frac{3}{4}zyy = \frac{3}{4}zxx - \frac{\sqrt{3}}{2}zxy$$

$$zyy \rightarrow \frac{3}{4}zxx + \frac{\sqrt{3}}{2}zxy + \frac{1}{4}zyy =$$

$$\frac{3}{4}zyy = \frac{3}{4}zxx + \frac{\sqrt{3}}{2}zxy$$

$$zzz \rightarrow zzz$$

$$zyz \rightarrow \frac{\sqrt{3}}{2}zxz - \frac{1}{2}zyz$$

$$\frac{3}{2}zyz = \frac{\sqrt{3}}{2}zxz$$

$$zyz \rightarrow -\frac{\sqrt{3}}{2}zxz - \frac{1}{2}zyz$$

$$\frac{3}{2}zyz = -\frac{\sqrt{3}}{2}zxz$$

This means that $\frac{\sqrt{3}}{2}zxz = -\frac{\sqrt{3}}{2}zxz$ so that $\chi_{zxz} = 0$ and consequently $\chi_{zyz} = 0$.

$$zyx \rightarrow -\frac{\sqrt{3}}{4}zxx - \frac{2}{4}zxy + \frac{\sqrt{3}}{4}zyy$$

$$\frac{3}{2}zyx = -\frac{\sqrt{3}}{4}zxx + \frac{\sqrt{3}}{4}zyy$$

$$zyx \rightarrow \frac{\sqrt{3}}{4}zxx - \frac{2}{4}zxy - \frac{\sqrt{3}}{4}zyy$$

$$\frac{3}{2}zyx = \frac{\sqrt{3}}{4}zxx - \frac{\sqrt{3}}{4}zyy$$

These symmetry operations give rise to the following simplified susceptibility tensor:

$$\begin{bmatrix} \chi^{(2)}_{xxx} & \chi^{(2)}_{xyy} & 0 & \chi^{(2)}_{xyz} & \chi^{(2)}_{xxz} & \chi^{(2)}_{xyx} \\ \chi^{(2)}_{yxx} & \chi^{(2)}_{yyy} & 0 & \chi^{(2)}_{yzy} & \chi^{(2)}_{yzx} & \chi^{(2)}_{yxy} \\ \chi^{(2)}_{zxx} & \chi^{(2)}_{zyy} & \chi^{(2)}_{zzz} & 0 & 0 & \chi^{(2)}_{zyx} \end{bmatrix} \tag{A.22}$$

without comparing the equality of certain equations. However, this has to be done, since the two rotations, clockwise and counterclockwise, account for the same symmetry operation. Hence,

$\frac{9}{8}xxx = \frac{\sqrt{3}}{4}xxy$ - $\frac{3}{8}xyy$ + $\frac{\sqrt{3}}{8}yxx$ - $\frac{3}{4}yxy$ + $\frac{3\sqrt{3}}{8}yyy$

$\frac{9}{8}xxx = -\frac{\sqrt{3}}{4}xxy$ - $\frac{3}{8}xyy$ - $\frac{\sqrt{3}}{8}yxx$ - $\frac{3}{4}yxy$ - $\frac{3\sqrt{3}}{8}yyy$

So $\frac{9}{8}xxx = -\frac{3}{8}xyy$ - $\frac{3}{4}yxy \rightarrow 3\ xxx = -xyy$-2 yxy

It is easily seen that xyy=yxy and that xxx=$-xyy$=$-yxy$.
The same can be done for the other components. Moreover, xxy, yxx and yyy

are zero, since

$$\begin{aligned}
\frac{3}{4}xyz &= -\frac{3}{4}yxz \\
\rightarrow xyz &= -yxz \\
\frac{9}{8}yxx &= -\frac{3}{4}xxy - \frac{3}{4}yyy \\
\rightarrow 3yxx &= -2xxy - yyy \\
\rightarrow xxy &= yyy = -yxx \\
yzy &= xxz \\
zxx &= zyy
\end{aligned}$$

Accounting for all these simplifications, eq. (A.3) simplifies to,

$$\begin{bmatrix}
\chi^{(2)}_{xxx} & -\chi^{(2)}_{xxx} & 0 & 0 & \chi^{(2)}_{xxz} & 0 \\
0 & 0 & 0 & \chi^{(2)}_{xzx} & 0 & -\chi^{(2)}_{xxx} \\
\chi^{(2)}_{zxx} & \chi^{(2)}_{zxx} & \chi^{(2)}_{zzz} & 0 & 0 & 0
\end{bmatrix} \tag{A.23}$$

A.2.2 Mirror planes

Similar to the case of a C_{4v} symmetry operation, the mirror plane symmetry operation does not yield additional simplifications to the susceptibility tensor compared to the threefold rotation symmetry operation. However, this approach is equally valid in calculating the simplifications to eq. (A.3).

Bibliography

[1] T. Maiman, *Stimulated optical radiation in Ruby*, Nature, **187** (4736), 494 (1960).

[2] P. A. Franken, A. E. Hill, C. W. Peters and G. Weinreich, *Generation of optical harmonics*, Physical Review Letters, **7** (4), 118–119 (1961).

[3] N. Bloembergen and P. Pershan, *Light waves at the boundary of nonlinear media*, Physical Review, **128** (2), 606–622 (1962).

[4] Y. Shen, *The Principles of Non-linear Optics* (Wiley, New York), 1992.

[5] M. Riordan and L. Hoddeson, *The birth of the information age* (Company, W. W. Norton, New York), 1997.

[6] S. M. Sze and K. N. Kwok, *Physics of semiconductor devices*, 3rd edition (John Wiley & sons, Inc., Delhi), 2007.

[7] R. W. Boyd, *Nonlinear optics (3rd edition)* (Academic Press), 2008.

[8] F. X. Wang, F. J. Rodríguez, W. M. Albers, R. Ahorinta, J. E. Sipe and M. Kauranen, *Surface and bulk contributions to the second-order nonlinear optical response of a gold film*, Physical Review B, **80** (23), 4–7 (2009).

[9] Y. R. Shen, *Surface properties probed by second-harmonic and sum-frequency generation*, Nature, **337** (9), 519–525 (1989).

[10] J. F. McGilp, *Optical characterisation of semiconductor surfaces and interfaces*, Progress in Surface Science, **49** (1), 1–106 (1995).

[11] O. A. Aktsipetrov, A. A. Fedyanin, J. I. Dadap and M. C. Downer, *DC-electric-field-induced second-harmonic generation studies of surfaces and buried interfaces of column IV semiconductors*, Laser Physics, **6** (6), 1142–1151 (1996).

[12] G. Hillrichs, D. Graf, G. Marowsky, O. Roders, A. Schnegg and P. Wagner, *Surface analysis of Si(111) wafers using second harmonic generation*, Journal of The Electrochemical Society, **141** (11), 3145–3151 (1994).

[13] C. Rotella, S. Napolitano, S. Vandendriessche, V. K. Valev, T. Verbiest, M. Larkowska, S. Kucharski and M. Wübbenhorst, *Adsorption kinetics of ultrathin polymer films in the melt probed by dielectric spectroscopy and second-harmonic generation*, Langmuir, **27** (22), 13533–13538 (2011).

[14] T. Heinz, M. Loy and W. Thompson, *Study of Si(111) surfaces by optical second-harmonic generation: Reconstruction and surface phase transformation*, Physical review letters, **54** (1), 63–66 (1985).

[15] H. W. K. Tom, X. D. Zhu, Y. R. Shen and G. A. Somorjai, *Investigation of the Si(111)-(7x7) surface by second-harmonic generation: oxidation and the effects of surface phosphorus*, Surface Science, **167** (1), 167–176 (1986).

[16] M. K. Vanbel, V. V. Afanas'ev, C. Adelmann, M. Caymax, V. K. Valev and T. Verbiest, *Tunneling of holes is observed by second-harmonic generation*, Applied Physics Letters, **102** (8), 082104 (2013).

[17] M. A. van der Veen, V. K. Valev, T. Verbiest and D. E. De Vos, *In situ orientation-sensitive observation of molecular adsorption on a liquid/zeolite interface by second-harmonic generation.*, Langmuir, **25** (8), 4256–4261 (2009).

[18] M. A. van der Veen, J. Van Noyen, B. F. Sels, P. A. Jacobs, T. Verbiest and D. E. De Vos, *Mapping of the organization of p-nitroaniline in SAPO-5 by second-harmonic generation microscopy*, Physical chemistry chemical physics, **12** (36), 10688–10692 (2010).

[19] P. Pershan, *Nonlinear Optical Properties of Solids: Energy Considerations*, Physical Review, **130** (3), 919–929 (1963).

[20] N. Bloembergen, R. Chang, S. Jha and C. Lee, *Optical second-harmonic generation in reflection from media with inversion symmetry*, Physical Review, **174** (3), 813–822 (1968).

[21] C. Wang, *Second-harmonic generation of light at the boundary of an isotropic medium*, Physical Review, **178** (3), 1457–1460 (1969).

[22] P. Guyot-Sionnest, W. Chen and Y. R. Shen, *General considerations on optical second-harmonic generation from surfaces and interfaces.*, Physical review. B, **33** (12), 8254–8263 (1986).

[23] J. E. Sipe, D. J. Moss and H. M. van Driel, *Phenomenological theory of optical second- and third-harmonic generation from cubic centrosymmetric crystals*, Physical Review B, **35** (3), 1129–1141 (1987).

[24] J. E. Sipe, *New Green-function formalism for surface optics*, Journal of the Optical Society of America B, **4** (4), 481–489 (1987).

[25] G. Lüpke, D. J. Bottomley and H. M. V. Driel, *Second- and third-harmonic generation from cubic centrosymmetric crystals with vicinal faces : phenomenological theory and experiment*, Journal of the Optical Society of America B, **11** (1), 33–44 (1994).

[26] S. Yang, X. Li, A. Bristow and J. Sipe, *Second harmonic generation from tetragonal centrosymmetric crystals*, Physical Review B, **80** (16), 1–9 (2009).

[27] C. H. Lee, R. K. Chang and N. Bloembergen, *Nonlinear electroreflectance in silicon and silver*, Physical Review Letters, **18** (5), 167–170 (1967).

[28] P. R. Fischer, J. L. Daschbach, D. E. Gragson and G. L. Richmond, *Sensitivity of second harmonic generation to space charge effects at Si(111)/electrolyte and Si(111)/SiO2/electrolyte interfaces*, Journal of Vacuum Science & Technology A, **12** (5), 2617–2624 (1994).

[29] O. A. Aktsipetrov, A. A. Fedyanin, A. V. Melnikov, E. D. Mishina, A. N. Rubtsov, M. H. Anderson, P. T. Wilson, M. Beek, X. F. Hu, J. I. Dadap and M. C. Downer, *DC-electric-field-induced and low-frequency electromodulation second-harmonic generation spectroscopy of Si(001)-SiO 2 interfaces*, Physical Review B, **60** (12), 8924–8938 (1999).

[30] O. Aktsipetrov, A. Fedyanin, A. Melnikov, J. Dadap, X. Hu, M. Anderson, M. Downer and J. Lowell, *DC electric field induced second-harmonic generation spectroscopy of the Si (001)-SiO2 interface: separation of the bulk and surface non-linear contributions*, Thin Solid Films, **294** (1-2), 231–234 (1997).

[31] R. Kempf, P. Wilson and J. Canterbury, *Third and fourth harmonic generation at Si-SiO2 interfaces and in Si-SiO2-Cr MOS structures*, Applied Physics B, **68** (3), 325–332 (1999).

[32] O. A. Aktsipetrov, A. A. Fedyanin, E. D. Mishina, A. N. Rubtsov, C. W. V. Hasselt and M. A. C. Devillers, *DC-electric-field-induced second-harmonic generation in Si(111)-SiO2-Cr metal-oxide-semiconductor structures*, Physical Review B, **54** (3), 1825–1832 (1996).

[33] M. K. Vanbel, C. Y. Su, J. P. Locquet and T. Verbiest, *Electric-field-induced second-harmonic generation demonstrates different interface*

properties of molecular beam epitaxy grown MgO on Si, The Journal of Physical Chemistry C, **118** (4), 1919–1924 (2014).

[34] H. Veendrick, *Nanometer CMOS IC's*, 1st edition (Springer, New York), 2008.

[35] J.-P. Locquet, C. Marchiori, M. Sousa, J. Fompeyrine and J. W. Seo, *High-K dielectrics for the gate stack*, Journal of Applied Physics, **100** (5), 051610 (2006).

[36] C. Claeys, J. Mitard, G. Eneman, M. Meuris and E. Simoen, *Si versus Ge for future microelectronics*, Thin Solid Films, **518** (9), 2301–2306 (2010).

[37] F. Schäffler, *High-mobility Si and Ge structures*, Semiconductor Science and Technology, **12** (12), 1515–1549 (1997).

[38] Y. Fang, V. D'Costa, J. Tolle, C. Poweleit, J. Kouvetakis and J. Menéndez, *Strained Si films grown by chemical vapor deposition of trisilane on Ge buffered Si (100)*, Thin Solid Films, **516** (23), 8327–8332 (2008).

[39] J. M. Hartmann, A. Abbadie, N. Cherkashin, H. Grampeix and L. Clavelier, *Epitaxial growth of Ge thick layers on nominal and 6° off Si(001); Ge surface passivation by Si*, Semiconductor Science and Technology, **24** (5), 055002 (2009).

[40] R. People and J. C. Bean, *Calculation of critical layer thickness versus lattice mismatch for GexSi1-x/Si strained-layer heterostructures*, Applied Physics Letters, **47** (3), 322–324 (1985).

[41] S. Sioncke, H. C. Lin, L. Nyns, G. Brammertz, A. Delabie, T. Conard, A. Franquet, J. Rip, H. Struyf, S. De Gendt, M. Müller, B. Beckhoff and M. Caymax, *S-passivation of the Ge gate stack: Tuning the gate stack properties by changing the atomic layer deposition oxidant precursor*, Journal of Applied Physics, **110** (8), 084907 (2011).

[42] C. Fleischmann, S. Sioncke, S. Couet, K. Schouteden, B. Beckhoff, M. Müller, P. Hönicke, M. Kolbe, C. Van Haesendonck, M. Meuris, K. Temst and A. Vantomme, *Towards Passivation of Ge(100) Surfaces by Sulfur Adsorption from a (NH4)2S Solution: A Combined NEXAFS, STM and LEED Study*, Journal of The Electrochemical Society, **158** (5), H589–H594 (2011).

[43] *http://www.itrs.net/reports.html*.

[44] J. Kim, L. J. Cote, F. Kim and J. Huang, *Visualizing graphene based sheets by fluorescence quenching microscopy*, Journal of the American Chemical Society, **132** (1), 260–267 (2010).

[45] W. Daum, *Optical studies of Si/SiO2 interfaces by second-harmonic generation spectroscopy of silicon interband transitions*, Applied Physics A, **87** (3), 451–460 (2007).

[46] M. L. Alles, R. Pasternak, X. Lu, N. H. Tolk, R. D. Schrimpf, D. M. Fleetwood, R. P. Dolan and R. W. Standley, *Second harmonic generation for noninvasive metrology of silicon-on-insulator wafers*, IEEE Transactions on Semiconductor Manufacturing, **20** (2), 107–113 (2007).

[47] M. C. Downer, B. S. Mendoza and V. I. Gavrilenko, *Optical second harmonic spectroscopy of semiconductor surfaces: advances in microscopic understanding*, Surface and Interface Analysis, **31** (10), 966–986 (2001).

[48] B. Jun, Y. V. White, R. D. Schrimpf, D. M. Fleetwood, F. Brunier, N. Bresson, S. Cristoloveanu and N. H. Tolk, *Characterization of multiple Si/SiO2 interfaces in silicon-on-insulator materials via second-harmonic generation*, Applied Physics Letters, **85** (15), 3095 (2004).

[49] V. Valev, M. Vanbel and B. Vincent, *Second harmonic generation indicates a better Si/Ge interface quality for higher temperature and with N2 rather than with H2 as the carrier gas*, IEEE electron device, **32** (1), 12–14 (2011).

[50] C. Meyer, G. Lüpke, U. Emmerichs, F. Wolter, H. Kurz, C. H. Bjorkman and G. Lucovsky, *Electronic transitions at Si(111)/SiO2 and Si(111)/Si3N4 interfaces studied by optical second-harmonic spectroscopy*, Physical review letters, **74** (15), 3001–3005 (1995).

[51] J. Dadap, Q. Deng, M. C. Downer and J. K. Lowell, *Randomly oriented Angstrom-scale microroughness at the Si(100)/SiO2, interface probed by optical second harmonic generation*, Applied Physics Letters, **64** (16), 2139–2141 (1994).

[52] S. T. Cundiff, W. H. Knox, F. H. Baumann, K. W. Evans-Lutterodt, M.-T. Tang, M. L. Green and H. M. V. Driel, *Si/SiO2 interface roughness: Comparison between surface second harmonic generation and x-ray scattering*, Applied Physics Letters, **70** (11), 2–5 (2001).

[53] W. Kessels, J. Gielis, B. Hoex, N. Terlinden, G. Dingemans, V. Verlaan and M. van de Sanden, *Electric field induced surface passivation of Si by atomic layer deposited Al2O3 studied by optical second-harmonic generation*, *in 2009 34th IEEE Photovoltaic Specialists Conference (PVSC)* (Ieee), 2009, 427–431.

[54] N. M. Terlinden, G. Dingemans, M. C. M. van de Sanden and W. M. M. Kessels, *Role of field-effect on c-Si surface passivation by ultrathin (-20*

nm) atomic layer deposited Al2O3, Applied Physics Letters, **96** (11), 112101 (2010).

[55] R. Carriles, J. Kwon, Y. Q. An, L. Sun, S. K. Stanley, J. G. Ekerdt, M. C. Downer, J. Price, T. Boescke and a. C. Diebold, *Optical characterization of process-dependent charging in hafnium oxide structures*, Journal of Vacuum Science & Technology B, **24** (4), 2160 (2006).

[56] V. Fomenko, E. P. Gusev and E. Borguet, *Optical second harmonic generation studies of ultrathin high-k dielectric stacks*, Journal of Applied Physics, **97** (8), 083711 (2005).

[57] V. Gavrilenko, *Differential reflectance and second-harmonic generation of the Si/SiO2 interface from first principles*, Physical Review B, **77** (15), 1–7 (2008).

[58] G. Lüpke, *Characterization of semiconductor interfaces by second-harmonic generation*, Surface Science Reports, **35** (3-4), 75–161 (1999).

[59] O. A. Aktsipetrov, V. O. Bessonov, A. A. Fedyanin and V. O. Val'dner, *DC-induced generation of the reflected second harmonic in silicon*, JETP Letters, **89** (2), 58–62 (2009).

[60] D. Lim, M. C. Downer and J. G. Ekerdt, *Second-harmonic spectroscopy of bulk boron-doped Si(001)*, Applied Physics Letters, **77** (2), 181 (2000).

[61] J. L. Fiore, V. V. Fomenko, D. Bodlaki and E. Borguet, *Second harmonic generation probing of dopant type and density at the Si/SiO2 interface*, Applied Physics Letters, **98** (4), 041905 (2011).

[62] Y. V. White, X. Lu, R. Pasternak, N. H. Tolk, A. Chatterjee, R. D. Schrimpf, D. M. Fleetwood, A. Ueda and R. Mu, *Studies of charge carrier trapping and recombination processes in Si/SiO2/MgO structures using second-harmonic generation*, Applied Physics Letters, **88** (6), 062102 (2006).

[63] H. Park, J. Qi, Y. Xu, K. Varga, S. M. Weiss, B. R. Rogers, G. Lüpke and N. Tolk, *Boron induced charge traps near the interface of Si/SiO2 probed by second harmonic generation*, Physica Status Solidi (B), **247** (8), 1997–2001 (2010).

[64] C.-L. Chang, W. C. Lee, L. K. Chu, M. Hong, J. Kwo and Y.-M. Chang, *Direct determination of flat-band voltage for metal/high κ oxide/semiconductor heterointerfaces by electric-field-induced second-harmonic generation*, Applied Physics Letters, **98** (17), 171902 (2011).

[65] R. Carriles, J. Kwon, Y. Q. An, J. C. Miller, M. C. Downer, J. Price and a. C. Diebold, *Second-harmonic generation from Si/SiO2/Hf1-xSixO2 structures*, Applied Physics Letters, **88** (16), 161120 (2006).

[66] L. He, J. D. Walker, H. M. Branz, C. T. Rogers and C. W. Teplin, *Measurement of electric-field induced second harmonic generation in hydrogenated amorphous silicon*, Applied Physics Letters, **101** (16), 161604 (2012).

[67] N. Tolk, M. Alles, R. Pasternak, X. Lu, R. Schrimpf, D. Fleetwood, R. Dolan and R. Standley, *Oxide interface studies using second harmonic generation*, Microelectronic Engineering, **84** (9-10), 2089–2092 (2007).

[68] Y.-M. Chang, Y.-L. Hong and S. Gwo, *Direct probe of the built-in electric field of Mg-doped a-plane wurtzite InN surfaces with time-resolved electric-field-induced second harmonic generation*, Applied Physics Letters, **93** (13), 131106 (2008).

[69] K. S. Novoselov, A. Geim, S. V. Morozov, D. Jiang, Y. Zhang, S. V. Dubonos, I. V. Grigorieva and A. A. Firsov, *Electric field effect in atomically thin carbon films*, Science, **306** (5696), 666–669 (2004).

[70] J. K. Park, S. M. Song, J. H. Mun and B. J. Cho, *Graphene gate electrode for MOS structure-based electronic devices*, Nano letters, **11** (12), 5383–5386 (2011).

[71] S. Thongrattanasiri, I. Silveiro and J. F. Garcia de Abajo, *Plasmons in electrostatically doped graphene*, Applied Physics Letters, **100** (20), 201105 (2012).

[72] G. V. Naik, V. M. Shalaev and A. Boltasseva, *Alternative plasmonic materials: beyond gold and silver*, Advanced materials, **25** (24), 3264–3294 (2013).

[73] A. H. Castro Neto, N. M. R. Peres, K. S. Novoselov and A. K. Geim, *The electronic properties of graphene*, Reviews of Modern Physics, **81** (1), 109–162 (2009).

[74] F. Bonaccorso, Z. Sun, T. Hasan and A. C. Ferrari, *Graphene photonics and optoelectronics*, Nature Photonics, **4** (9), 611–622 (2010).

[75] R. Stöhr, R. Kolesov, J. Pflaum and J. Wrachtrup, *Fluorescence of laser-created electron-hole plasma in graphene*, Physical Review B, **82** (12), 3–6 (2010).

[76] X.-F. Zhang, X. Shao and S. Liu, *Dual fluorescence of graphene oxide: a time-resolved study.*, The journal of physical chemistry A, **116** (27), 7308–7313 (2012).

[77] J. J. Dean and H. M. van Driel, *Second harmonic generation from graphene and graphitic films*, Applied Physics Letters, **95** (26), 261910 (2009).

[78] J. Dean and H. van Driel, *Graphene and few-layer graphite probed by second-harmonic generation: Theory and experiment*, Physical Review B, **82** (12), 1–10 (2010).

[79] S.-Y. Hong, J. I. Dadap, N. Petrone, P.-C. Yeh, J. Hone and R. M. Osgood, *Optical third-harmonic generation in graphene*, Physical Review X, **3** (2), 021014 (2013).

[80] N. Kumar, J. Kumar, C. Gerstenkorn, R. Wang, H.-Y. Chiu, A. L. Smirl and H. Zhao, *Third harmonic generation in graphene and few-layer graphite films*, Physical Review B, **87** (12), 121406 (2013).

[81] W.-T. Liu, S. Wu, P. Schuck, M. Salmeron, Y. Shen and F. Wang, *Nonlinear broadband photoluminescence of graphene induced by femtosecond laser irradiation*, Physical Review B, **82** (8), 1–4 (2010).

[82] M. Feng, H. Zhan and Y. Chen, *Nonlinear optical and optical limiting properties of graphene families*, Applied Physics Letters, **96** (3), 033107 (2010).

[83] X. Yao and A. Belyanin, *Nonlinear optics of graphene in a strong magnetic field*, Journal of Physics: Condensed Matter, **25** (5), 054203 (2013).

[84] Q. Liu, B. Guo, Z. Rao, B. Zhang and J. R. Gong, *Strong two-photon-induced fluorescence from photostable, biocompatible nitrogen-doped graphene quantum dots for cellular and deep-tissue imaging.*, Nano letters, **13** (6), 2436–2441 (2013).

[85] M. Caymax, G. Eneman, F. Bellenger, C. Merckling, a. Delabie, G. Wang, R. Loo, E. Simoen, J. Mitard, B. De Jaeger, G. Hellings, K. De Meyer, M. Meuris and M. Heyns, *Germanium for advanced CMOS anno 2009: a SWOT analysis*, 2009 IEEE International Electron Devices Meeting (IEDM), 1–4 (2009).

[86] B. Vincent, R. Loo, W. Vandervorst, J. Delmotte, B. Douhard, V. Valev, M. Vanbel, T. Verbiest, J. Rip and B. Brijs, *Si passivation for Ge pMOSFETs: Impact of Si cap growth conditions*, Solid-state electronics, 1–6 (2011).

[87] B. Vincent, J. Damlencourt, Y. Morand, A. Pouydebasque, C. Le Royer, L. Clavelier, N. Dechoux, P. Rivallin, T. Nguyen and S. Cristoloveanu, *The Ge condensation technique: A solution for planar SOI/GeOI co-integration for advanced CMOS technologies?*, Materials Science in Semiconductor Processing, **11** (5-6), 205–213 (2008).

[88] S. Thompson and S. Parthasarathy, *Moore's law: the future of Si microelectronics*, Materials Today, **9** (6), 20–25 (2006).

[89] R. H. Dennard, F. H. Gaensslen, H.-N. Yu, V. L. Rideout, E. Bassous and A. R. LeBlanc, *Design of ion-implanted small MOSFET's dimensions with very small physical dimensions*, IEEE journal of solid-state circuits, **9** (5), 256–268 (1974).

[90] D. P. Vallett, *IC failure analysis : the importance of test and diagnostics*, IEEE design & test of computers, **14** (3), 76–82 (1997).

[91] V. K. Valev, F. E. Leys, M. Caymax and T. Verbiest, *Difference in the nonlinear optical response of epitaxial Si on Ge(100) grown from SiH4 at 500)C and from Si3H8 350 °C due to segregation of Ge*, Applied Physics Letters, **94** (6), 2009–2011 (2009).

[92] J. Mitard, C. Shea, B. Dejaeger, A. Pristera, G. Wang, M. Houssa, G. Eneman, G. Hellings, W.-e. Wang, J. C. Lin, F. E. Leys, R. Loo, G. Winderickx, E. Vrancken, A. Stesmans, K. Demeyer, M. Caymax, L. Pantisano, M. Meuris and M. Heyns, *Impact of EOT scaling down to 0.85nm on 70nm Ge-pFETs technology with STI*, Technology, **5** (82), 82–83 (2009).

[93] J. Litwin, J. Sipe and H. van Driel, *Picosecond and nanosecond laser-induced second-harmonic generation from centrosymmetric semiconductors*, Physical Review B, **31** (8), 5543–5546 (1985).

[94] V. Valev, A. Kirilyuk, F. Dalla Longa, J. Kohlhepp, B. Koopmans and T. Rasing, *Observation of periodic oscillations in magnetization-induced second harmonic generation at the Mn/Co interface*, Physical Review B, **75** (1), 3–6 (2007).

[95] J. McGilp, *Optical characterisation of semiconductor surfaces and interfaces*, Progress in Surface Science, **49** (1), 1–106 (1995).

[96] W. Kolthammer, D. Barnard, N. Carlson, A. Edens, N. Miller and P. Saeta, *Harmonic generation in thin films and multilayers*, Physical Review B, **72** (4), 1–15 (2005).

[97] T. F. Heinz, M. Loy and W. Thompson, *Study of symmetry and disordering of Si(111)-7x7 surfaces by optical second harmonic generation*, Journal of Vacuum Science & Technology B, **3** (5), 1467 (1985).

[98] L. A. F. M., J. A. M. Huethorst and J. J. Van Oekel, *Marangoni drying : a new extremely clean drying process*, Langmuir, **6** (11), 1701–1703 (1990).

[99] T. Verbiest, K. Clays and V. Rodriguez, *Second-order nonlinear optical characterization techniques* (CRC press Taylor & Francis group), 2009.

[100] D. J. Bottomley, G. Lüpke, C. Meyer and Y. Makita, *Exact separation of surface and bulk contributions to anisotropic second-harmonic generation from cubic centrosymmetric media*, Optics letters, **20** (5), 453–5 (1995).

[101] van Hasselt C W, M. A. Verheijen and T. Rasing, *Vicinal Si(111) surfaces studied by optical second-harmonic generation: Step-induced anisotropy and surface-bulk discrimination*, Physical review. B, **42** (14), 9263–9266 (1990).

[102] T. Scheidt, E. G. Rohwer, P. Neethling, H. M. von Bergmann and H. Stafast, *Ionization and shielding of interface states in native p+-Si/SiO2 probed by electric field induced second harmonic generation*, Journal of Applied Physics, **104** (8), 083712 (2008).

[103] V. Kaushik, B. O'Sullivan, G. Pourtois, N. Van Hoornick, a. Delabie, S. Van Elshocht, W. Deweerd, T. Schram, L. Pantisano, E. Rohr, L.-a. Ragnarsson, S. De Gendt and M. Heyns, *Estimation of fixed charge densities in hafnium-silicate gate dielectrics*, IEEE Transactions on Electron Devices, **53** (10), 2627–2633 (2006).

[104] Q. Jin, H. Regensburger, R. Vollmer and J. Kirschner, *Periodic Oscillations of the Surface Magnetization during the Growth of Co Films on Cu(001)*, Physical Review Letters, **80** (18), 4056–4059 (1998).

[105] J. Hamrle, L. Polerecky and J. Ferré, *Theory of second-harmonic generation from multilayer systems based on electric point-dipole radiation: Application to magnetic multilayers*, Physical Review B, **68** (14), 144401 (2003).

[106] H. Wierenga, M. Prins and T. Rasing, *Magnetization-induced optical second-harmonic generation from magnetic multilayers*, Physica B, **204** (1-4), 281–286 (1995).

[107] T. B. Kristensen, K. Pedersen and T. G. Pedersen, *Optical second-harmonic generation from an Au wedge on Si(111)*, Physica Status Solidi (a), **175** (1), 195–200 (1999).

[108] B. Vincent, R. Loo, W. Vandervorst, G. Brammertz and M. Caymax, *Low temperature Si homo-epitaxy by reduced pressure chemical vapor deposition using dichlorosilane, silane and trisilane*, Journal of Crystal Growth, **312** (19), 2671–2676 (2010).

[109] J. Dadap, X. Hu, M. Anderson, M. Downer, J. Lowell and O. Aktsipetrov, *Optical second-harmonic electroreflectance spectroscopy of a Si(001) metal-oxide-semiconductor structure*, Physical review B, **53** (12), R7607–R7609 (1996).

[110] H. Hirayama, T. Komizo, T. Kawata and K. Takayanagi, *Changes of phase and intensity of optical SHG with Ag deposition on Si (111)-7x7 surfaces*, Applied Surface Science, **190** (180), 108–112 (2002).

[111] B. De Jaeger, R. Bonzom, F. Leys, O. Richard, J. V. Steenbergen, G. Winderickx, E. V. Moorhem, G. Raskin, F. Letertre, T. Billon, M. Meuris and M. Heyns, *Optimisation of a thin epitaxial Si layer as Ge passivation layer to demonstrate deep sub-micron n- and p-FETs on Ge-On-Insulator substrates*, Microelectronic Engineering, **80**, 26–29 (2005).

[112] Y.-Y. Fang, V. D'Costa, J. Tolle, C. Poweleit, J. Kouvetakis and J. Menéndez, *Strained Si films grown by chemical vapor deposition of trisilane on Ge buffered Si(100)*, Thin Solid Films, **516** (23), 8327–8332 (2008).

[113] M. Caymax, F. Leys, J. Mitard, K. Martens, L. Yang, G. Pourtois, W. Vandervorst, M. Meuris and R. Loo, *The influence of the epitaxial growth process parameters on layer characteristics and device performance in Si-passivated Ge pMOSFETs*, Journal of The Electrochemical Society, **156** (12), H979–H985 (2009).

[114] V. Fomenko, J.-F. Lami and E. Borguet, *Nonquadratic second-harmonic generation from semiconductor-oxide interfaces*, Physical Review B, **63** (12), 1–4 (2001).

[115] B. Vincent, W. Vandervorst, M. Caymax and R. Loo, *Influence of Si precursor on Ge segregation during ultrathin Si reduced pressure chemical vapor deposition on Ge*, Applied Physics Letters, **95** (26), 262112 (2009).

[116] G. Moore, *Progress In Digital Integrated Electronics*, IEEE Solid-State Circuits Newsletter, **20** (3), 36–37 (2006).

[117] D. P. Brunco, B. De Jaeger, G. Eneman, J. Mitard, G. Hellings, A. Satta, V. Terzieva, L. Souriau, F. E. Leys, G. Pourtois, M. Houssa, G. Winderickx, E. Vrancken, S. Sioncke, K. Opsomer, G. Nicholas, M. Caymax, A. Stesmans, J. Van Steenbergen, P. W. Mertens, M. Meuris and M. M. Heyns, *Germanium MOSFET devices: advances in materials understanding, process development, and electrical performance*, Journal of The Electrochemical Society, **155** (7), H552–H561 (2008).

[118] H. Shang, H. Okorn-Schimdt, J. Ott, P. Kozlowski, S. Steen, E. Jones, H.-S. Wong and W. Hanesch, *Electrical characterization of germanium p-channel MOSFETs*, IEEE Electron Device Letters, **24** (4), 242–244 (2003).

[119] J. A. Dean, *CRC handbook of chemistry and physics: 85nd edition* (CRC press Taylor & Francis group, New York), 1998.

[120] V. V. Afanas'ev, Y. G. Fedorenko and A. Stesmans, *Interface traps and dangling-bond defects in (100)Ge/HfO2*, Applied Physics Letters, **87** (3), 032107 (2005).

[121] C. O. Chui, S. Ramanathan, B. B. Triplett, P. C. Mcintyre and K. C. Saraswat, *Germanium MOS Capacitors Incorporating Ultrathin*, IEEE Electron Device Letters, **23** (8), 473–475 (2002).

[122] M. C. Downer, B. S. Mendoza and V. I. Gavrilenko, *Optical second harmonic spectroscopy of semiconductor surfaces: advances in microscopic understanding*, Surface and Interface Analysis, **31** (10), 966–986 (2001).

[123] A. Kirilyuk and T. Rasing, *Magnetization-induced-second-harmonic generation from surfaces and interfaces*, Journal of the Optical Society of America B, **22** (1), 148 (2005).

[124] V. K. Valev, M. Gruyters, A. Kirilyuk and T. Rasing, *Influence of quadratic contributions in magnetization-induced second harmonic generation studies of magnetization reversal*, Physica Status Solidi (B), **242** (15), 3027–3031 (2005).

[125] Y. Sheng, A. Best, H.-J. Butt, W. Krolikowski, A. Arie and K. Koynov, *Three-dimensional ferroelectric domain visualization by Cerenkov-type second harmonic generation*, Optics express, **18** (16), 16539–16545 (2010).

[126] V. Pavlov, J. Ferré, P. Meyer, G. Tessier, P. Georges, A. Brun, P. Beauvillain and V. Mathet, *Linear and non-linear magneto-optical studies of Pt/Co/Pt thin films*, Journal of Physics: Condensed Matter, **13** (44), 9867–9878 (2001).

[127] V. K. Valev, X. Zheng, C. Biris, A. Silhanek, V. Volskiy, B. De Clercq, O. A. Aktsipetrov, M. Ameloot, N. C. Panoiu, G. A. E. Vandenbosch and V. V. Moshchalkov, *The origin of second harmonic generation hotspots in chiral optical metamaterials*, Optical Materials Express, **1** (1), 36 (2011).

[128] V. K. Valev, A. V. Silhanek, B. De Clercq, W. Gillijns, Y. Jeyaram, X. Zheng, V. Volskiy, O. A. Aktsipetrov, G. A. E. Vandenbosch, M. Ameloot, V. V. Moshchalkov and T. Verbiest, *U-shaped switches for optical information processing at the nanoscale*, Small, **7** (18), 2573–2576 (2011).

[129] V. K. Valev, D. Denkova, X. Zheng, A. I. Kuznetsov, C. Reinhardt, B. N. Chichkov, G. Tsutsumanova, E. J. Osley, V. Petkov, B. De Clercq, A. V. Silhanek, Y. Jeyaram, V. Volskiy, P. A. Warburton, G. A. E. Vandenbosch,

S. Russev, O. A. Aktsipetrov, M. Ameloot, V. V. Moshchalkov and T. Verbiest, *Plasmon-enhanced sub-wavelength laser ablation: plasmonic nanojets*, Advanced materials, **24** (10), OP29–OP35 (2012).

[130] M. K. Vanbel, V. K. Valev, B. Vincent, V. V. Afanas'ev, J.-P. Locquet, S. Van Elshocht, M. Caymax and T. Verbiest, *Second-harmonic generation reveals the oxidation steps in semiconductor processing*, Journal of Applied Physics, **111** (6), 064504 (2012).

[131] M. Falasconi, L. C. Andreani, A. M. Malvezzi, M. Patrini and V. Mulloni, *Bulk and surface contributions to second-order susceptibility in crystalline and porous silicon by second-harmonic generation*, Surface Science, **481** (1-3), 105–112 (2001).

[132] A. Delabie, S. Sioncke, J. Rip, S. Van Elshocht, M. Caymax, G. Pourtois and K. Pierloot, *Mechanisms for the trimethylaluminum reaction in aluminum oxide atomic layer deposition on sulfur passivated germanium*, The Journal of Physical Chemistry C, **115** (35), 17523–17532 (2011).

[133] Y. Glinka, W. Wang, S. Singh, Z. Marka, S. Rashkeev, Y. Shirokaya, R. Albridge, S. Pantelides, N. Tolk and G. Lucovsky, *Characterization of charge-carrier dynamics in thin oxide layers on silicon by second harmonic generation*, Physical Review B, **65** (19), 1–4 (2002).

[134] T. Scheidt, E. Rohwer, H. von Bergmann and H. Stafast, *Charge-carrier dynamics and trap generation in native Si/SiO2 interfaces probed by optical second-harmonic generation*, Physical Review B, **69** (16), 1–8 (2004).

[135] L. Gomez, P. Hashemi, S. Member and J. L. Hoyt, *Enhanced hole transport in short-channel*, IEEE transactions on electron devices, **56** (11), 2644–2651 (2009).

[136] W. Yu, B. Zhang, Q. Zhao, J.-M. Hartmann, D. Buca, A. Nichau, R. Lupták, J. Lopes, S. Lenk, M. Luysberg, K. Bourdelle, X. Wang and S. Mantl, *High mobility compressive strained Si0.5Ge0.5 quantum well p-MOSFETs with higher-k/metal-gate*, Solid-State Electronics, **62** (1), 185–188 (2011).

[137] M. K. Vanbel, A. Delabie, S. Sioncke, C. Adelmann, V. V. Afanas'ev, J.-P. Locquet, S. Van Elshocht, M. Caymax and T. Verbiest, *Second-harmonic generation as characterization tool for Ge/high-k dielectric interfaces*, Proceedings of SPIE, **8434** (May 2012), 84341F (2012).

[138] T. Heinz, H. Tom and Y. Shen, *Determination of molecular orientation of monolayer adsorbates by optical second-harmonic generation*, Physical Review A, **28** (3), 1883–1885 (1983).

[139] Z. A. Weinberg, *tunneling of electrons from Si into thermally grown SiO2*, Solid-State Electronics, **20** (1), 11–18 (1977).

[140] C. W. V. Hasselt, M. A. C. Devillers, T. Rasing and O. A. Aktsipetrov, *Second-harmonic generation from thick thermal oxides on Si(111): the influence of multiple reflections*, Journal of the Optical Society of America B, **12** (1), 33 (1995).

[141] A. Bongiorno, A. Pasquarello, M. S. Hybertsen and L. C. Feldman, *Transition Structure at the Si(100)-SiO2 Interface*, Physical Review Letters, **90** (18), 186101 (2003).

[142] M. L. Green, T. W. Sorsch, G. L. Timp, D. A. Muller, B. E. Weir, P. J. Silvermann, S. V. Moccio and Y. O. Kim, *Understanding the Limits of Ultrathin SiO2 and Si-O-N Gate Dielectrics for sub-50 nm CMOS*, Microelectronic Engineering, **48** (1-4), 25–30 (1999).

[143] A. Ando, R. Hasunuma, T. Maeda and K. Sakamoto, *Conducting atomic force microscopy studies on local electrical properties of ultrathin SiO 2 films*, Applied Surface Science, **162** (401), 401–405 (2000).

[144] J.-P. Locquet, C. Marchiori, M. Sousa, J. Fompeyrine and J. W. Seo, *High-K dielectrics for the gate stack*, Journal of Applied Physics, **100** (5), 051610 (2006).

[145] Y. Jiang and N. Bahlawane, *Effect of nucleation and growth kinetics on the electrical and optical properties of undoped ZnO films*, The Journal of Physical Chemistry C, **114** (11), 5121–5125 (2010).

[146] M. L. Addonizio and A. Antonaia, *Enhanced electrical stability of LP-MOCVD-deposited ZnO:Blayers by means of plasma etching treatment*, The Journal of Physical Chemistry C, **117** (46), 24268–24276 (2013).

[147] C. Samyn, T. Verbiest, E. Kesters, K. Van den Broeck, M. Van Beylen and a. Persoons, *High glass transition chromophore functionalised poly(maleimide-styrene)s for second-order nonlinear optical applications*, Polymer, **41** (16), 6049–6054 (2000).

[148] T. Verbiest, S. V. Elshocht, C. Nuckolls, K. E. Phillips and T. J. Katz, *Second-order nonlinear optical properties of highly symmetric chiral thin films*, Langmuir, **17** (16), 1997–1999 (2001).

[149] J. J. H. Gielis, B. Hoex, M. C. M. van de Sanden and W. M. M. Kessels, *Negative charge and charging dynamics in Al2O3 films on Si characterized by second-harmonic generation*, Journal of Applied Physics, **104** (7), 073701 (2008).

[150] Y. V. White, X. Lu, R. Pasternak, N. H. Tolk, A. Chatterjee, R. D. Schrimpf, D. M. Fleetwood, A. Ueda and R. Mu, *Studies of charge carrier trapping and recombination processes in Si/SiO2/MgO structures using second-harmonic generation*, Applied Physics Letters, **88** (6), 062102 (2006).

[151] C.-Y. Su, M. Menghini, T. Smets, L. Dillemans, R. Lieten and J. P. Locquet, *Influence of the Surface Pretreatment on the Electrical Properties of MgO and Al2O3 Gate Stacks grown by MBE*, *in IOP Conference Series: Materials Science and Engineering*, volume 41 (2012, 012010.

[152] S. Guha and V. Narayanan, *Oxygen Vacancies in High Dielectric Constant Oxide-Semiconductor Films*, Physical Review Letters, **98** (19), 196101 (2007).

[153] S. Guha, V. K. Paruchuri, M. Copel, V. Narayanan, Y. Y. Wang, P. E. Batson, N. a. Bojarczuk, B. Linder and B. Doris, *Examination of flatband and threshold voltage tuning of HfO2/TiN field effect transistors by dielectric cap layers*, Applied Physics Letters, **90** (9), 092902 (2007).

[154] W. Li, O. Auciello, R. N. Premnath and B. Kabius, *Giant dielectric constant dominated by Maxwell-Wagner relaxation in Al2O3/TiO2 nanolaminates synthesized by atomic layer deposition*, Applied Physics Letters, **96** (16), 162907 (2010).

[155] C.-Y. Su, M. Frederickx, M. Menghini, L. Dillemans, R. Lieten, T. Smets, J. W. Seo and J.-P. Locquet, *Deposition and characterization of MgO/Si gate stacks grown by molecular beam epitaxy*, Thin Solid Films, **520** (14), 4508–4511 (2012).

[156] D. K. Schroder, *Semiconductor Material and Device Characterization* (John Wiley & Sons, Inc., Hoboken, NJ, USA), 2005.

[157] J. T. Dickinson, S. C. Langford, J. J. Shin and D. L. Doering, *Positive ion emission from excimer laser excited MgO surfaces*, Physical Review Letters, **73** (19), 2630–2633 (1994).

[158] J. Ulises Reveles, A. M. Köster, S. N. Khanna and C. Quintanar, *Surface oxygen diffusion into neutral, cationic, and dicationic oxygen vacancies on MgO (100) surfaces*, Journal of Physical Chemistry C, **114** (100), 12265–12270 (2010).

[159] E. A. Kotomin, S. Piskunov, Y. F. Zhukovskii, R. I. Eglitis, A. Gopejenko and D. E. Ellis, *The electronic properties of an oxygen vacancy at ZrO(2)-terminated (001) surfaces of a cubic PbZrO(3): computer simulations from the first principles*, Physical chemistry chemical physics : PCCP, **10** (29), 4258–4263 (2008).

[160] M. Yoshikawa, K. Saitoh, T. Ohshima, H. Itoh, I. Nashiyama, S. Yoshida, H. Okumura, Y. Takahashi and K. Ohnishi, *Depth profile of trapped charges in oxide layer of 6H-SiC metal-oxide-semiconductor structures*, Journal of Applied Physics, **80** (1), 282–287 (1996).

[161] K. S. Novoselov, D. Jiang, F. Schedin, T. J. Booth, V. V. Khotkevich, S. V. Morozov and A. K. Geim, *Two-dimensional atomic crystals.*, Proceedings of the National Academy of Sciences of the United States of America, **102** (30), 10451–10453 (2005).

[162] C. Cong, T. Yu, K. Sato, J. Shang, R. Saito, G. Dresselhaus and M. Dresselhaus, *Raman Characterization of ABA- and ABC-stacked trilayer graphene*, ACS nano, **5** (11), 8760–8768 (2011).

[163] C. H. Lui, Z. Li, K. F. Mak, E. Cappelluti and T. F. Heinz, *Observation of an electrically tunable band gap in trilayer graphene*, Nature Physics, **7** (12), 944–947 (2011).

[164] E. Delahaye, N. Sandeau, Y. Tao, S. Brasselet and R. Cleément, *Synthesis and second harmonic generation microscopy of nonlinear optical efficient hybrid nanoparticles embedded in polymer films. Evidence for intra- and internanoparticles orientational synergy*, The Journal of Physical Chemistry C, **113** (21), 9092–9100 (2009).

[165] S. Brasselet, V. Le Floc'h, F. Treussart, J.-F. Roch, J. Zyss, E. Botzung-Appert and A. Ibanez, *In Situ diagnostics of the crystalline nature of single organic nanocrystals by nonlinear microscopy*, Physical Review Letters, **92** (20), 207401 (2004).

[166] M. A. van der Veen, B. F. Sels, D. E. De Vos and T. Verbiest, *Localization of p-nitroaniline chains inside zeolite ZSM-5 with second-harmonic generation microscopy*, Journal of the American Chemical Society, **132** (19), 6630–6631 (2010).

[167] M. A. van der Veen, F. Vermoortele, D. E. De Vos and T. Verbiest, *Point group symmetry determination via observables revealed by polarized second-harmonic generation microscopy: (1) theory*, Analytical chemistry, **84** (15), 6378–6385 (2012).

[168] M. A. van der Veen, F. Vermoortele, D. E. De Vos and T. Verbiest, *Point group symmetry determination via observables revealed by polarized second-harmonic generation microscopy: (2) Applications*, Analytical chemistry, **84** (15), 6386–6390 (2012).

[169] A. Gasecka, L.-Q. Dieu, D. Brühwiler and S. Brasselet, *Probing molecular order in zeolite L inclusion compounds using two-photon fluorescence*

polarimetric microscopy, The journal of physical chemistry B, **114** (12), 4192–4198 (2010).

[170] T. Yoon, W. C. Shin, T. Y. Kim, J. H. Mun, T.-S. Kim and B. J. Cho, *Direct measurement of adhesion energy of monolayer graphene as-grown on copper and its application to renewable transfer process.*, Nano letters, **12** (3), 1448–1452 (2012).

[171] A. C. Ferrari, J. C. Meyer, V. Scardaci, C. Casiraghi, M. Lazzeri, F. Mauri, S. Piscanec, D. Jiang, K. S. Novoselov, S. Roth and A. K. Geim, *Raman spectrum of graphene and graphene layers*, Physical Review Letters, **97** (18), 1–4 (2006).

[172] S. Pisana, M. Lazzeri, C. Casiraghi, K. S. Novoselov, A. K. Geim, A. C. Ferrari and F. Mauri, *Breakdown of the adiabatic Born-Oppenheimer approximation in graphene*, Nature materials, **6** (3), 198–201 (2007).

[173] A. Das, S. Pisana, B. Chakraborty, S. Piscanec, S. K. Saha, U. V. Waghmare, K. S. Novoselov, H. R. Krishnamurthy, A. K. Geim, A. C. Ferrari and A. K. Sood, *Monitoring dopants by Raman scattering in an electrochemically top-gated graphene transistor*, Nature nanotechnology, **3** (4), 210–215 (2008).

[174] B. Krauss, T. Lohmann, D.-H. Chae, M. Haluska, K. von Klitzing and J. Smet, *Laser-induced disassembly of a graphene single crystal into a nanocrystalline network*, Physical Review B, **79** (16), 165428 (2009).

[175] M. A. van der Veen, D. E. De Vos and T. Verbiest, *Unraveling molecular architecture inside zeolites with second-harmonic generation microscopy*, *in Proceedings of SPIE* (2010, 77580D.

[176] T. Gokus, R. R. Nair, A. Bonetti, M. Böhmler, A. Lombardo, K. S. Novoselov, A. K. Geim, A. C. Ferrari and A. Hartschuh, *Making graphene luminescent by oxygen plasma treatment*, ACS nano, **3** (12), 3963–3968 (2009).

[177] G. Eda, Y.-Y. Lin, C. Mattevi, H. Yamaguchi, H.-A. Chen, I.-S. Chen, C.-W. Chen and M. Chhowalla, *Blue photoluminescence from chemically derived graphene oxide*, Advanced materials, **22** (4), 505–509 (2010).

[178] Z. Luo, P. M. Vora, E. J. Mele, A. T. C. Johnson and J. M. Kikkawa, *Photoluminescence and band gap modulation in graphene oxide*, Applied Physics Letters, **94** (11), 111909 (2009).

[179] Y. Zhang, T.-T. Tang, C. Girit, Z. Hao, M. C. Martin, A. Zettl, M. F. Crommie, Y. R. Shen and F. Wang, *Direct observation of a widely tunable bandgap in bilayer graphene*, Nature, **459** (7248), 820–823 (2009).

[180] H. Zhang, D. Tang, R. J. Knize, L. Zhao, Q. Bao and K. P. Loh, *Graphene mode locked, wavelength-tunable, dissipative soliton fiber laser*, Applied Physics Letters, **96** (11), 111112 (2010).

[181] V. K. Valev, B. De Clercq, C. G. Biris, X. Zheng, S. Vandendriessche, M. Hojeij, D. Denkova, Y. Jeyaram, N. C. Panoiu, Y. Ekinci, A. Silhanek, V. Volskiy, G. A. E. Vandenbosch, M. Ameloot, V. V. Moshchalkov and T. Verbiest, *Distributing the optical near-field for efficient field-enhancements in nanostructures*, Advanced materials, **24** (35), OP208–OP215 (2012).

[182] M. L. Foo, S. Horike, Y. Inubushi and S. Kitagawa, *An alkaline earth I3O0 porous coordination polymer: [Ba2TMA(NO3)(DMF)]*, Angewandte Chemie, **51** (25), 6107–6111 (2012).

[183] F. G. Fumi, *Physical properties of crystals: the direct-inspection method*, Acta Crystallographica, **5** (1), 44–48 (1952).

List of publications

Peer reviewed publications

1. V. K. Valev, **M. K. Vanbel**, B. Vincent, V. V. Moshchalkov, M. Caymax and T. Verbiest,
Second harmonic generation indicates a better Si/Ge interface quality for higher temperature and with N_2 rather than with H_2 as the carrier gas
IEEE Electron Device Letters, **32** (1), 12-14 (2011).

2. B. Vincent, R. Loo, W. Vandervorst, J. Delmotte, B. Douhard, V. K. Valev, **M. Vanbel**, T. Verbiest, J. Rip, B. Brijs, T. Conard, C. Claypool, S. Takeuchi, S. Zaima, J. Mitard, B. De Jaeger, J. Dekoster and M. Caymax,
Si passivation for Ge pMOSFETs: Impact of Si cap growth conditions
Solid State Electronics, **60** (1), 116-121 (2011).

3. **M. K. Vanbel**, V. K. Valev, B. Vincent, V. V. Afanas'ev, J.-P. Locquet, S. Van Elshocht, M. Caymax and T. Verbiest,
Second-harmonic generation reveals the oxidation steps in semiconductor processing
Journal of Applied Physics, **111** (6), 064504 (2012).

4. **M. K. Vanbel**, V. V. Afanas'ev, C. Adelmann, M. Caymax, V. K. Valev and T. Verbiest,
Tunneling of holes is observed by second-harmonic generation
Applied Physics Letters, **102** (8), 082104 (2013).

5. H. Moshe, **M. Vanbel**, V. K. Valev, T. Verbiest, D. Dressler and Y. Mastai,
Chiral thin films of metal oxide
Chemistry - A European Journal, **19** (31), 10295-10301 (2013).

6. **M. K. Vanbel**, C.-Y. Su, J.-P. Locquet and T. Verbiest,
Electric field-induced second-Harmonic generation demonstrates different interface properties of molecular beam epitaxy grown MgO on Si
Journal of Physical Chemistry C, **118** (4), 1919-1924 (2014).

7. M. Bloemen, S. Vandendriessche, V. Goovaerts, W. Brullot, **M. Vanbel**, S. Carron, N. Geukens, T. Parac-Vogt and T. Verbiest,
Synthesis and characterization of holmium doped iron oxide nanoparticles
Materials, **7** (2), 1155-1164 (2014).

Conference proceeding publications

1. **M. K. Vanbel**, A. Delabie, S. Sioncke, C. Adelmann, V. V. Afanas'ev, J.-P. Locquet, S. Van Elshocht, M. Caymax and T. Verbiest,
Second-harmonic generation as characterization tool for Ge/high-k dielectric interfaces
Proceedings to SPIE, **8434**, 2012, 84341F.

2. A. V. Klekachev, I. Asselberghs, C. Huyghebaert, **M. Vanbel**, M. A. van der Veen, A. L. Stesmans, M. M. Heyns, S. De Gendt and T. Verbiest,
SHG/2PF microscopy of single and multi-layer graphene
Proceedings to SPIE, **8474**, 2012, 847405.

3. J. Perez-Moreno, S. Van Cleuvenbergen, **M. Vanbel**, K. Clays and E. W. Taylor,
An all-optical protocol to determine the molecular origin of radiation damage/enhancement in electro-optic polymeric materials
Proceedings to SPIE, **8519**, 2012, 85190C.

4. **M. Vanbel**, S. Vandendriessche, M. A. van der Veen, D. Slavov, P. Heister, R. Paesen, V. K. Valev, M. Ameloot and T. Verbiest,
"*Second-harmonic generation from complex chiral samples*
Proceedings to SPIE, volume 8770, 2013, 87701F.

5. **M. K. Vanbel**, R. Paesen, W. Brullot, S. Vandendriessche, I. Asselberghs, K. Markey, P. Valvekens, M. A. van der Veen, D. De Vos, M. Ameloot, V. K. Valev, J.-P. Locquet and T. Verbiest,
Fast Fourier-transform second-harmonic generation (FFT-SHG) provides a solution for measuring nonlinear effects on fragile structures,
Frontiers in Optics, **3**, 2013, FTu2F.5.

FACULTY OF SCIENCE
DEPARTMENT OF CHEMISTRY
MOLECULAR IMAGING AND PHOTONICS
Celestijnenlaan 200D box 2425
B-3001 Heverlee